NASA Contractor Report 198374

NASA-CR-198374
19960001942

Real Time Acousto-Ultrasonic NDE Technique for Monitoring Damage in Ceramic Composites Under Dynamic Loads

Anil Tiwari
Virginia Polytechnic Institute and State University
Blacksburg, Virginia

FOR REFERENCE
NOT TO BE TAKEN FROM THIS ROOM

August 1995

COPY
NOV 1995
CENTER

Prepared for
Lewis Research Center
Under Contract NAS3–26827

National Aeronautics and
Space Administration

NF01389

NASA Technical Library
3 1176 01423 1766

REAL TIME ACOUSTO-ULTRASONIC NDE TECHNIQUE FOR MONITORING DAMAGE IN CERAMIC COMPOSITES UNDER DYNAMIC LOADS

NASA Contractor Report

Sponsored by HITEMP Project Office
NASA LeRC, Cleveland, OH.

Anil Tiwari

Engineering Science and Mechanics Department,
Virginia Polytechnic Inst. & State University, Blacksburg, VA.

ABSTRACT

Research effort was directed towards developing a near real-time, acousto-ultrasonic (AU), nondestructive evaluation (NDE) tool to study the failure mechanisms of ceramic composites. Progression of damage is monitored in real-time by observing the changes in the received AU signal during the actual test. During the real-time AU test, the AU signals are generated and received by the AU transducers attached to the specimen while it is being subjected to increasing quasi-static loads or cyclic loads (10 Hz, R = 0.1). The received AU signals for 64 successive pulses were gated in the time domain (T = 40.96 μ sec) and then averaged every second over ten load cycles and stored in a computer file during fatigue tests. These averaged gated signals are representative of the damage state of the specimen at that point of its fatigue life. This is also the first major attempt in the development and application of real-time AU for continuously monitoring damage accumulation during fatigue without interrupting the test.

The present work has verified the capability of the AU technique to assess the damage state in silicon carbide/calcium aluminosilicate (SiC/CAS) and silicon carbide/magnesium aluminosilicate (SiC/MAS) ceramic composites Continuous monitoring of damage initiation and progression under quasi-static ramp loading in tension to failure of unidirectional and cross-ply SiC/CAS and quasi-isotropic SiC/MAS ceramic composite specimens at room temperature was accomplished using near real-time AU parameters.

The AU technique was shown to be able to detect the stress levels for the onset and saturation of matrix cracks, respectively The critical cracking stress

level is used as a design stress for brittle matrix composites operating at elevated temperatures. The AU technique has found that the critical cracking stress level is 10-15 % below the level presently obtained for design purposes from analytical models.

An acousto-ultrasonic stress-strain response (AUSSR) model for unidirectional and cross-ply ceramic composites was formulated. The AUSSR model predicts the strain response to increasing stress levels using real-time AU data and classical laminated plate theory. The Weibull parameters of the AUSSR model are used to calculate the design stress for thermo-structural applications. Real-time AU together with the AUSSR model was used to study the failure mechanisms of SiC/CAS ceramic composites under static and fatigue loading An S-N curve was generated for a cross-ply SiC/CAS ceramic composite material The AU results are corroborated and complemented by other NDE techniques, namely, in-situ optical microscope video recordings and edge replication

TABLE OF CONTENTS

1. INTRODUCTION 1

1.1 Introduction 1

1.2 Problem Statement 5

2. ACOUSTO-ULTRASONIC TECHNIQUE 7

2.1 Introduction 7

2.2 Ring down SWF method 8

2.3 Weighted ring down SWF method 9

2.4 Modified Acousto-ultrasonic technique 10

2.4.1 Frequency-spectrum analysis 10

2.5 Real time AU 15

3. EXPERIMENTAL PROCEDURES 17

3 1 Material Systems 17

3.2 Sample Preparation 20

3.3 Mechanical Testing 23

3.3.1 Quasi-static strength testing 23

3.3.2 Fatigue testing 23

3.4 Nondestructive Testing 24

3.4.1 Acousto-ultrasonic Technique 24

3.4.2 X-Ray Radiography 28

3.4.3 Ultrasonic C-scan 29

3.4.4 Scanning electron microscope (SEM) 29

3.4.5 Long distance optical video microscope 29

3.4.6 Edge replication 30

3.4.7 Stiffness reduction 31

4. QUASI-STATIC TESTING 32
4.1 Introduction 32
4.2 Unidirectional SiC/CAS static tests 34
4.2.1 Heat treated unidirectional $[0_8]_s$ SiC/CAS static tests 49
4.3 Failure process of Unidirectional $[0_8]_s$ SiC/CAS under static loads . 52
4.4 Cross-ply $[0/90]_{4s}$ SiC/CAS static tests 62
4 4.1 Heat treated cross-ply $[0/90]_{4s}$ SiC/CAS static tests . . 72
4.5 Failure Process of cross-ply $[0/90]_{4s}$ SiC/CAS under static loads 78
4.6 Quasi-isotropic $[0/+-45/90]_{2s}$ SiC/MAS static tests 79
4.6.1 Heat treated Quasi-isotropic $[0/+-45/90]_{2s}$ SiC/MAS static tests 82

5. AUSSR MODEL 89
5.1 Introduction 89
5.2 Ply-discount Scheme 95
5.3 AUSSR model for unidirectional ceramic composites . . 96
5.3.1 Introduction 96
5.3.2 AUSSR model 97
5 3.3 AUSSR-WZ model 102
5.3.4 AUSSR-WZ-WB model 104
5.3.5 Modified AUSSR model 107
5.4 AUSSR model for cross-ply ceramic composites . . 111
5.5 Summary 113

6. FATIGUE TESTING 116
6.1 Introduction 116
6.2 Validation of real time AU technique during fatigue tests . . 117
6.3 Fatigue testing 120
6.3.1 Introduction 120
6.3.2 High load amplitude fatigue 124

6.3.3 Medium load amplitude fatigue 128
6.3.4 Low load amplitude fatigue 137
6.4 S-N Curve 154
6.5 Failure process during Fatigue 156
6.6 Summary 160

7. CONCLUSIONS AND FUTURE RECOMMENDATIONS 162
7.1 Development of real-time AU technique 162
7.2 Quasi-static tests 163
7.2.1 Failure process in $[0_8]_s$ SiC/CAS ceramic composite under quasi-static loads 163
7.2.2 Failure process in $[0/90]_{4s}$ SiC/CAS ceramic composite under quasi-static loads 165
7.3 AUSSR model 166
7.4 Fatigue tests 167
7.5 Recommendations for future work 169

REFERENCES 171

List of Tables

Table 1. Properties of SiC/CAS ceramic composite 19

Table 2. Experimental program. 22

Table 3. Quasi-static test results. 50

List of illustrations

Figure 1. Conceptual configuration of acousto-ultrasonic (AU) set-up . . 11

Figure 2. Detailed view of specimen dimensions. 21

Figure 3. (a) Photographic view of real time AU set-up (b) Enlarged view of the transducer holder device attached to the specimen. . . 26

Figure 4. Stress vs strain for sample G14 (SiC/CAS, $[0_9]_s$) 35

Figure 5. Normalized SWF (M0) vs stress for sample G14 (SiC/CAS, $[0_9]_s$) 37

Figure 6. Photo-micrograph of the damaged surface after matrix saturation of cracks for sample G14 (SiC/CAS, $[0_9]_s$) 38

Figure 7. Normalized SWF (M0) vs stress for sample U2 (SiC/CAS, $[0_8]_s$) 39

Figure 8. (a) SEM photo-micrograph of the failure surface of sample U2 (SiC/CAS, $[0_8]_s$), (b) Enlarged view of the failure surface. 41

Figure 9. Normalized SWF (M0) vs stress for sample U5 (SiC/CAS, $[0_8]_s$), (loaded in load control mode till saturation of matrix cracks) . . 43

Figure 10. Normalized SWF (M0) vs displacement for sample U5 (SiC/CAS, $[0_8]_s$), (loaded in constant displacement control mode till failure) . . . 44

Figure 11. Normalized SWF (M0) vs stress for sample U4 (SiC/CAS, $[0_8]_s$) 46

Figure 12. Stress vs strain for sample U4 (SiC/CAS, $[0_8]_s$) 47

Figure 13. Normalized SWF (M0) vs stress for sample U10 (SiC/CAS, $[0_8]_s$) 48

Figure 14. Initial SWF (M0) vs ultimate tensile strength of unidirectional samples (SiC/CAS, $[0_8]_s$) 51

Figure 15. Normalized SWF (M0) vs stress for sample U8 (SiC/CAS, $[0_8]_s$) (Heat treated at 1200°C for 48 hrs.) 53

Figure 16. Normalized SWF (M0) vs stress for sample U9 (SiC/CAS, $[0_8]_s$) (Heat treated at 1200°C for 48 hrs.) 54

Figure 17. Stress vs strain for sample U9 (SiC/CAS, $[0_8]_s$) (Heat treated at 1200°C for 48 hrs.) 55

Figure 18. Photograph of the failed heat treated specimens U8 and U9, (SiC/CAS, $[0_8]_s$) 56

Figure 19. Normalized SWF (M0) vs stress for sample C5 (SiC/CAS,$[0/90]_{4s}$) 63

Figure 20. Stress vs strain for sample C5 (SiC/CAS, $[0/90]_{4s}$) 64

Figure 21. Normalized SWF (M0) vs stress for sample C2(SiC/CAS, $[0/90]_{4s}$) 65

Figure 22. Normalized SWF (M0) vs stress for sample C6 (SiC/CAS, $[0/90]_{4s}$) 67

Figure 23. Stress vs strain for sample C6 (SiC/CAS, $[0/90]_{4s}$) . . . 68

Figure 24. Normalized SWF (M0) vs stress for sample C7 (SiC/CAS, $[0/90]_{4s}$) 69

Figure 25. (a) Photo-micrograph of the failure surface of sample C6 (SiC/CAS, $[0/90]_{4s}$), (b) Enlarged view 70

Figure 26. Photo-micrograph showing interfacial debond at failure for sample C6 (SiC/CAS, $[0/90]_{4s}$) 71

Figure 27. Normalized SWF (M0) vs stress for sample C8 (SiC/CAS, $[0/90]_{4s}$), (Heat treated at 1200°C for 48 hrs.) . 73

Figure 28. Stress vs strain for sample C8 (SiC/CAS, $[0/90]_{4s}$) (Heat treated at 1200°C for 48 hrs.) 74

Figure 29. Normalized SWF (M0) vs stress for sample C9 (SiC/CAS, $[0/90]_{4s}$), (Heat treated at 1200°C for 48 hrs.) 75

Figure 30. (a) Polished surface of heat treated sample C9 (SiC/CAS, $[0/90]_{4s}$) (b) SEM photo-micrograph of a fiber located at the mid-region of the laminate at failure (sample C9). 76

Figure 31. (a) SEM photo-micrograph of the failure surface of heat treated sample C9 (SiC/CAS, $[0/90]_{4s}$) (b) Enlarged view showing non-uniform heat treatment 77

Figure 32. Normalized SWF (M0) vs stress for sample MAS-8 (SiC/MAS, $[0/\pm45/90]_{2s}$) 80

Figure 33. Stress vs strain for sample MAS-8 (SiC/MAS, $[0/\pm45/90]_{2s}$) . . 81

Figure 34. Normalized SWF (M0) vs stress for sample MAS-11 (SiC/MAS, $[0/\pm45/90]_{2s}$) 83

Figure 35. Normalized SWF (M0) vs stress for sample MAS-1 (SiC/MAS, $[0/\pm45/90]_{2s}$) 84

Figure 36. Stress vs strain for sample MAS-1 (SiC/MAS, $[0/\pm45/90]_{2s}$) . . . 85

Figure 37. Normalized SWF (M0) vs stress for sample MAS-3 (SiC/MAS, $[0/\pm45/90]_{2s}$) 86

Figure 38. Normalized SWF (M0) vs stress for sample MAS-10 (SiC/MAS, $[0/\pm45/90]_{2s}$) 87

Figure 39. Strain response to increasing stress - ply discount scheme and linear variation of E_m and G_m over matrix cracking stress range. 98

Figure 40. Weibull distribution fit to a typical AU (SWF(M0) data for SiC/CAS $[0_8]_s$ ceramic composite (α = 15 and β = 235 MPa) . 100

Figure 41. AUSSR model predictions and experimental stress-strain curve for unidirectional SiC/CAS $[0_8]_s$ ceramic composite. 101

Figure 42. Weitsman's (WZ) model predictions of additional strains due to fiber breaks and Weibull distribution curve fit to the model. (α = 50 and β = 290 MPa) 103

Figure 43. AUSSR - WZ model predictions and experimental stress-strain curve for unidirectional SiC/CAS $[0_8]_s$ ceramic composite. 105

Figure 44. AUSSR - WZ - WB model predictions and experimental stress-strain curve for unidirectional SiC/CAS $[0_8]_s$ ceramic composite. . . . 106

Figure 45. Modified AUSSR-WZ-WB model predictions and experimental stress-strain curve for unidirectional SiC/CAS $[0_8]_s$ ceramic composite. 108

Figure 46. Modified AUSSR model predictions and experimental stress-strain curve for unidirectional SiC/CAS $[0_8]_s$ ceramic composite 110

Figure 47. AUSSR model predictions and experimental stress-strain curve for cross-ply SiC/CAS $[0/90]_{4s}$ ceramic composite 112

Figure 48. Validation of AU set-up for fatigue testing. 119

Figure 49. Ultrasonic C-scan of cross-ply SiC/CAS $[0/90]_{4s}$ ceramic composite 121

Figure 50. X-ray radiograph of cross-ply SiC/CAS $[0/90]_{4s}$ ceramic composite . 122

Figure 51. Normalized SWF (M0) vs % life for sample C18, SiC/CAS $[0/90]_{4s}$ (σ_{max} = 90% UTS) 125

Figure 52. Photo-micrograph of transverse matrix cracks at failure sample C18 126

Figure 53. Normalized SWF (M0) and normalized static stiffness vs % life for sample C12, SiC/CAS $[0/90]_{4s}$ (σ_{max} = 90% UTS) . 127

Figure 54. Normalized SWF (M0) and normalized static stiffness vs % life for sample C12, SiC/CAS $[0/90]_{4s}$ at early life (σ_{max} = 90% UTS) . 129

Figure 55. (a) SEM photo-micrograph of the failure surface of sample C12, SiC/CAS $[0/90]_{4s}$, (b) Enlarged view of the failure surface 130

Figure 56. Photo-micrograph showing debonding at the fiber/matrix interface of sample C12, SiC/CAS $[0/90]_{4s}$ 131

Figure 57. Normalized SWF (M0) and normalized static stiffness vs % life for sample C13, SiC/CAS $[0/90]_{4s}$ (σ_{max} = 90% UTS) 132

Figure 58. Edge replicas of the damaged surface of sample C13, SiC/CAS $[0/90]_{4s}$ (σ_{max} = 90% UTS) 133

Figure 59. Normalized SWF (M0) vs % life for sample C19, SiC/CAS $[0/90]_{4s}$ (σ_{max} = 85% UTS) 134

Figure 60. Normalized SWF (M0) vs % life for sample C17, SiC/CAS $[0/90]_{4s}$ (σ_{max} = 75% UTS) 135

Figure 61. Local delaminations in the 90° plies of sample C17, SiC/CAS $[0/90]_{4s}$ (σ_{max} = 75% UTS) 136

Figure 62. Normalized SWF (M0) and normalized static stiffness vs cycles for sample C4, SiC/CAS $[0/90]_{4s}$ (σ_{max} = 75% UTS) 138

Figure 63. Normalized SWF (M0) and normalized static stiffness vs % life for sample C11, SiC/CAS $[0/90]_{4s}$ (σ_{max} = 60% UTS) 139

Figure 64. Normalized SWF (M0) and normalized static stiffness vs cycles for sample C11, SiC/CAS $[0/90]_{4s}$ at early life (σ_{max} = 60% UTS) . . 140

Figure 65. Edge replicas of the damaged surface of sample C11, SiC/CAS $[0/90]_{4s}$ (σ_{max} = 60% UTS) 141

Figure 66. SEM photo-micrograph of the failure surface of sample C11, SiC/CAS $[0/90]_{4s}$ 142

Figure 67. (a) SEM photo-micrograph of the failure surface of sample C11, SiC/CAS $[0/90]_{4s}$, (b) Enlarged view 143

Figure 68. Normalized SWF (M0) and normalized static stiffness vs % life for sample C16, SiC/CAS $[0/90]_{4s}$ (σ_{max} = 60% UTS) 145

Figure 69. Normalized SWF (M0) vs % life for sample C20, SiC/CAS $[0/90]_{4s}$ (σ_{max} = 60% UTS) 146

Figure 70. Photograph showing failure locations of samples C11, C16 and C20 SiC/CAS $[0/90]_{4s}$ (σ_{max} = 60% UTS) 147

Figure 71. Normalized SWF (M0) and normalized static stiffness vs cycles for sample C3, SiC/CAS $[0/90]_{4s}$ (σ_{max} = 66% UTS) 148

Figure 72. Edge replicas of the damaged surface of sample C3, SiC/CAS $[0/90]_{4s}$ (σ_{max} = 66% UTS) 149

Figure 73. Local delaminations in the 90° plies of sample C3, SiC/CAS $[0/90]_{4s}$ (σ_{max} = 66% UTS) 151

Figure 74. Normalized SWF (M0) and normalized static stiffness vs % life for sample C14, SiC/CAS $[0/90]_{4s}$ (σ_{max} = 65% UTS) 152

Figure 75. Normalized SWF (M0) vs % life for sample C15, SiC/CAS $[0/90]_{4s}$ (σ_{max} = 65% UTS) 153

Figure 76. S-N curve for cross-ply SiC/CAS $[0/90]_{4s}$ ceramic composite. . . . 155

1. INTRODUCTION

1.1 Introduction

Monolithic ceramic materials have been used for centuries to manufacture components exposed to very high temperatures. These materials can withstand harsh chemical environments besides offering higher oxidation resistance than most metals. Monolithic ceramic materials also have a higher strength to weight ratio and a higher stiffness to weight ratio than most metals. These attractive features make ceramic materials a preferred choice over most metals or alloys for high temperature applications.

Although ceramic materials possess attractive features, they have inherent shortcomings limiting their usefulness in many applications. Poor material reliability make these materials unacceptable in many instances, although these materials can have excellent mechanical integrity and chemical stability at high temperatures. These materials are extremely sensitive to micro-cracks and other flaws. Mechanical behavior is degraded by the presence of flaws such as pores, large grains and micro-structural irregularities. Ceramic materials show little damage tolerance and failure is catastrophic, thereby limiting their use in structural applications.

The quantitative prediction of the degradation of mechanical properties as a result of flaws and their distribution is a complex problem yet to be tackled successfully. The reliability of such materials could be improved by development of nondestructive evaluation (NDE) techniques to detect and characterize the

shape, size and location of flaws and thereby assess the degradation of structural ceramics. Reliability after processing these materials is also a major concern. Proof testing can eliminate defective parts and can be used as a quality control in the manufacturing stage. However, proof testing of ceramic components is time consuming and expensive. Also, proof testing being destructive can itself damage the components that pass the testing.

A significant amount of research [1-28] has been done to develop and refine NDE techniques to detect critical flaws in structural monolithic ceramic composites. The application of different NDE techniques to each ceramic material depends on its ability to detect not only the critical flaws but also to monitor the growth of the sub-critical flaws in the material. The location, shape and size of these flaws are used in fracture mechanics models to predict the life of structures under operating loads.

Munz, et. al., [1] introduced artificial flaws such as pores and Fe- inclusions in reaction bonded silicon nitride and sintered silicon nitride bend specimens. Fracture mechanics models to predict bending strength were applied based on the flaw data from NDE, fracture surface analysis and fracture toughness of the material.

Klima, et. al., [2] used radiographics, ultrasonics, scanning laser acoustic microscopy and thermo-acoustic microscopy to characterize silicon carbide and silicon nitride modulus of rupture specimens. Ultrasonics was found to be sensitive to micro-structural variations in grain and void morphology and their distributions. Scanning laser acoustic microscope was capable of detecting voids, inclusions and cracks in these specimens.

Nongaillard, et. al., [3] have shown that scanning acoustic microscope operating at 100 MHz range is an effective tool for nondestructive evaluation of ceramic materials. Scanning acoustic microscope detected flaws and inclusions smaller than 50μm.

Fahr, et. al., [4] have used a 10-100 MHz surface acoustic wave system with a computer controlled data acquisition and analysis system to characterize surface cracks in ceramics. At 100 MHz, surface acoustic wave system could detect a 25 μm deep crack on a polished ceramic specimen.

Cielo, et. al., [5] have used three laser based techniques for characterization of sintered materials. A good correlation was obtained with the independently measured density of the zirconia samples. Vary, et. al., [6] compared scanning laser acoustic microscopy, scanning acoustic microscopy, photo-acoustic microscopy and electron acoustic microscopy to detect flaws in structural ceramics.

Presently, ongoing research in the NDE of ceramics [7-28] is primarily focussed on developing and refining NDE techniques such as computed tomography, scanning laser acoustic microscopy, scanning acoustic microscopy, microradiography, ultrasonics and radiography to detect critical flaws with reliability and to locate and size them.

There is a need to develop new material systems which have all the inherent advantages of monolithic ceramics but are more tough and damage tolerant. The toughening of ceramics can be achieved by adding a second phase material system in the form of particles, whiskers or continuous fibers to create ceramic composites. The second phase materials toughen the material system by deflecting and branching approaching cracks, and by increasing resistance to

fracture and work of fracture by introduction of fiber debond, crack bridging, fiber breakage and fiber pullout mechanisms. Residual stresses due to thermal coefficient mismatch can also be a contributing factor to the toughening mechanism. Optimization of the interphase can also increase fracture resistance and thereby allow for smooth graceful failure. Research and development in the ceramic composites field have yielded new material systems with increased fracture resistance, higher strength and higher strain to failure.

Presently, the processing of reliable ceramic composites is a cause for major concern in composite manufacturing industries. Processing and manufacturing of ceramic composite components can introduce defects which will affect the overall integrity of the resultant composite structure. Interest in NDE as a tool or means to weed out defective components during the processing stage and for in-service quality monitoring has grown.

There is a need to develop NDE techniques that can assess and quantify the damage present in ceramic composites and relate a quantifiable parameter directly to strength or long time serviceability of the component. The present challenge in the field of NDE is to assess initial integrity and also damage accumulation and residual strength during service. Real-time NDE monitoring of damage under dynamic loads could also be used as a tool to study the failure mechanisms of composite material systems in the laboratory.

1.2 Problem Statement

Acoustic emission and ultrasonics are widely used to evaluate material performance. Alex Vary and co-workers [29-31] developed a technique, viz., the acousto-ultrasonic (AU) method, which is a hybrid of acoustic emission and ultrasonics. AU studies [29-75] show a correlation between stress wave propagation characteristics determined by AU and the mechanical properties of the material. The AU method measures an integrated effect of damage/flaws present in the material between two transducers.

The primary objective of the present research is to determine the feasibility of the real-time AU technique to assess the damage state and to monitor damage development in ceramic composites under dynamic loads. A real-time AU technique is developed to take AU data for quasi-static ramp loading in tension to failure and also for fatigue loading. The feasibility of the real-time AU for this purpose is shown. Next, it is shown that AU can identify different damage modes and is able to monitor the progress of these damage modes.

Unidirectional and cross-ply tensile specimens of SiC/CAS and quasi-isotropic tensile specimens of SiC/MAS are loaded in tension to failure and the damage growth is continuously monitored in near real-time by AU parameters. Several specimens are heat treated before loading. The changes in the damage characteristics are evaluated by real- time AU monitoring. Damage initiation and growth under cyclic loading in cross-ply SiC/CAS specimens are continuously monitored by the AU technique specially developed for fatigue loading. Various other NDE techniques are utilized to complement the AU results. Based on the present results by the author, it is believed that real-time AU can decipher the true nature of damage mechanisms taking place in a brittle matrix composite.

The present research work is presented as follows: Chapter 2 describes the AU technique with its basic theory and underlying principles. Chapter 3 explains the experimental setup of the various NDT experiments and the mechanical tests performed. Results for quasi-static tests are discussed in chapter 4 with the acousto-ultrasonic stress-strain response (AUSSR) model described in chapter 5. The AUSSR model uses real-time AU data and classical laminated plate theory (CLPT) to predict the strain response at increasing stress levels of a laminate. Fatigue test results are presented in chapter 6 along with the S-N data curve generated for cross-ply SiC/CAS ceramic composite. Concluding remarks are presented in chapter 7 along with proposed future work.

2. ACOUSTO-ULTRASONIC TECHNIQUE

2.1 Introduction

Two basic NDT techniques that have been extensively used to evaluate the mechanical integrity of structures are acoustic emission (AE) and ultrasonics. To perform AE, it is necessary to load the structure being monitored. The AE results from discontinuous, sudden permanent changes (damage) in the micro-structure. Whether or not the damage resulting from an AE test affects the overall performance of the structure depends upon the level to which the material has been loaded. Ultrasonics can detect flaws, such as voids, foreign inclusions or fatigue damage, present in the specimen. For the study of advanced materials, a new Acousto-Ultrasonic (AU) technique, a hybrid of the ultrasonics and AE techniques was suggested by Vary and co-workers [29-31]. The AU technique induces an ultrasonic signal into a specimen and subsequently detects and analyzes it using AE methods. One of the major advantages of the AU technique is that it gives an integrated effect of overall flaw/damage present in the structure between the transmitting and receiving transducers. The stress wave propagation parameters are measured in the principal load directions, which means the stress waves must take the same path that the loading would take in the structure. This is the key to the measurement.

The AU technique excites a repeated series of ultrasonic pulses in the specimen by a broad band transmitting transducer through a couplant medium. The receiver and the sender transducers are placed normally on the same side of the specimen. The propagating stress wave interacts with the microstructure and

flaws present between the two transducers. The received signal can be analyzed to evaluate the changing state of damage. The analysis of the received signal produces a parameter referred to as stress wave factor (SWF) which can be related quantitatively to the mechanical performance of the material. The SWF value is a measure of stress wave energy transmission and provides a rating of the efficiency with which dynamic strain energy transfer takes place in the material. If the material exhibits high SWF values, the material has better transmission of dynamic stress or a better load re-distribution capability and hence will have higher strength. Conversely, low SWF values indicate regions where dynamic strain energy is likely to concentrate and promote fracture.

2.2 Ring down SWF method

Vary [29] defined the SWF as a product of three quantities, namely N,T and (p.p.s.)

$$SWF = N \times T \times (p.p.s.) \tag{2.1}$$

where,

N	=	number of times the received signal crosses a certain fixed threshold level.
T	=	time gate interval
p.p.s.	=	pulse repetition rate or pulses per second

This method of quantifying the detected stress wave has limitations. The threshold level has to be set so as not to incorporate signals in the noise level. It

cannot be set too high, since then it may not be sensitive to the changing damage/flaws present in the structure. It has been shown that the ring down SWF decreases in proportion to a fractional power of the ultimate tensile strength of graphite/epoxy [31].

2.3 Weighted ring down SWF method

A different approach to account for the amplitude of the signal was developed by Williams and Lampert [73]. A modified approach was adopted by Fahr [62], in which the noise level, V_0, is first determined, and then the threshold level is set above it. The total number of counts above V_0 is determined. The threshold level is increased by a small amount, δV and again the number of counts is determined. The difference between these two readings is multiplied by the amplitude at that threshold level. This value is summed by successive increases in threshold level until the peak amplitude of the waveform is reached.

$$SWF = \sum_{i=0}^{n} V_i \, (C_i - C_{i+1}) \tag{2.2}$$

where,

V_i	=	Threshold level at the i-th count
C_i	=	Number of counts at the i-th level.
V_n	=	Peak amplitude of the waveform.

This weighted ring down SWF method for determining the SWF is more

sensitive to damage than the original; the smaller the increments between threshold levels, the greater this sensitivity.

2.4 Modified Acousto-ultrasonic technique

An alternative approach for analyzing the received AU signal has been developed in our laboratory [32-49]. A conceptual configuration of an AU set-up is shown in Fig. 1. This approach converts the digitized time-voltage signal received at the receiving transducer into an amplitude-frequency spectrum by means of a Hartley's transform algorithm [76-77] defined by the equation given below.

$$F(\nu) = \frac{1}{N} \sum_{n=0}^{N-1} f(\tau)\, e^{\frac{-i2\pi n\nu}{N}} \tag{2.3}$$

Various statistical moments of the frequency spectrum are then calculated and defined as various SWF values as explained below.

2.4.1 Frequency-spectrum analysis

Talreja [78] suggested that three classes of parameters can be used to describe any distribution function, viz., scale, location, and shape parameters. One can consider the frequency spectrum to be a plane figure, closed on the frequency axis. Then, various moments of the frequency spectrum plane figure can be calculated using equation (2.4).

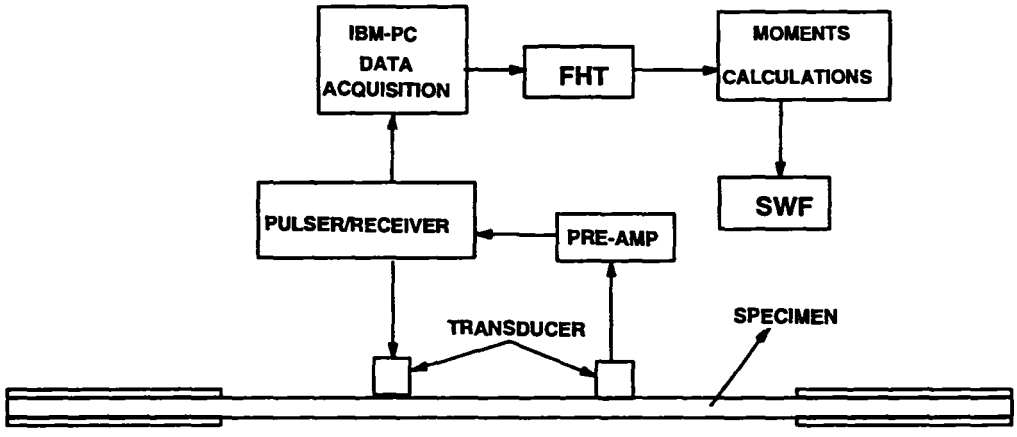

Figure 1 Conceptual configuration of acousto-ultrasonic (AU) set-up.

Moments

$$M_r = \int_{-\infty}^{\infty} S(f)\, f^r\, df \qquad (2.4)$$

where,

r	=	0,1,2,3,....
f	=	Frequency
S(f)	=	Power spectral density
M_r	=	r^{th} moment

The zeroth moment is then simply the area under the spectral density distribution and is indicative of the total energy content of the received signal. The location parameter is given by the centroid of the frequency distribution curve, equation (2.5).

Location parameter

$$f_c = \frac{M_1}{M_0} \qquad (2.5)$$

where,

f_c	=	Centroid of the frequency distribution
M_1	=	First moment of the frequency distribution
M_0	=	Zeroth moment of the frequency distribution

Shape parameters

Different shape parameters can then be defined by the following:

$$S_{r,k} = \frac{M_r}{M_{r-k}\, f_c^k} \tag{2.6}$$

where,

k = 1,2,3,....

r = 2,3,4,....

r > k

Studies have shown that the moments defined above are affected by damage/flaws present in the structure in a particular manner, such that the latter can be located and characterized. Stiffler, et al., [42] have shown that a decrease in SWF values calculated by the moments method correlates well with the reduction of stiffness of graphite-epoxy composite specimens subjected to fatigue tests. Tiwari, et al. [43-45] have used the moments method for assuring adhesive bond quality.

Researchers [29-49] have shown acousto-ultrasonic (AU) parameters to be more sensitive than stiffness measurements as a means of monitoring damage development. Although physical understanding of the effect of damage on wave propagation and on the AU signal is not yet completely understood, researchers have suggested that the local stress state or displacement field is modified by the damage present. By recording information on stress wave propagation characteristics one can hope to obtain information about the value of stress

concentration or impending failure modes. The moments analysis of the received signal in the frequency domain produces a stress wave factor (SWF) which can be correlated to residual strength/stiffness of the specimen through additional experimental measurements [46-49].

Kautz [54] compared AU signals from a neat resin and a composite of the resin matrix having the same geometry. Results indicated that AU energy introduced into a laminated Gr/resin propagates by two modes through the structure. The first mode propagating along the Gr fibers is faster than the second mode in the resin. The second mode was attenuated at higher frequencies. Kautz et. al. [53] have shown a correlation between ultrasonic velocity data and interfacial shear strength data determined from mechanical tests on SiC/RBSN. Kautz [55] and Sundaresan [41] applied AU to filament wound composite structures. AU could detect delaminations and defects due to dry windings and winding tension variations. Kautz et. al. applied AU to SiC/Ti-15-3 metal matrix composite with different lay-ups. SWF was found to be sensitive to fiber/matrix debonding due to mechanical strain and also due to thermal cycling.

Additional research [36, 39, 65-69] at Virginia Tech has studied the characteristics of AU signals. Tang et. al. [66] used dispersion curves (fh vs kh; h is the thickness of the plate and k is the wave number) to characterize composite plates since each material and stacking sequence gives distinct dispersion curves. A modified AU method was used to measure the low frequency, long wavelength flexural wave phase velocity V_p.

Kiernan et. al. [36,39] made the first attempt to provide a general physical explanation for AU results in composite plates based on elasticity solutions, Lamb wave theory and through-the-thickness transverse resonance (TTR). Velocity

measurements and the frequency content of AU signals were compared to Lamb wave theory predictions. Higher order lamb waves were identified as a dominant mode of propagation. Kiernan [39] has shown the effect of the variation of the input disturbance in terms of the frequency content of AU signals. The AU signal output needs to be modified by a frequency dependent weighting function to account for the frequency variation of the input signal. Also, a slight-off normal repositioning of transducers could change the AU energy sent in a given direction.

Kiernan and Duke [37] utilized the variation of AU signals with respect to azimuthal angles to predict the growth of impact damage. Damage was shown to increase in the direction of higher AU values caused by the redirection of reflected energy in that direction.

2.5 Real-time AU

Real-time monitoring of damage progression in ceramic composites by a NDE technique can provide better insight into failure mechanisms under dynamic loads. Monitoring in real-time under dynamic loading can indicate the sequence of the occurrence of each damage mode and help us understand and model the failure mechanisms of the material. Hemann, et al. [79] studied the effect of increasing stress level on AU signals on unidirectional graphite/epoxy composite material. This was considered to be a first step towards developing real-time AU as a tool for monitoring damage under dynamic loads.

Progression of damage is monitored in real-time by observing the changes in the received AU signal during the actual test. Prior to the development of a real-time AU technique, mechanical testing was stopped to perform an AU test along

with other NDE tests before reloading the specimen to the next load level. The dynamics of the damage mechanics may be altered by interrupting the mechanical test. During the real-time AU test, the AU signals are generated and received by the AU transducers attached to the specimen while it is being subjected to increasing quasi-static loads. The sender transducer generates AU signals continuously at the rate of 1600 pulses/sec with a rise time for each pulse being less than 10 nanoseconds. The received AU signal corresponding to one of the pulse is gated in the time domain (gated time (T) = 40.96 μ sec; sampling rate = 25 Mhz) and stored every second in a separate computer file. Further analysis is done to calculate AU (SWF) parameters by the FORTRAN codes developed at Virginia Tech [32-49]. A copy of the codes with proper documentation is attached in the appendix. The received real-time AU signals contain information regarding the damage state of the specimen along with the damage events that occurred at each instant.

The real-time AU developed by the author also monitored damage accumulation continuously under cyclic loading (10 Hz, R = 0.1). The received AU signals for 64 successive pulses were gated in the time domain (T = 40.96 μ sec) and then averaged every second over ten load cycles and stored in a computer file. These averaged gated signals are representative of the damage state of the specimen at that point of its fatigue life. This is also the first major attempt in the development and application of real-time AU for continuously monitoring damage accumulation during fatigue. The real-time AU technique can be used to decipher the true nature of the damage mechanics and help in studying the failure mechanisms of composite materials by monitoring the onset and growth of each damage mode.

3. EXPERIMENTAL PROCEDURES

3.1 Material Systems

Unidirectional $[0_8]_S$ and cross-ply $[0/90]_{4S}$ ceramic composites having silicon carbide fiber and calcium aluminosilicate matrix (SiC/CAS II) were made by Corning, Incorporated, with approximately 40% fiber content and less than 1% porosity. Nicalon (SiC) fiber used to make the panels was manufactured through a polymer pyrolysis process by Nippon Carbon Co. Ltd. of Japan. Nicalon is homogeneously composed of ultra-fine β-SiC crystals with excess carbon and other elements. Nicalon fiber is highly resistant to oxidation and chemical attack and has excellent strength and modulus properties. The impregnated tow of fibers is passed through a slurry of CAS II and then wound on a drum. Unidirectional laminae are cut and laid up according to the desired stacking sequence. With the help of proper tooling, the laid-up laminate is hot-pressed for consolidation for approximately 4 hours with maximum pressure (1500 psi) and maximum temperature (1250_o C) being maintained for at least 40 minutes. Table 1 shows the constituent properties of SiC/CAS ceramic composite material system. The information regarding the manufacturing process and the constituent properties has been provided by Corning, Incorporated.

One unidirectional $[0_8]_S$ plate, 6.5" x 6.5" x 0.12", and two cross-ply $[0/90]_{4S}$ plates, 6.5" x 6.5" x 0.127" were supplied by Corning Inc.. The results of ultrasonic c-scan performed on each plate indicated a negligible amount of porosity. Ten samples were cut from each plate with a diamond saw cutter using a synthetic lubricant to avoid damage. Samples from the unidirectional plate were marked as

samples U1,..,U10. Figure 2 shows typical tensile specimen dimensions. The first cross-ply plate had an average density of 2.694 gm/cc and the samples cut from this plate were marked as C1,..,C10. The second cross-ply plate had an average density of 2.681 gm/cc and the samples were cut and marked as C11,..,C20. Samples from the second plate (C11,..,C20) were used to generate fatigue data. The difference in the average density between the plates may have been caused by the difference in prepregs. Table 2 describes the nomenclature used for different SiC/CAS ceramic composite specimens along with the type of subjected loads and heat treatments.

Additional unidirectional $[0_9]_S$ samples, G12, G14, G16, were supplied by NASA Lewis Research Center and were also manufactured by Corning, Inc.. The dimensions of these cut specimens were 6.0" x 0.5" x 0.125".

A second material system was also available for this study. Quasi-isotropic $[0/+-45/90]_{2s}$ specimens (152.4 mm x 11.8 mm x 3.4 mm) made from silicon carbide fiber and magnesium aluminosilicate matrix (SiC/MAS) were provided by Rolls-Royce [80]. Real-time AU data were recorded during static tests on samples MAS-8, MAS-11, MAS-1, MAS-3 and MAS-10. There were no coatings applied on any of these samples. Samples MAS-1, MAS-3 and MAS-10 were heat treated at 1100^0 C for 100 hours in air prior to mechanical testing.

End tabs made from high pressure cross-plied glass/epoxy laminates, (1.5" x 0.5" x 0.15"), were glued to the specimens using FM-300 adhesive and cured at 300^0 F for 2 hours. The end tabs were sanded by 180 grit emery paper along with the specimen for better bonding. End tabs were attached to prevent crushing damage when held in the grips of the testing machine.

Table 1. Constituent properties of SiC/CAS ceramic composite material system.

PROPERTY	SiC	CAS-II	Composite
Radius (μm)	7.5	-	-
Density (gm/cc)	2.55	2.76	-
Poisson's ratio	0.15	0.22	0.192 (ROM)
Coefficient of thermal expansion (x 10^{-6} / ^{0} C)	4.0	4.96	-
Volume fraction	0.4	0.6	-
Tensile modulus (GPa)	193	98	136 (ROM)
Strain to failure (%)	1.5	0.1	-

Processing temperature = 1250^0 C

Fracture energy (CAS) = 25 J/m^2.

Samples U8, U9, C8, C9 were subjected to heat treatment for 48 hours in air with the temperature maintained at 1200 ^{0} C. The reason for the heat treatment was to change the properties of the interface and thereby change the failure characteristics of these specimens. It was the author's intention to investigate the sensitivity of real-time AU by comparing the changes in the AU signals for two different failure processes.

3.2 Sample Preparation

The edges of the samples in the thickness direction were polished after attaching the end tabs to enhance the clarity of video recordings of these surfaces. The polished surfaces also produced good quality edge replications. Polishing was performed using 400 and 600 grit emery paper in succession. A final mirror-like surface was produced using diamond paste of 15 microns and then 6 microns, in succession.

Two aluminum V-notch tabs measuring 0.5" long and 0.1875" wide were glued to one side of the specimen at the gage section with a thin layer of silicone rubber. The V-notch ran along the flat surface parallel to the length. Care was taken to align the grooves of the V-notches parallel to each other at an inch apart and perpendicular to the load axis. Silicone rubber is a room temperature cured adhesive. The knife edges of the extensometer were seated in the V-notches and held in place by rubber bands during testing.

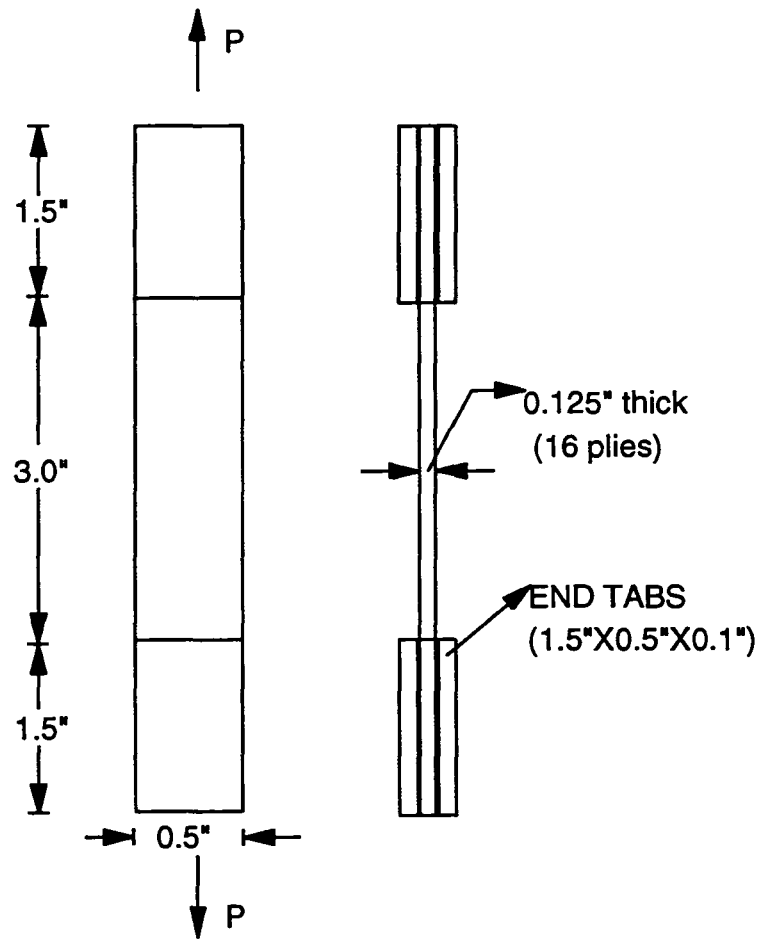

Figure 2. Detailed view of specimen dimensions.

Table 2. Experimental Program

Fiber - SiC (Nicalon) Matrix - CAS-II

Specimen dimensions - 6" X 0.5" X 0.125"

LAY-UP	NOMENCLATURE	TOTAL NOS.
$[0_8]_s$	U1..U10	10
$[0/90]_{4s}$	C1..C20	20

UNIDIRECTIONAL

SAMPLES	TYPE OF LOADING / HEAT TREATMENT
U1..U4, U10	Quasi-static ramp loading in tension to failure at room temperature (QST @ RT)
U8, U9	Heat treatment @ 1200^0 C for 48 hrs: then Quasi-static ramp loading in tension to failure at room temperature (QST @ RT)

CROSS-PLY

SAMPLES	TYPE OF LOADING / HEAT TREATMENT
C1..C3,C6,C7	QST @ RT
C8,C9	Heat treatment @ 1200^0 C for 48 hrs: then Quasi-static ramp loading in tension to failure at room temperature (QST @ RT)
C11..C20	Fatigue @ room temperature with σ_{max} = 60 %, 65%, 75%, 85% & 90% of UTS

3.3 Mechanical Testing

3.3.1 Quasi-static strength testing

A 20 kip, electro-hydraulic, servo-controlled load frame with hydraulic wedge grips was used to load the specimens in tension to failure. A right angled level was used to ensure the specimens were aligned to the load axis prior to gripping by the hydraulic wedges. Care was taken to grip all specimens in slight tension so as to avoid any chances of the specimen experiencing any compressive load. The grip pressure used was 400 psi and was sufficient to prevent any premature slipping prior to failure.

Static tests were run in load control mode at the rate of 200 lbs/min. The slow rate was chosen to enable the real-time AU system to gather as much data as possible. The strain signal from the extensometer was fed through the load frame's internal amplifier and then fed into a computer driven data collection system along with the load signal. The A/D board in the data acquisition system converted the analog signal and stored it at the rate of 5 Hz. The stored data was imported into a spreadsheet A linear regression analysis was done on the linear portion of the resulting stress-strain curve to determine the initial stiffness of the specimen.

3.3.2 Fatigue testing

A 20 kip, electro-hydraulic, servo-controlled load frame with hydraulic wedge grips was used to run tension-tension (R = 0.1), constant load amplitude fatigue tests at 10 Hz. The gripping procedure was similar to static tests. Maximum load

amplitudes were determined based on data from static strength. The load amplitude in each cycle was chosen to be a different % of the average ultimate static strength. The load amplitude for individual fatigue tests ranged from 90% to 60% so as to generate an S-N curve for the material system. Once the load amplitudes were set, the fatigue tests were interrupted only to measure static stiffness and to take edge replicas. The maximum strain was also monitored by a peak detector. The maximum strain readings were recorded by the researcher manually after a set number of elapsed cycles or when there was a sudden increase in the maximum strain caused by damage. The dynamic stiffness of the laminate was monitored by comparing the ratio of the maximum initial strain to the present strain ($\varepsilon_0/\varepsilon_i$). Since the fatigue tests were run in load control, the maximum stress remains constant and hence this ratio ($\varepsilon_0/\varepsilon_i$) indicated the normalized dynamic stiffness and was used to monitor modulus/stiffness as a function of cycles. The fatigue tests were interrupted if there was a sudden decrease in dynamic stiffness so as to enable the researcher to study the damage by other means.

3.4 Nondestructive Testing

3.4.1 Acousto-ultrasonic Technique

A block diagram of the experimental AU system is shown in Fig 1 along with an enlarged view of the transducer holder. Figure 3 shows a photograph of the experimental AU system along with a specimen held in the grips. Ultrasonic pulses were introduced into the mechanically loaded specimen through a broadband transmitting transducer, Panametrics model V133RM (2.25 Mhz/6.35 mm). The

couplant used was Sonotrace-30. A Panametrics Model 5052-AU pulser/receiver was used to generate and receive the ultrasonic signal. The receiving transducer was the same type as the transmitter.

A plexi-glass transducer holder was designed and fabricated to maintain a fixed distance between the AU transducers: 38.1 mm (1.5") apart on the opposite side of the specimen from the extensometer. The transducer holder had two counter bores to snugly fit the outer casing of the AU transducers and a small cut out window for the connectors of the transducers. Small grooves were cut at the edges of the holder to seat rubber bands so as to prevent it from slipping. The rubber bands aided in maintaining a constant pressure at the center of the transducer holder throughout the experiment.

The couplant was applied between the transducers and the specimen with the help of a syringe prior to the start of each test. Degradation of the couplant was negligible for static tests as the maximum duration of a test was 15 minutes. The pressure maintained by the rubber bands produced reproducible results during trial runs. Degradation of the couplant during fatigue tests was observed after 50000 cycles with a consequent effect upon the AU signals. Therefore, fresh couplant was applied after 30000 cycles and AU data were compared before and after the application of the fresh couplant. Negligible amount of couplant degradation was observed in few samples.

The data acquisition board used for the AU tests provided sampling rates from 156 Khz to 25 Mhz in transient mode. Sampling rates of 40, 80 and 160 Mhz were available in the time equivalent sampling mode. A sampling rate of 25 Mhz was chosen for these tests. The display software was optimized for the fastest possible up-date rate of wave-form data with a standard IBM color graphics board.

(a)

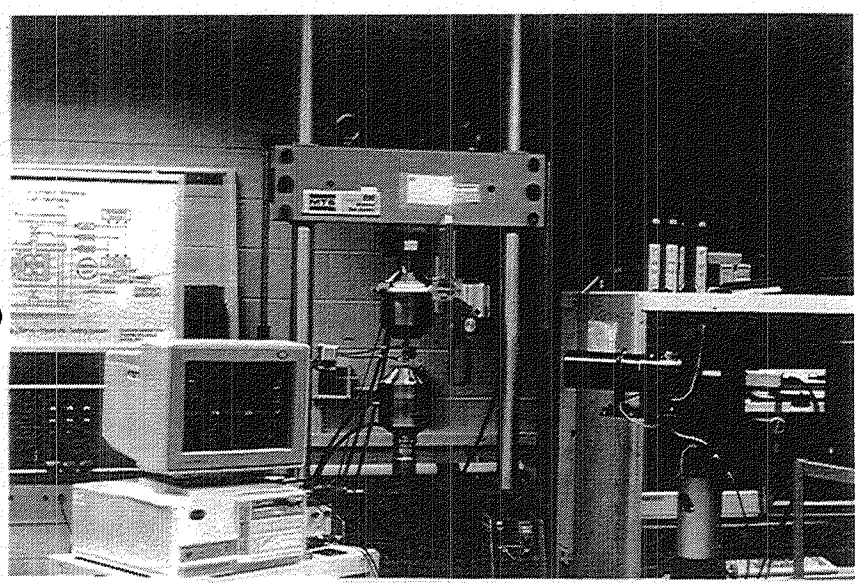

(b)

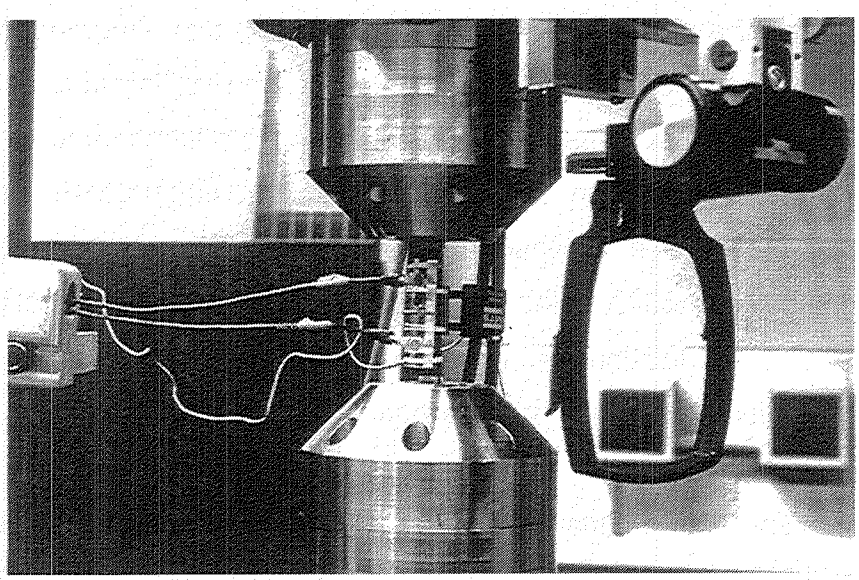

Figure 3. (a) Photographic view of real-time AU set-up. (b) Enlarged view of the transducer holder device attached to the specimen.

Update rates of 10-15 times per second were achieved in digital oscilloscope fashion. The time delay and the sweep length were controlled from the keyboard.

The data acquisition board sends a trigger pulse to trigger a high frequency electronic pulse from the pulser to the transmitting transducer. The electronic pulse energy is converted to mechanical energy on the face of the transducer plate. The mechanical excitation produced induces stress waves in the material, through the couplant. The AU stress wave interacts with the material micro-structure and damage. The motion of the stress waves is sensed by the receiver AU transducer which in turn converts the mechanical energy to an electronic signal. The received signal is amplified and sent to the A/D converter board. The A/D converter is triggered by the same trigger pulse used for the pulser unit to signal it to begin taking data. The digitized signal is displayed on the screen and can be stored for further analysis.

Two types of data records can be saved in disk files by the data acquisition software: set-up parameters and waveform data. The set-up parameter feature retains the settings for future data collections requiring the same parameter readings. Waveform data files contain the digitized waveforms. These files can be recalled by the software and displayed or the numerical information contained can be dumped directly to the CRT or the printer. The software associated with the board allows the computer to act as a digital oscilloscope, with the ability to store the waveform and perform limited frequency analysis by means of a fast fourier transform algorithm (FFT).

The preamplifier and amplifier gains for the received signal were set for each individual sample. After a group of signals was saved, the signals were input to a FORTRAN program developed at Virginia Tech [32-49] to calculate the

frequency spectra and their various moments. The FORTRAN codes are attached in the appendix for reference. The AU data were normalized with respect to the initial value of each test and plotted against stress level. The zeroth moment was found to be the most sensitive parameter of the ones studied for detection of matrix cracks and is referred to here as AU stress wave factor (SWF).

3.4.2 X-Ray Radiography

Damage modes such as delaminations and matrix cracks can be easily detected by penetrant enhanced x-ray radiography. The researcher can also locate damage by taking through-the-thickness and through-the-width X-ray radiographs and interpolating to obtain the approximate location of the damage. A zinc-iodide solution (60 gms of ZnI_2 + 10 ml water + 10 ml isopropyl alcohol + 10 ml Kodak Photo-Flo 200) was used in this study as an x-ray opaque penetrant with Kodak Photo-Flo acting as a wetting agent. This penetrant was applied over the free surface of the specimen. The specimen was left to soak in the penetrant for 24 hours to allow the penetrant to seep into the damaged areas by capillary action. Excess penetrant was removed from the free surface with acetone prior to exposure to the x-ray radiation. Obviously, one limitation of the technique is that only damage that has path(s) open to the surface will be detected.

A Hewlett Packard 43805N Faxitron series X-ray system was used to radiograph the specimens. The applied x-ray tube voltage, the exposure time and the distance from the emitting element have to be established to get a good contrast x-ray radiograph for the specimens. The specimens soaked in penetrant were placed on a Kodak M-5 double-side emulsion film at a distance of 16 inches from the emitting element. The tube voltage was set at 40 kVp and the exposure

time was set at 5 minutes to obtain high contrast contact x-ray radiographs.

3.4.3 Ultrasonic C-scan

A Sperry UM721 reflectoscope with an Automation Industries Inc., US-450 scanner was used to perform ultrasonic c-scans on the specimens. The specimens were placed on a glass plate at the bottom of the water tank. A Panametrics transducer with focal length of 1.5 inches and nominal frequency of 15 Mhz was used in a reflection mode. Ultrasonic signals reflected off the glass surface were gated with a preset threshold level. Non-conformities in the specimen such as voids, cracks, delaminations, inclusions, etc., attenuate the transmitted signal in proportion to the severity of these non-conformities.

3.4.4 Scanning electron microscope (SEM)

The specimens were cut to a 1 inch width from the failure surface by using a low speed, water cooled diamond wheel. These cut specimens were coated by gold sputtering for 2 minutes prior to insertion in the SEM test chamber. The SEM unit was a model type SX40 manufactured by International Scientific Instruments (ISI). The SEM photographs taken of the failure surface show the micro details of the failed surface.

3.4.5 Long distance optical video microscope

A Questar QM1 long-range microscope especially designed for visual and photographic focusing was used to follow damage progression along a free edge

of the specimen. The microscope was focusable in a range of 22 inches (55.88 cm) to 77 inches (195 58 cm), as measured between the front surface of the lens and the target. At 22 inches (55.88 cm) the QM1 system will resolve below 2.5 microns with proper lighting arrangement and its in-built optical system. The QM1 optical system consisted of a primary mirror, a corrector lens, and a secondary mirror mounted in the center of the corrector. The magnification range depended on the eyepiece used and varied between 5 x at 77 inches to 65 x at 22 inches. These magnifications were further increased by 1.6 x with the use of a short-focus, negative achromatic Barlow lens resulting in a magnification of 104 x for 22 inches. The QM1 system included a video recorder to record the changes occurring in the observed region which was the polished free edge of our specimen. The video recordings indicated the occurrence of first matrix cracks and their saturation. A similar system at NASA Lewis was also used to record the damage in several samples.

3.4.6 Edge replication

Edge replication makes an impression of the surface topography of a material on acetone-softened acetate film. Tests were stopped at a preset number of cycles during fatigue testing. Acetone was applied to the polished surface through a syringe and then acetate film was pressed against the polished surface. The acetone softened the acetate film and formed an impression of the free surface giving a clear view of the cracks and other damages on the free edge of the specimen. The film again hardened and set with the surface impression after the acetone evaporated.

3.4.7 Stiffness reduction

O' Brien [81], has shown that stiffness reduction could be used as an nondestructive method to monitor damage in composites. Here, fatigue tests were interrupted after a preset number of cycles and the load level was brought back to zero. The specimen was then ramp loaded to 15 % of its ultimate static strength. Strain and load signals were recorded as in the static tests with the help of a data acquisition board. A linear regression was done on the stress-strain curve to evaluate the stiffness of the laminate at that point of its fatigue life.

4. QUASI-STATIC TESTING

4.1 Introduction

Fiber reinforced ceramic matrix composites exhibit damage accumulation and progression well before ultimate failure. Although the matrix has a stiffness comparable with that of the fiber, the strain to failure of the matrix is lower than that for the fiber in brittle matrix composites (BMC). BMC experience matrix micro-cracking well before their final failure. Thermo-structural applications of such materials expose the fiber matrix interphase region to the atmosphere through these matrix micro-cracks causing oxidation at elevated temperatures. The oxidation could improve the bonding between fiber and matrix resulting in a brittle behavior. A weaker interface reduces the likelihood of catastrophic failure by allowing debonding to occur, resulting in a smooth failure. The stress level at the initiation of matrix cracking, often called the critical cracking stress, for a BMC material system is used as the critical design stress for thermo-structural applications.

Analytical and experimental investigations improve our understanding of the damage mechanisms in BMC material systems [82-111]. The observed failure mechanisms of BMC have generated much interest in fiber bridged failure modes, also called steady state cracking failure mode. The first cylindrical model using shear lag theory to predict the critical cracking stress for BMC was presented by Aveston et. al. [82]. The Aveston's model takes into account slipping along the fiber matrix interface, no-slip perfect bonding, and partial slip which is a combination of the two to predict the onset of large scale matrix cracking.

A more rigorous model was proposed by Budiansky et.al. [83] which uses a fracture mechanics approach to study the condition for the onset of matrix cracking. The two conditions considered in this model are (a) - unbonded fibers mechanically held by thermal strain mismatch and (b) - fibers weakly bonded but under initial residual tension, susceptible to debonding by localized high stresses at a crack tip. The critical conditions are established by using a generalized energy release rate formulation and the critical stresses are obtained in terms of micro-structural properties of the constituents and the interface.

Although the stresses at the onset of matrix cracking are used as a design stress for BMC, no standard technique exists to measure it. Researchers have used the stress at the start of the non-linearity of the stress strain curve for uni-axial tension loading along the fiber direction as an indicator of this critical stress. The non-linearity point is often poorly defined but is used to fit the analytical models proposed by different researchers.

Barsoum et.al. [84] have tried to determine the matrix cracking initiation stress by measuring the electrical resistance changes of a thin gold film on the tensile surface of the composite as a function of applied stress in a three point bend test. The results of the research presented here shows that real-time AU would be able to more closely identify the stress level at the onset of matrix cracking.

Available literature regarding work done on SiC/CAS BMC material systems is sparse. The few researchers [85-89] working on this material system have yet to produce conclusive results regarding the true nature of the failure mechanisms. Kim and Pagano [85] concluded that the initiation of matrix cracking for this material system is over predicted by the Aveston's model [82]. They suggested

that the deviation from linearity in the stress strain curve appeared to be the combined effect of the accumulation of small micro-cracks rather than the steady-state cracks assumed by the model.

Recent studies done by Kim [86,87] on a cross-ply SiC/CAS material system indicate the onset of micro-cracking to be independent of ply orientation. Contrary to Kim's findings, the results presented here indicate the occurrence of matrix cracks in the 90^0 plies prior to the onset of cracks in the 0^0 plies. Similar conclusions have been drawn by Wang et.al. [88] in his most recent work. The damage modes observed by Wang were transverse cracking, followed by delamination cracking, followed by fiber fracture for his lay-up of SiC/CAS material system.

This chapter describes the results of the static tests carried out along with real-time AU to study failure mechanisms in ceramic composites. The results are according to category consisting of unidirectional SiC/CAS and cross-plies SiC/CAS and quasi-isotropic SiC/MAS static tests. Static tests for heat treated specimens and their failure mechanisms are also presented.

4.2 Unidirectional SiC/CAS static tests

Sample G14 is unidirectional SiC/CAS with 18 plies. Ultrasonic c-scan results indicated no observable porosity or inclusions in the specimen. Sample G14 was quasi-statically ramp loaded in tension to 400 MPa at a constant loading rate of 90.72 kg (200 lbs)/min. The resulting stress/strain curve is presented in Figure 4. Note the start of non-linearity at 200 MPa due to large scale matrix cracking. A second linear region starts approximately 275 MPa and is more compliant than the

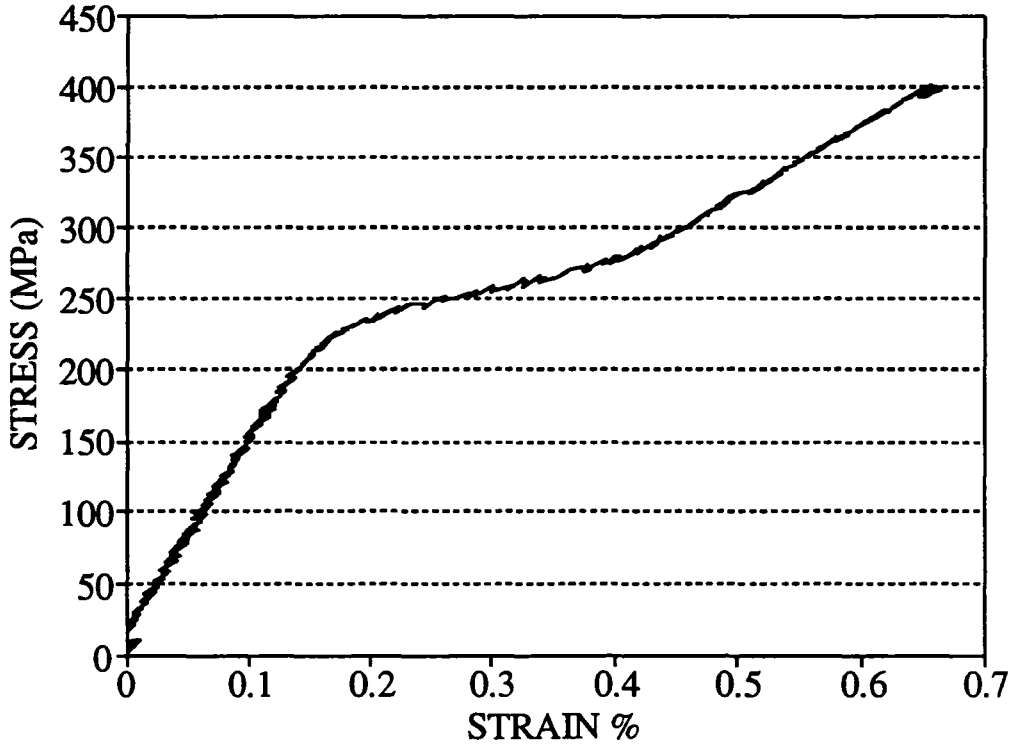

Figure 4. Stress vs strain for sample G14 (SiC/CAS, $[0_s]_s$).

initial linear zone. The normalized stress wave factor (SWF) M0 is plotted versus stress in Fig. 5. The AU readings are stored after every 60-80 MPa of increased stress levels. The SWF (M0) value recorded at 150 MPa is higher than the initial SWF (M0) value taken at zero load. This result may at first appear to be contrary to expectation that as the damage progresses the SWF values reduce. Grosskopf et. al. [40] had observed a similar increase in one AU data point just before a sharp decrease in SWF values in a few ceramic samples, depending on the load level at which the AU data were recorded. The present author investigated this apparent anomaly further rather than attributing it to scatter of data due to experimental error, fiber straightening effects or some other cause. This observation was also the author's motivation for modifying the AU system to record AU data every second making this a real-time AU technique. A sharp decline in SWF values occurs after 150 MPa that is believed to have been caused by large scale matrix cracking in the specimen. The saturation of matrix cracks occurs at 300 MPa as indicated in Fig 5. The start of the second linear zone also occurs at 300 MPa as shown in Fig. 4. The test was stopped at 400 MPa to quantify the damage on the edge surface. Figure 6 is a photo-micrograph showing the saturation of matrix cracks observed under optical microscope. The average crack spacing is found to be 140μm. Real-time AU data are recorded in the remainder of the test to obtain information about damage in real-time and thereby investigate the increase in SWF value prior to the sharp drop caused by large scale matrix cracking.

Sample U2, unidirectional SiC/CAS with 16 plies, was also quasi-statically ramp loaded in tension until failure at a constant loading rate of 90.72 kg (200 lbs)/min. Figure 7 shows the normalized SWF values taken in real-time versus stress levels. The onset of large scale matrix cracking occurs at 180 MPa, as indicated by the start of the local increase in SWF values and verified by in-situ

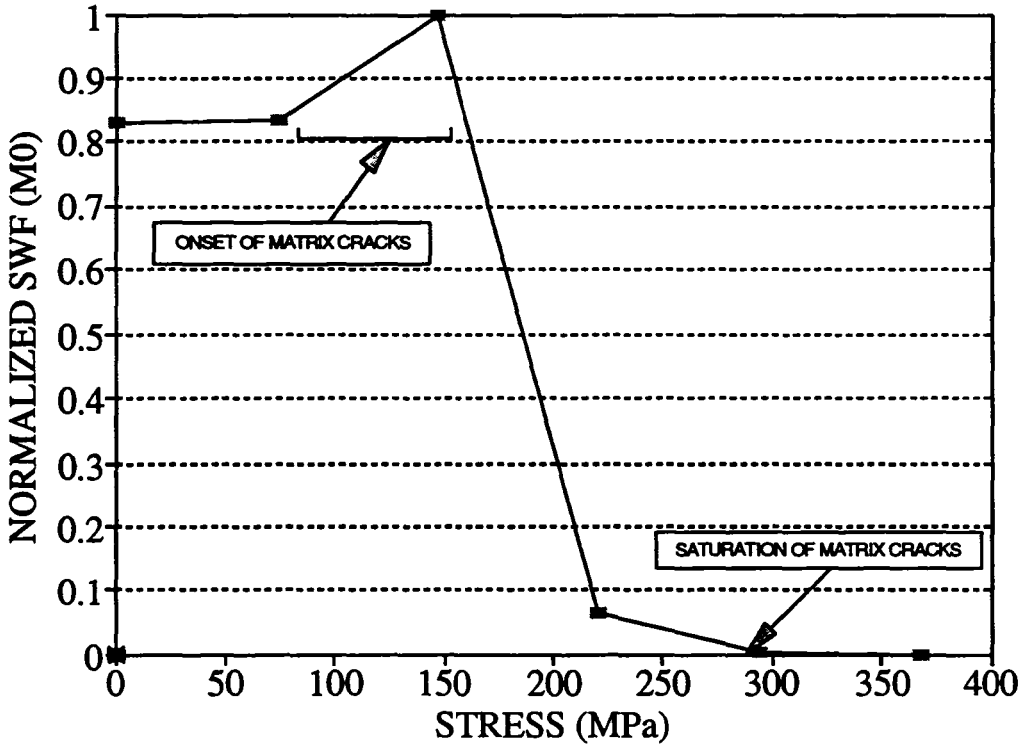

Figure 5. Normalized SWF (M0) vs stress for sample G14 (SiC/CAS, $[0_s]_s$)

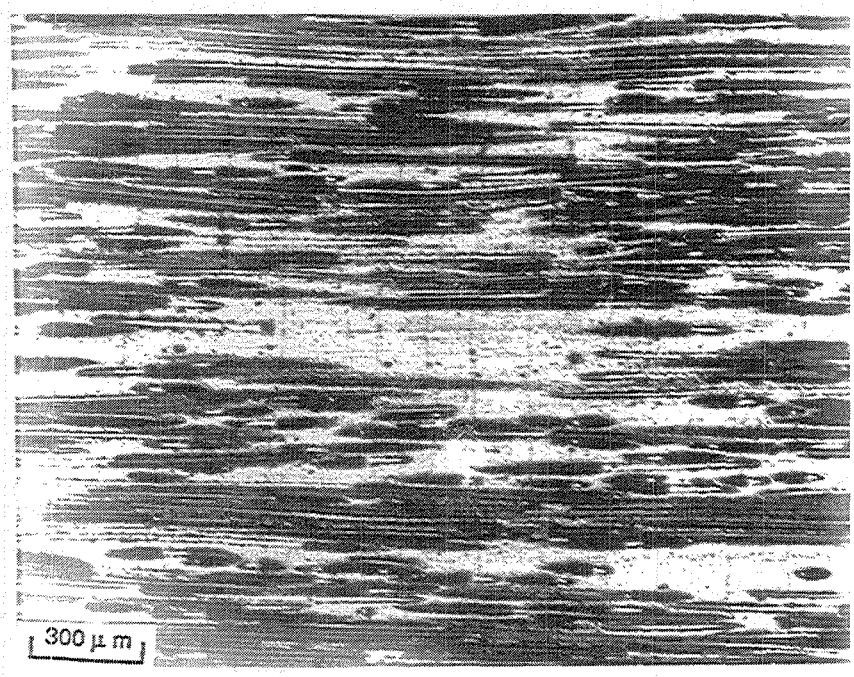

Figure 6. Photo-micrograph of the damaged surface after matrix saturation of cracks for sample G14 (SiC/CAS, $[0_9]_s$)

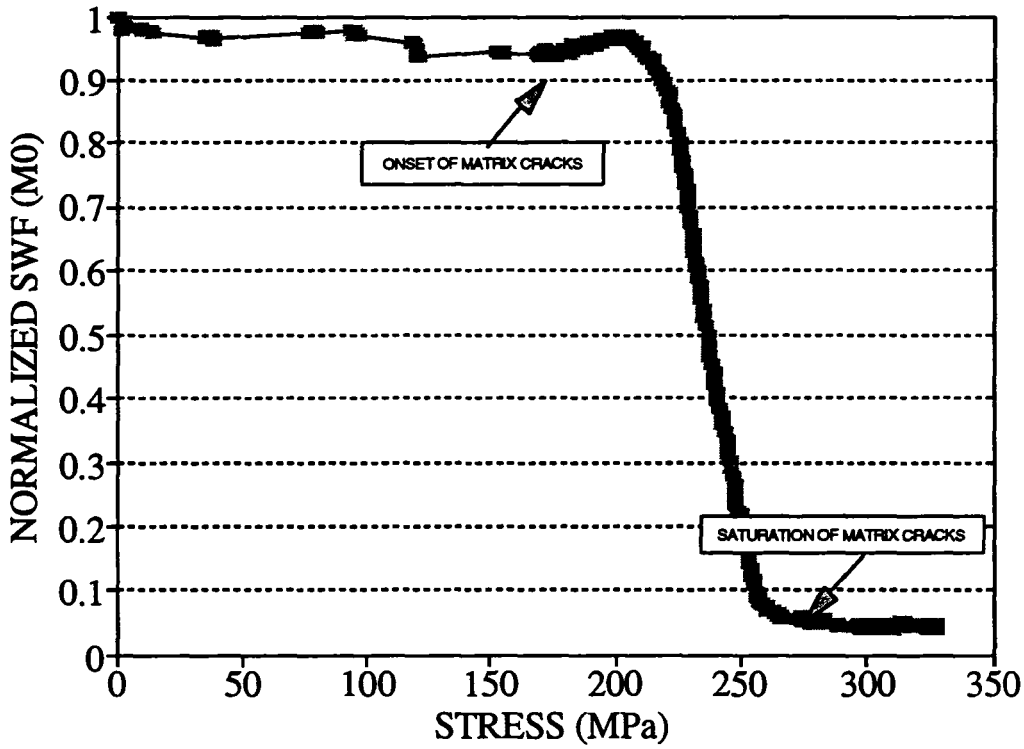

Figure 7. Normalized SWF (M0) vs stress for sample U2 (SiC/CAS, $[0_8]_s$)

optical microscope video recordings. There are at-least 20-30 AU data points having SWF values higher than the neighboring values showing a local increase and then a decrease prior to a sharp drop. Hence, the increased AU value in sample G14 most probably was not caused by experimental error but by a phenomenon observed in most specimens.

The AU receiving transducer also acts as an AE transducer receiving additional stress waves emitted by matrix cracking. The start of the nonlinear zone at 180 MPa and video recordings of first matrix cracks observed through the in-situ optical microscope were used to verify and complement AU results. In the approximate stress range between 180 and 205 MPa, the AU parameter (M0) is a combination of additional stress wave energy originating from matrix cracking and the received AU signal energy. The received AU signal energy is dependent on the efficiency of the stress wave propagation which is dependent on the damage state of the material at that stage. While there may be an inherent decrease in the AU signal energy in this stress range, it is more than offset by the increase in AE signals emitted from matrix cracking. After this range, the contribution to the SWF value due to matrix cracking decreases at a considerably faster rate than the increase in AE activity originating from the cracks. Hence, only a local increase is seen at the onset of matrix cracking. The saturation of matrix cracks takes place at approximately 260 MPa as indicated by the subsequent flat portion of the SWF graph. This corresponds to the start of the second linear zone in the stress strain curve. Figure 8 gives a view of the failure surface of sample U2 indicating significant fiber pullout.

Sample U5 was also quasi-statically ramp loaded in tension to 340 MPa at a constant loading rate of 90.72 kg (200 lbs)/min. Almost all matrix cracking has taken place by this stress level. The specimen was unloaded and reloaded to

(a)

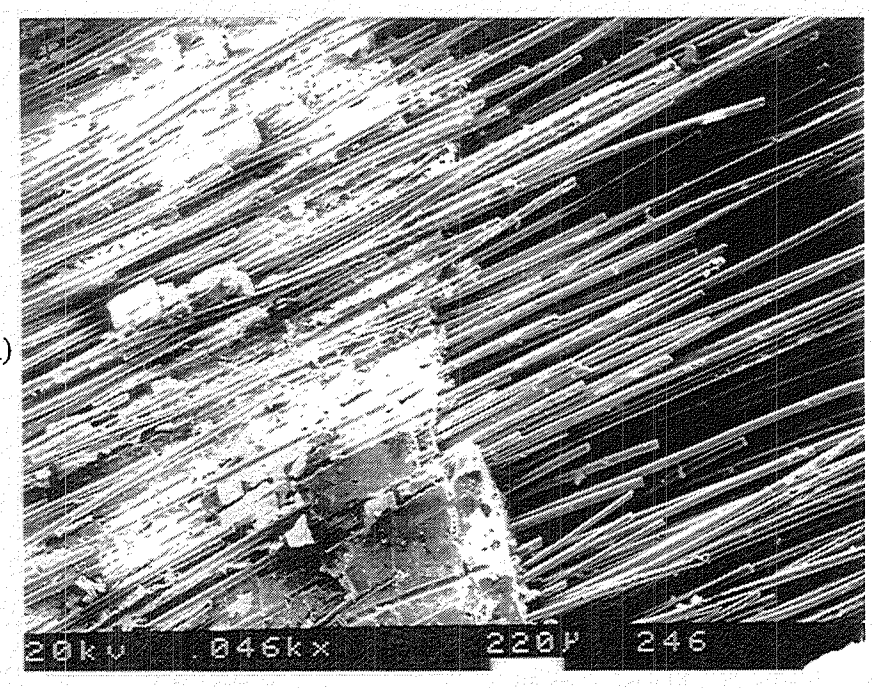

(b)

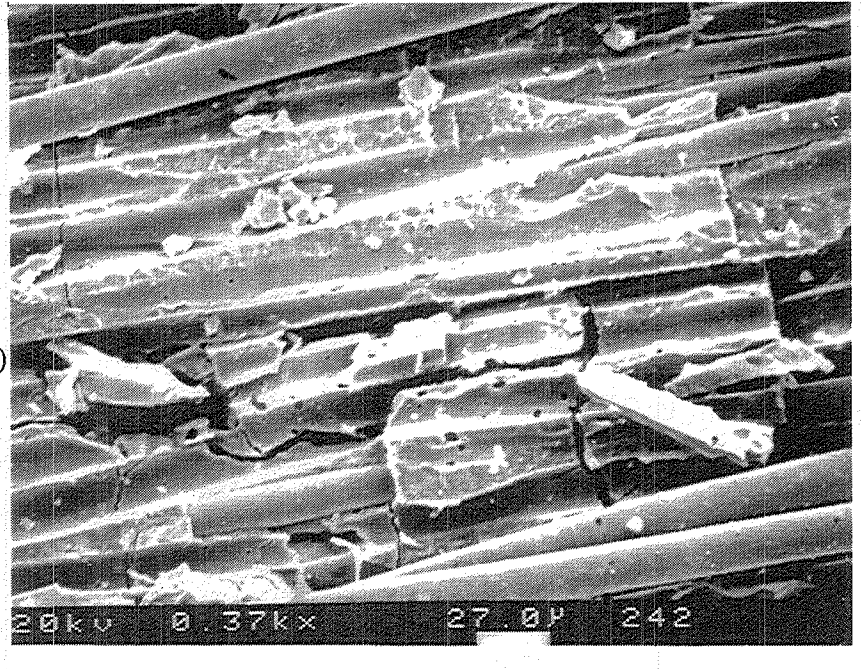

Figure 8. (a) SEM photo-micrograph of the failure surface of sample U2 (SiC/CAS, $[0_8]_s$), (b) Enlarged view of the failure surface.

failure in displacement control mode at a constant displacement rate of 0.254 mm/min so as to closely monitor the damage taking place near failure over an extended period of time.

Figure 9 shows the normalized SWF values plotted versus increasing stress during the load control mode of the sample U5 test. The local increase of SWF values occurs at 180 MPa indicating the onset of large scale matrix cracks. The saturation of matrix cracks occurs at approximately 270 MPa indicated by the start of the flat portion of the SWF curve. Sharp peaks of SWF values occurs at 240 MPa and 265 MPa, respectively. These peaks presumably are caused by a damage mode other than matrix cracking. These jumps in SWF value are caused by damaged induced acoustic emission stress waves that have been detected and analyzed by the AU system. The sharp increase in apparent SWF with a very high peak indicates stress waves generated by this damage mode have short duration and very high energy content. Because these events are so much more energetic, it is suggested that this damage mode might be fiber breakage. Further proof to verify fiber breakage would require additional testing by other techniques.

Real-time SWF values are plotted versus cross-head displacement for sample U5 loaded in displacement control mode in Fig. 10. Extensive acoustic emission (AE) generated by the occurrence of damage between 0.508 mm (0.02") and 0.762 mm (0.03") displacement of the cross-head causes the discontinuous changes in apparent SWF. The corresponding stress levels at these displacements are 350 MPa and 425 MPa, from the stress versus displacement graph of this test. Several peaks in this region are high and sharp indicating again high energy AE events, possibly fiber breaks. The smaller peaks which are about twice the order of magnitude of the input signal in terms of energy content may indicate the occurrence of some damage mode other than matrix cracking or fiber breaking.

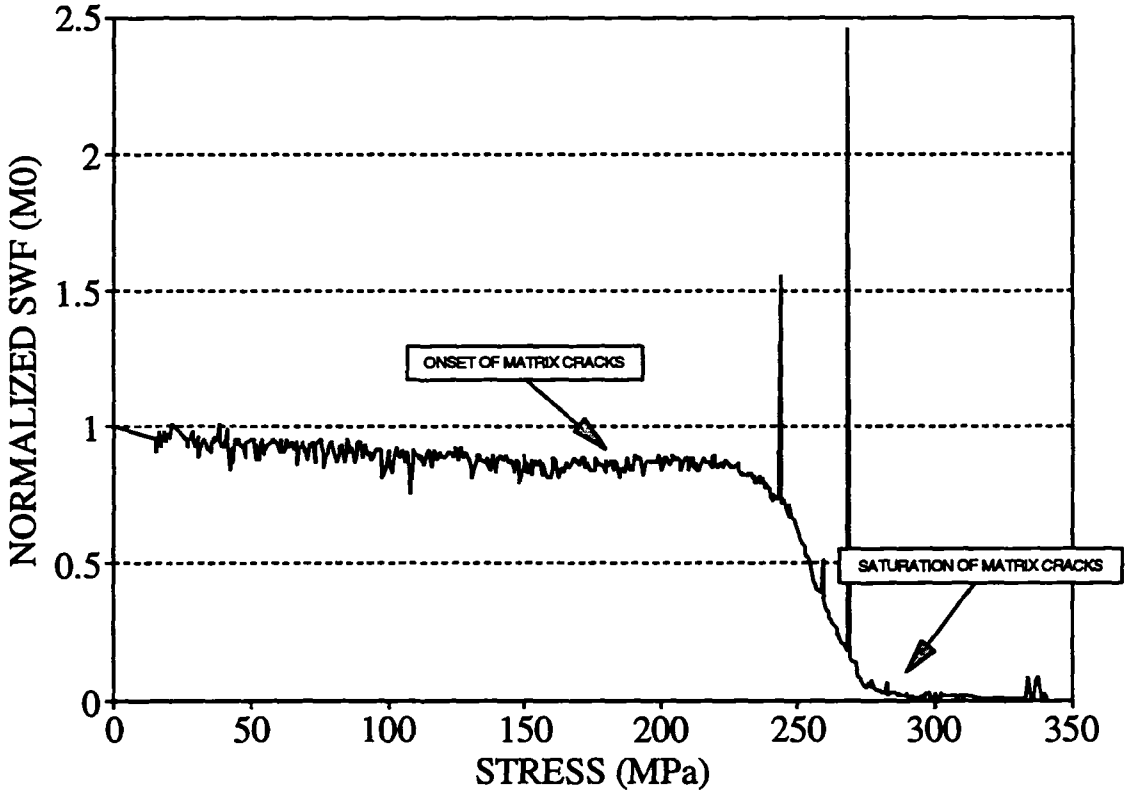

Figure 9. Normalized SWF (M0) vs stress for sample U5 (SiC/CAS, $[0_6]_s$); (loaded in load control mode till saturation of matrix cracks)

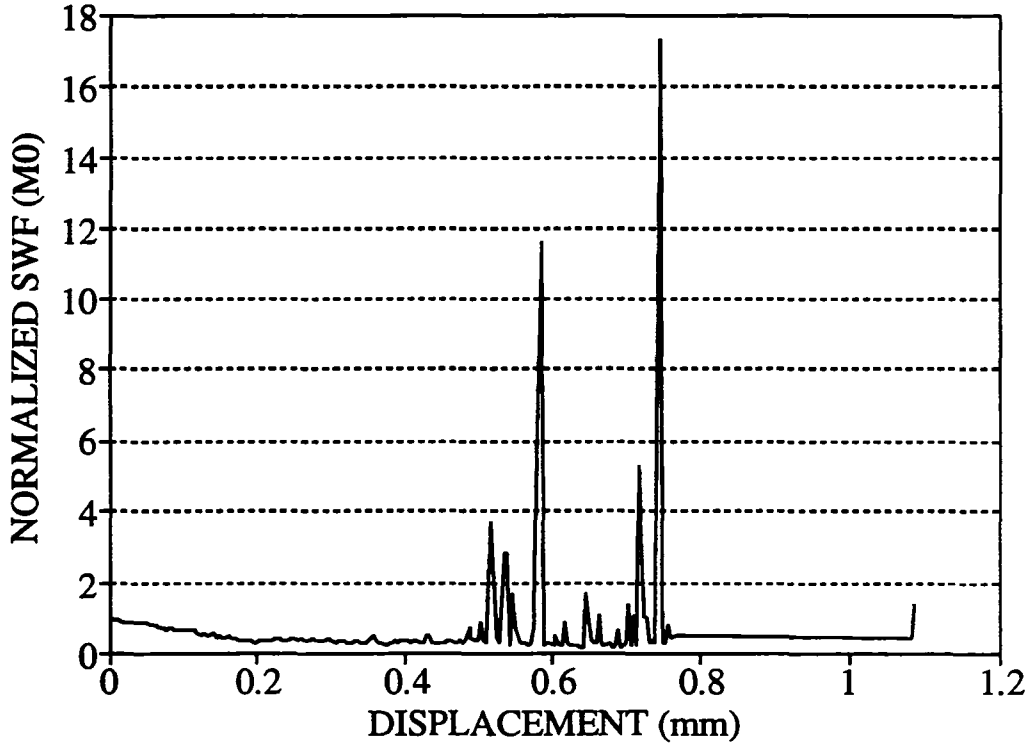

Figure 10. Normalized SWF (M0) vs displacement for sample U5
(SiC/CAS, $[0_8]_s$); (loaded in constant displacement control mode till failure)

However, this possibility must be studied further. The sharp peaks between 0.508 mm (350 MPa) and 0.762 mm (425 MPa) indicate large scale fiber breaks during the catastrophic failure of the specimen.

Sample U4 was quasi-statically ramp loaded in tension until failure at a constant loading rate of 90.72 kg (200 lbs)/min. Figure 11 shows normalized SWF values versus stress levels. The onset of large scale matrix cracks occurred at 165 MPa, as indicated by the subsequent sharp decline (65% drop) in SWF value. The normalized SWF graph also shows a decrease of 15% in the range of 80 MPa to 165 MPa indicating occurrence of "early" matrix cracking perhaps due to flaw distribution in this specimen. A local increase in SWF values was not observed in this specimen prior to the large scale matrix cracking. Figure 12 shows the stress strain graph for sample U4. The start of the first drop in SWF values at 80 MPa along with the deviation from the initial linear portion of the stress strain curve and video recordings of first matrix cracks observed through the in-situ optical microscope were used to verify and complement AU results. The saturation of matrix cracks takes place at approximately 300 MPa as indicated by the subsequent flat region of the curve of SWF and is verified by the start of the second (approximately) linear zone in the stress strain curve. Finally, an abrupt change in the rate of decrease of SWF values occurs at approximately 360 MPa. The drop in SWF values was about 10%. This specimen failed in the region between the two transducers, while the other specimens failed outside this region. Hence in this test, AU served as a warning for the impending final failure occurring about 25 MPa prior to failure. Failure occurred at 390 MPa with 0.7% failure strain.

A similar test was run on sample U10. Figure 13 shows the normalized SWF values plotted with increasing stress level in load control mode for sample U10. The first decrease (20% drop) in SWF values began at 60 MPa followed by

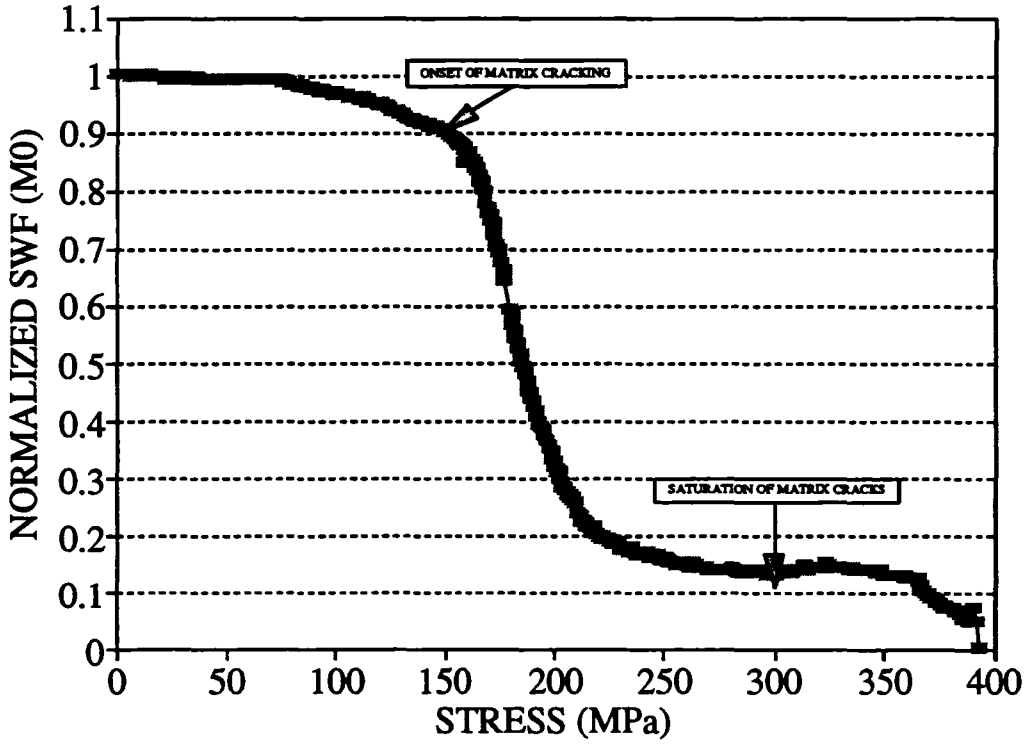

Figure 11. Normalized SWF (M0) vs stress for sample U4 (SiC/CAS, $[0_4]_s$)

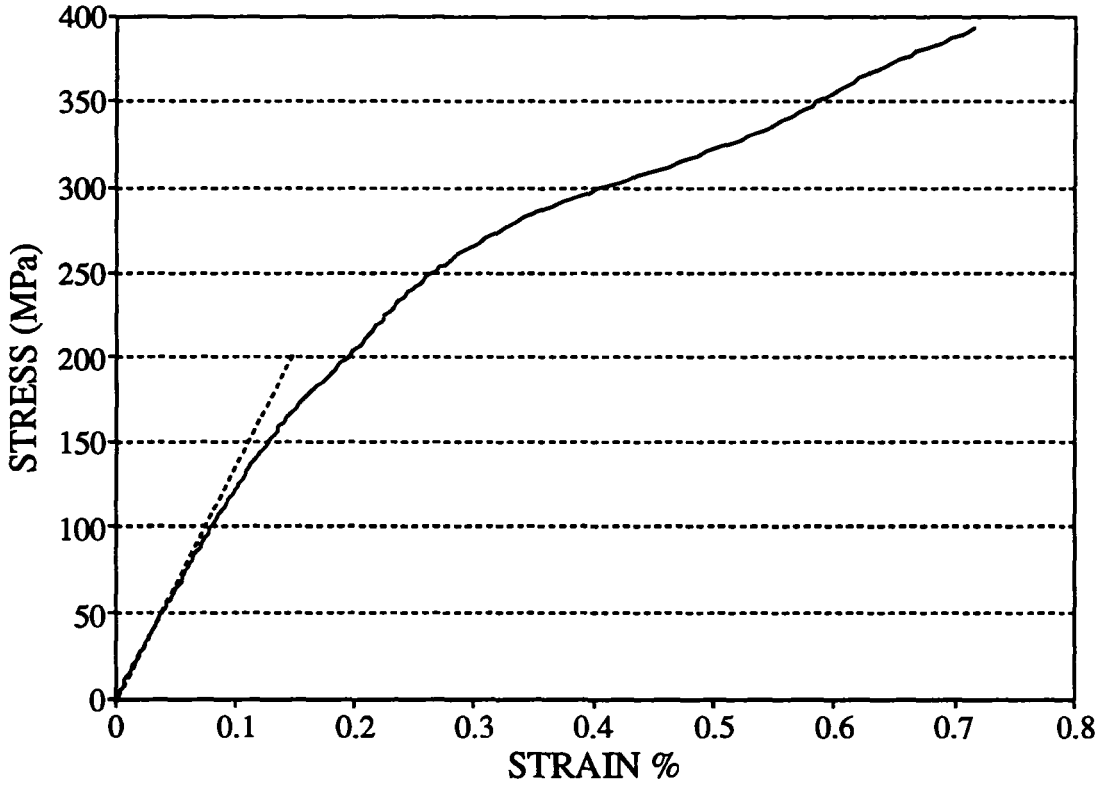

Figure 12. Stress vs strain for sample U4 (SiC/CAS, $[0_8]_s$)

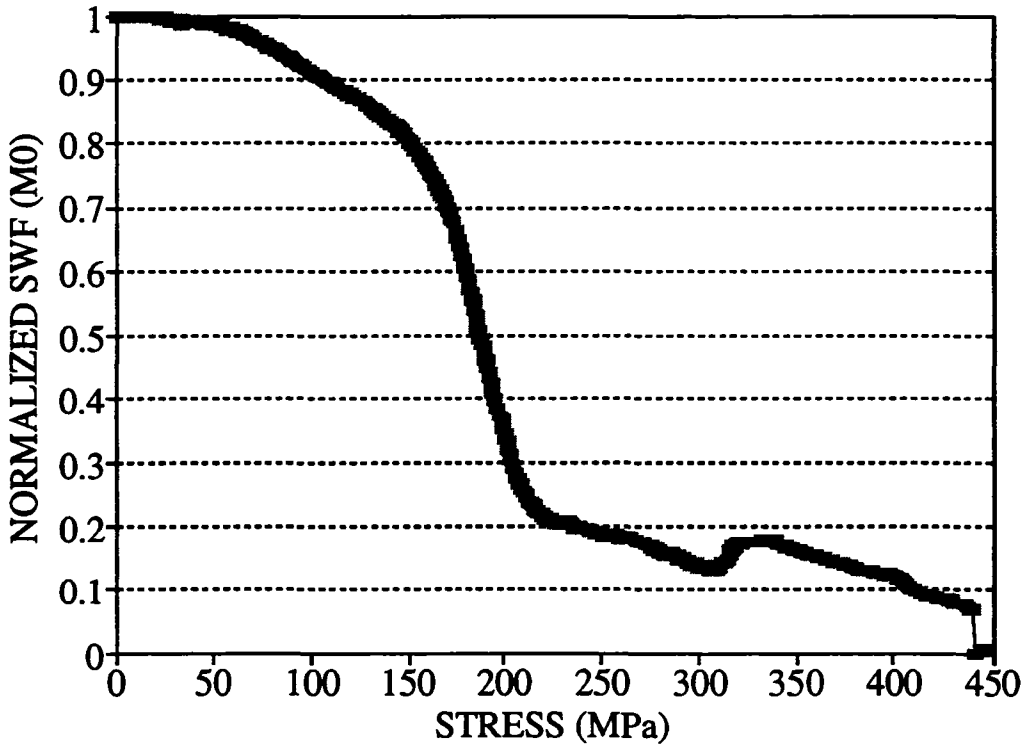

Figure 13. Normalized SWF (M0) vs stress for sample U10 (SiC/CAS, $[0_8]_s$)

a sharper rate of decline (65% drop) in SWF values beginning around 170 MPa and indicating the onset of large scale matrix cracks. The saturation of matrix cracks occurred at around 300 MPa as verified by the start of the second linear zone in the stress strain curve. Again, there is an abrupt change in the rate of decline of SWF values (10% drop) about 25 MPa prior to the final failure at 440 MPa with a failure strain of 0.85%.

Samples G12, G16, U1, and U3 showed similar results and hence are not presented here. Table 3 presents the test results for the static tests for SiC/CAS. A graph of ultimate strength of unidirectional $[0_8]_s$ SiC/CAS specimens subjected to similar test conditions versus the initial SWF (M0) values is presented in Figure 14. Generally, the higher the initial SWF value, the better is the material in terms of having a lesser number of initial flaws and hence the higher is the ultimate static strength. For these materials, the initial AU value is a good measure of the damage state of the material prior to loading. The gains set for AU signals of sample U1 were different from the rest of the samples tested. Samples U5 was stopped after saturation of matrix cracks and then run at constant displacement rate to failure and hence samples U1 and U5 data are not included in this graph. Samples U8 and U9 were heat treated and their results are presented in the next section.

4.2.1 Heat treated unidirectional $[0_8]_s$ SiC/CAS static tests

Samples U8 and U9 were heat treated in an oven for 48 hours at a temperature of 1200^0 C. The heat treatment was administered to produce oxidative embrittlement of the interface and thereby cause a change in failure mechanisms in the SiC/CAS specimens. The purpose of this procedure was to evaluate the sensitivity of the real-time AU technique in detecting and monitoring

Table 3. Quasi-static Test Results

Fiber - SiC (Nicalon) Matrix - CAS-II

Specimen dimensions - 6" X 0.5" X 0.125"

LAY-UP	HEAT TREATMENT	ULTIMATE STATIC STRENGTH (σ_u)	FAILURE STRAIN (% ε_f)
$[0_8]_S$	NO	400 MPa	0.8 %
$[0_8]_S$	YES	210 MPa	0.54 %
$[0/90]_{4S}$	NO	163 MPa	0.6 %
$[0/90]_{4S}$	YES	63 MPa	0.12 %

The averaged values of the results are shown here.

Heat treated at 1200^0 C for 48 hours.

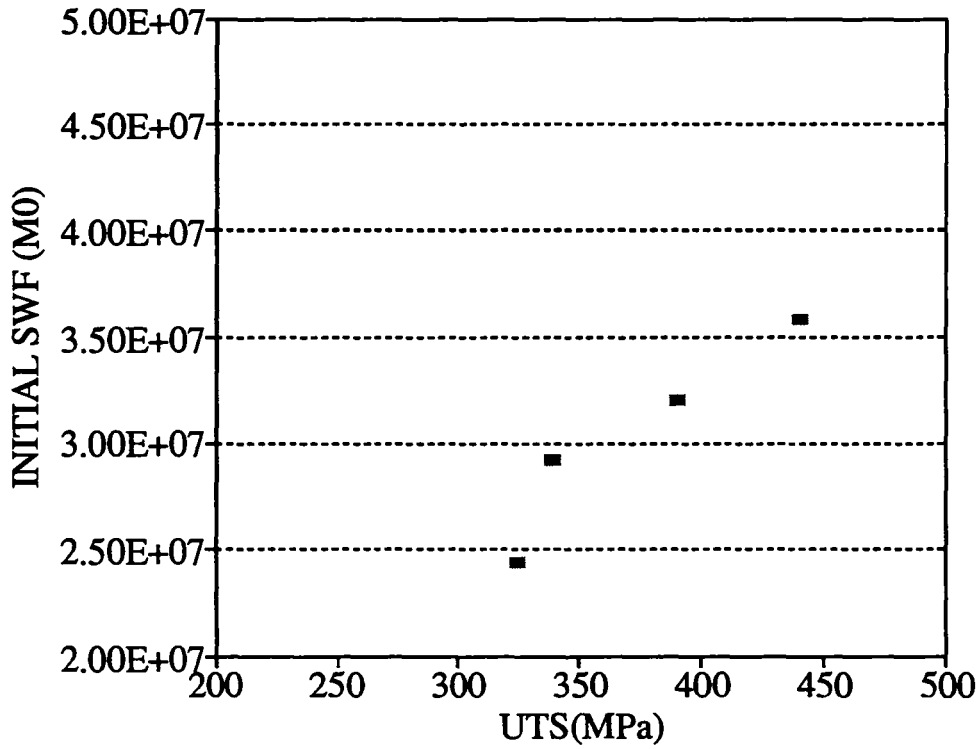

Figure 14. Initial SWF (M0) vs ultimate tensile strength of unidirectional samples (SiC/CAS, $[0_8]_s$)

the changes in the failure process.

Sample U8 was quasi-statically ramp loaded in tension to failure in load control at 200 lbs/min. Normalized SWF (M0) values drop by 60% in the stress range of 100 MPa to 190 MPa as shown in figure 15. Following this drop in AU values there is a small local increase because of increased AE activity. The final catastrophic failure occurs instantaneously at 230 MPa with a failure surface indicating brittle fracture with very little fiber pull-out.

A similar test was performed on sample U9. Figure 16 indicates a decrease of 55% in normalized SWF values between 100 MPa and 190 MPa. Catastrophic failure occurs at 195 MPa after a small local increase in SWF values. Again the failure surface indicated negligible fiber pull-out. Figure 17 shows the stress strain behavior of sample U9. The nonlinearity in the stress strain curve occurs at 100 MPa and is attributed to the onset of matrix cracking. A similar failure strain of 0.5% was observed in both samples. The failure surface and its location for samples U8 and U9 are shown in Fig. 18.

4.3 Failure process of Unidirectional $[0_8]_s$ SiC/CAS under static loads

The first damage mode observed in unidirectional ceramic composites subjected to increasing tensile loads is the development of parallel transverse matrix cracks occurring perpendicular to the fiber and the load axis. Prior to the onset of such cracking, the stress-strain response is linear and the slope of the curve is the elastic modulus of the composite laminate (E_c) given by a simple rule

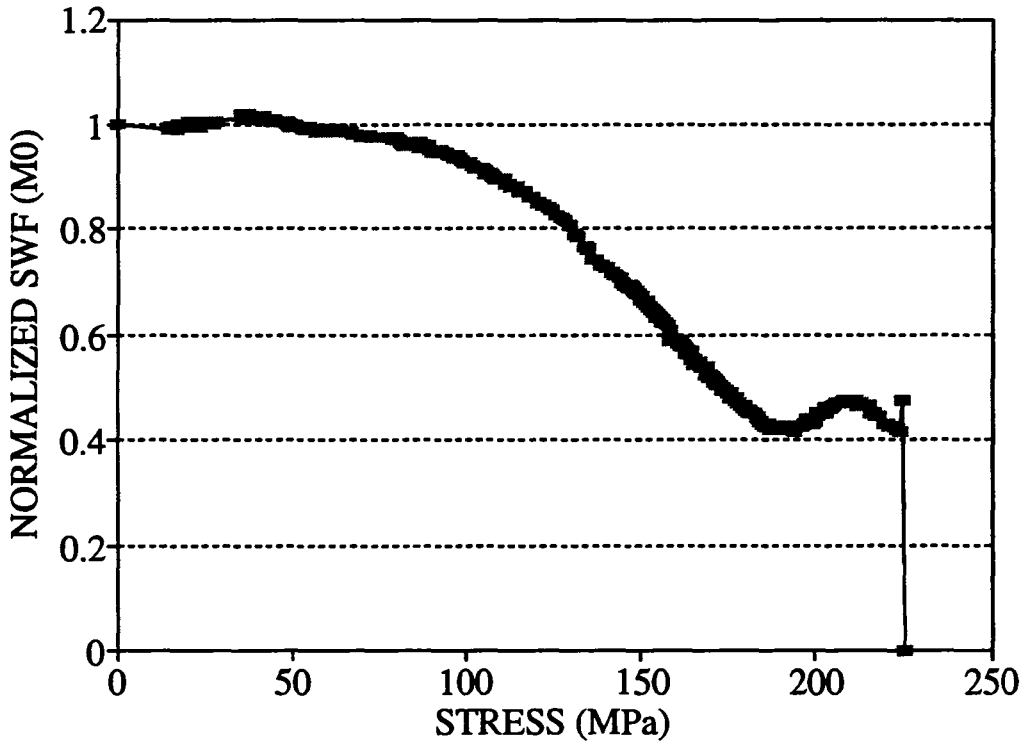

Figure 15. Normalized SWF (M0) vs stress for sample U8 (SiC/CAS, $[0_8]_s$) (Heat treated at 1200°C for 48 hrs.)

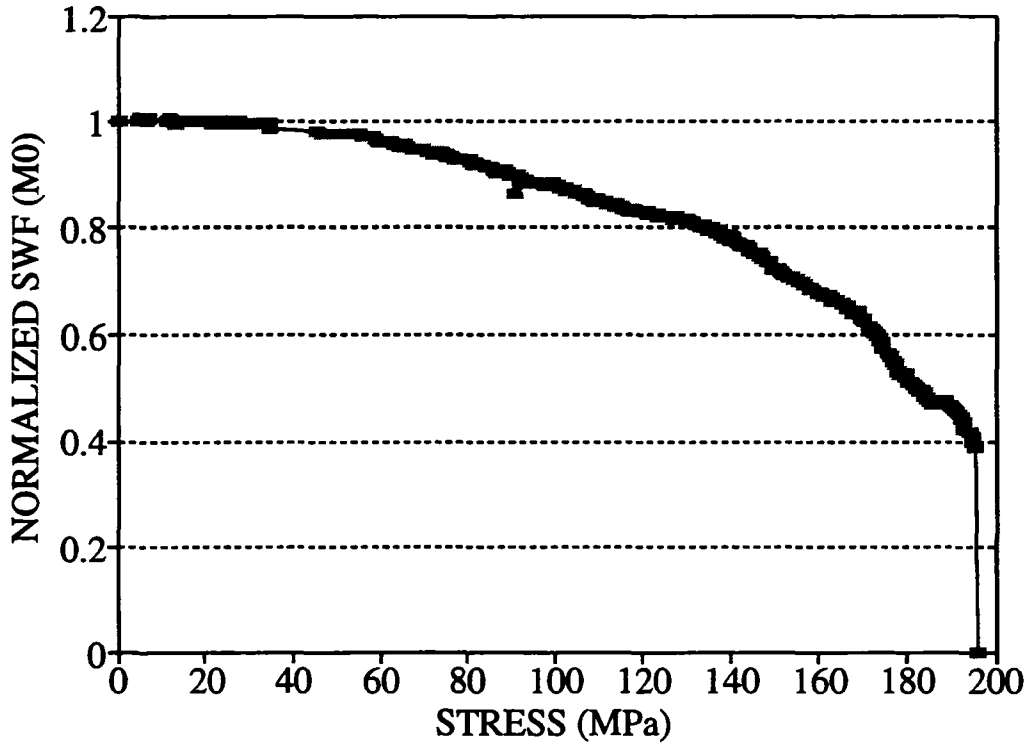

Figure 16. Normalized SWF (M0) vs stress for sample U9 (SiC/CAS, $[0_8]_s$) (Heat treated at 1200°C for 48 hrs.)

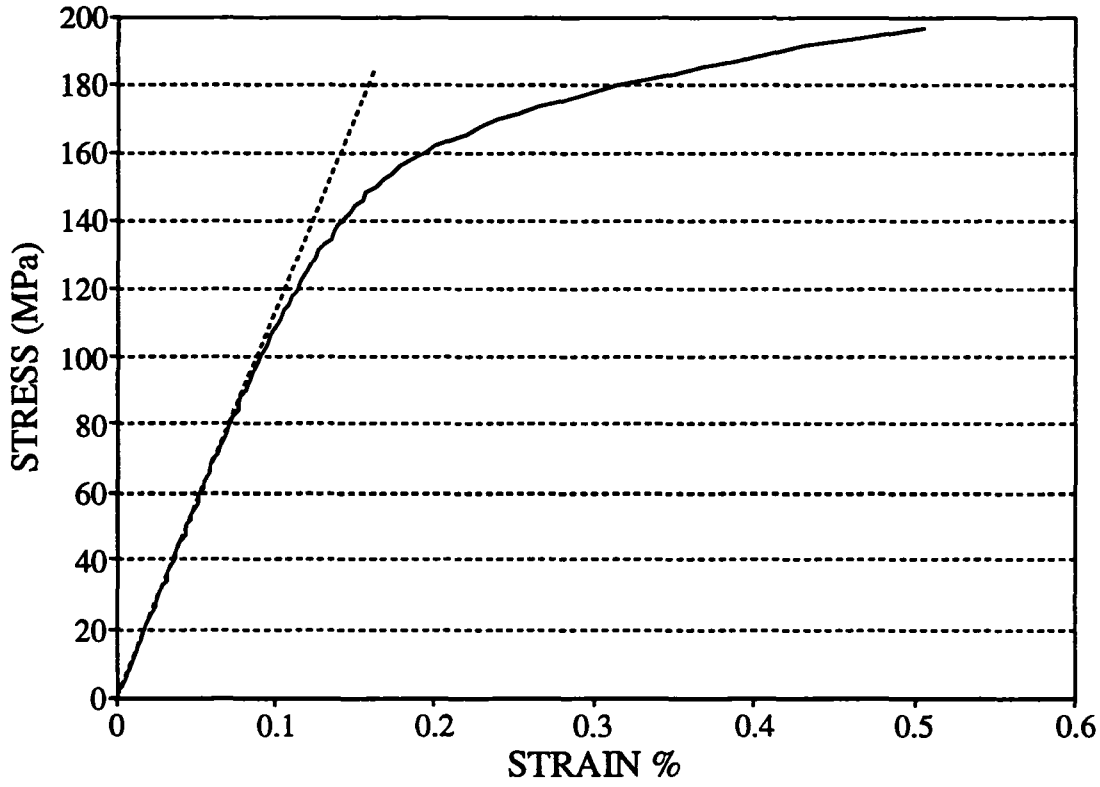

Figure 17. Stress vs strain for sample U9 (SiC/CAS, $[0_a]_s$)
(Heat treated at 1200°C for 48 hrs.)

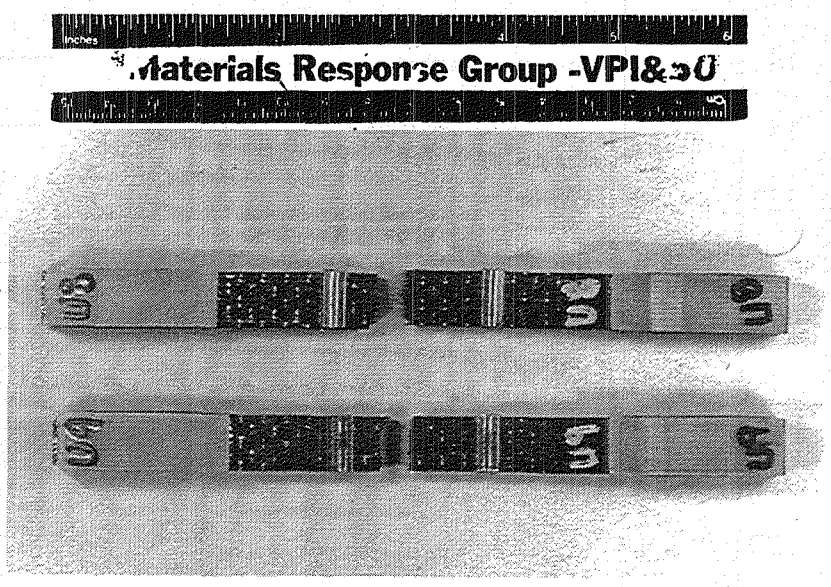

Figure 18. Photograph of the failed heat treated specimens U8 and U9, (SiC/CAS, $[0_8]_s$)

of mixtures ($E_c = v_f E_f + v_m E_m$). The experimental value of E_c = 130 GPa is comparable to that calculated from the rule of mixtures, E_c = 136 GPa. Matrix cracking occurs over a stress range in real materials. Once the matrix cracking saturates, that is, attains a constant density, the majority of the load is carried by the fibers till the final failure of the laminate. The existing analytical models for predicting critical matrix cracking stress, ultimate tensile strength for unidirectional ceramic composites and their underlying assumptions are presented below for comparison with AU and static results.

Aveston et.al. [82] have used a shear lag model with a stress based failure criterion to predict the critical cracking stress for a brittle matrix composite. Budiansky et. al. [83] refined the Aveston's model by using a fracture mechanics approach with the shear lag model to predict the lower bound for steady state matrix cracking. The inherent assumption of steady state matrix cracking is that parallel transverse matrix cracks occur instantaneously at σ_{cr} and that these cracks bridge all the fibers. Observations in real materials show a stress range over which matrix cracks develop and saturate. The model also takes into account the mismatch in the thermal coefficients of expansion of the fiber and the matrix which causes residual stresses, at room temperature. Processing temperatures of SiC/CAS laminates is about 1300°C (ΔT = -1275°C). Assuming Poisson's ratio (υ) of fiber and the matrix to be the same, the residual axial stress (σ_{ma}^{res}) in the matrix is given by [83] :

$$\sigma_{ma}^{res} = \frac{\xi_1 E_m E_f v_f (\alpha_f - \alpha_m) \Delta T}{\xi_2 E_c (1-\upsilon)} \tag{4.1}$$

where E_f, α_f and E_m, α_m are the elastic modulus and coefficient of thermal expansion of the fiber and matrix respectively and v_f is fiber volume fraction. The

residual radial stress (σ_{mr}^{res}) at the fiber/matrix interface is given by :

$$\sigma_{mr}^{res} = -\frac{E_f \nu_f (\alpha_f - \alpha_m) \Delta T}{2\xi_1 (1-\upsilon)} \tag{4.2}$$

where,

$$\xi_1 = 1 - \frac{(1-2\upsilon)}{2\,(1-\upsilon)} \left(1 - \frac{E_c}{E_f}\right) \tag{4.3}$$

$$\xi_2 = \frac{1}{2} \left(1 + \frac{E_c}{E_f}\right) \tag{4.4}$$

The Budiansky model predicts the critical stress σ_{cr} to be:

$$\sigma_{cr} = \left[\frac{6\tau\gamma_m \nu_f^2 E_f E_c^2}{(1-\nu_f) E_m^2 r}\right]^{\frac{1}{3}} - \frac{\sigma_{ma}^{res} E_c}{E_m} \tag{4.5}$$

SiC/CAS composite material system has a tensile residual stress ($+\sigma_{ma}^{res}$) in the longitudinal/axial direction that lowers the critical cracking stress, unlike a SiC/LAS material system. A compressive radial pressure ($-\sigma_{mr}^{res}$) at the interface increases the sliding stress τ and thereby increases the critical cracking stress (σ_{cr}). SiC/CAS ceramic material system has such a compressive pressure at the interface enhancing sliding resistance.

Computational results suggest the critical cracking stress level for a unidirectional $[0_8]_s$ SiC/CAS composite is **207 MPa**. The input data used for the

constituent properties were provided by Corning Inc. and are as follows: radius of fiber, $r = 7.5\mu m$; Elastic modulus of the matrix, $E_m = 98$ GPa ; Elastic modulus of the fiber, $E_f = 193$ GPa ; Elastic modulus of the composite (rule of mixtures), $E_c = 136$ GPa ; fiber volume fraction, $v_f = 0.4$; Poisson's ratio, $\upsilon = 0.22$ (same for fiber and matrix); Coefficient of thermal expansion, $\alpha_f = 4.0 \times 10^{-6} / {}^0C$ and $\alpha_m = 4.96 \times 10^{-6} / {}^0C$; matrix fracture energy, $\gamma_m = 25$ J/m^2; interfacial sliding stress, $\tau = 17$ MPa , [90]; and $\Delta T = -1275\ {}^0C$.

Flaws introduced during processing are crack initiation sites and at the critical cracking stress level (σ_{cr}) the first few cracks appear. The stresses in the matrix at the cracked matrix plane become zero and the additional load is now being shared by the bridged fibers. The stress in the matrix recovers its original pre-cracked value $\sigma_m = \sigma E_m/E_c$ over a distance l_s called the slip length due to sliding resistance at the fiber-matrix interface (σ is the global stress applied to the laminate). The recovered stress in the matrix at a distance of a slip length (l_s) is large enough to cause another transverse matrix crack. This process continues till the slip lengths overlap resulting in a saturation of matrix cracks parallel to each other at a distance of $X = 2l_s$ called the crack spacing. Real materials do not show equal crack spacing because of the statistical flaw distribution in the material. The slip length (l_s) can be approximated theoretically by the force balance equations ($l_s = r\, \sigma^{cr}\, E_m\, (1 - v_f) / 2\, \tau\, E_c\, v_f$).

The interfacial sliding stress can be calculated from the experimentally observed matrix crack spacing, the critical cracking stress level and the material constituent properties and is given by [82] :

$$\tau = \frac{\beta r E_m \sigma^{cr} (1 - v_f)}{2 v_f E_c X} \tag{4.6}$$

The average matrix crack spacing used for this calculation is 140μm obtained from the tests and $\beta = 1.337$ [91] . The sliding stress calculated is : τ = 8.25 MPa. This value is half the value of τ reported by Corning, Inc. and used in the calculation of critical cracking stress. This may be due to the fact that the constituent properties used in the calculations may not be the same as the actual in-situ properties. The constituent materials might be different than reported or matrix re-crystallization could take place during processing of these materials. The inherent simplified assumptions could also contribute to this discrepancy.

The SiC/CAS material system has a weak interface. This is desirable, since the propagating matrix cracks debond the fiber-matrix interface and thereby increases the effective unsupported length of the bridged fibers. This causes an increase in the total composite strain before failure. A few fiber breaks also occur along with the matrix cracks. The load normally carried by the broken fiber at that plane is shared by neighboring continuous fibers. This contributes to an increase in global composite strains. The increase in the composite strains due to increase in unsupported length of the fiber along with accumulation of matrix cracks and the additional strains caused by the few fiber breaks are responsible for the non-linear behavior of the stress strain curve. At the saturation stress level the majority of the load is carried by the fibers. The second linear zone of the stress strain curve originates at the saturation stress level. The upper bound for the slope of the second linear portion is given by $v_f E_f$. The observed experimental curve in this range is more complaint than this. The few fiber breaks occurring during matrix cracking is unaccounted for, and hence the slope is lower than $v_f E_f$.

Curtin [92] has based his ultimate strength model for a brittle matrix composite upon weakest link statistics. His assumptions include taking the sliding

stress and debond energy to be negligible and the fibers to be non-interacting. The load from a broken fiber site is transferred with the help of matrix through the sliding stress with global load sharing. A fiber is allowed to break more than once due to reloading of the fiber through the sliding stress (τ). The pull-out length and in-situ strength of a fiber can directly be related to the sliding stress. The ultimate strength based on these assumptions is [92]:

$$\sigma_u = v_f \sigma_c \left[\frac{2}{(m+2)}\right]^{\left\{\frac{1}{(m+1)}\right\}} \left[\frac{m+1}{m+2}\right] \tag{4.7}$$

where m is the Weibull shape parameter and σ_c is the characteristic fiber strength.

$$\sigma_c = \left[\frac{\sigma_0^m \, \tau \, L_0}{r}\right] \tag{4.8}$$

where σ_0 and L_0 are scale parameters based on the in-situ strength distribution of the fibers. The ultimate strength prediction from equation (4.7) is σ_u = 525 MPa based on the in-situ strength parameters σ_c = 2.0 GPa and the shape parameter m = 3.6 [90]. The experimentally observed values are less than 450 MPa for the unidirectional SiC/CAS material system. Hence, this model can be used only to obtain an upper bound for estimation of the ultimate strength.

The predictions of the Budiansky model for critical matrix cracking stress is higher than the AU results. The onset of matrix cracking is the design stress used for thermo-structural applications. Hence, AU results could be used to evaluate this stress level instead of the analytical models for a safer design of the structure operating at elevated temperatures.

The ultimate strength of heat treated specimens is reduced by

approximately 50% due to heat treatment. The change in the interphase due to oxygen ingression hinders interface debonding. The matrix cracks propagate through the fibers causing a brittle failure with negligible fiber pull-out.

4.4 Cross-ply $[0/90]_{4s}$ SiC/CAS static tests

Sample C5 is cross-ply SiC/CAS with 16 plies. Figure 19 shows the normalized SWF values versus stress level. A sharp drop of SWF values with increasing stress level observed at 70 MPa coincided with the onset of large scale matrix cracking in the 90^0 plies. The stress/strain graph shown in Fig. 20 for sample C5 indicates the start of non-linearity at approximately 70 MPa. The deviation from the initial linear portion of the stress strain curve and video recordings of first matrix cracks observed through the in-situ optical microscope were used to verify and complement the AU results. The recorded SWF values remain fairly constant over a very narrow range at about 95 MPa (as seen under enlarged scale) before being followed by another sharp decrease in value. This second decrease is attributed to matrix cracking in the 0^0 plies followed by the saturation of matrix cracks in the 0^0 at 150 MPa as indicated by the relatively constant SWF values following 150 MPa. The major share of the load is carried by the 0^0 plies after large scale matrix cracking of 90^0 plies has taken place prior to the onset (95 MPa) of matrix cracking in the 0^0 plies. The actual stress level for 8 plies of 0^0 is 190 MPa and is close to the stress level for the onset of large scale matrix cracking in unidirectional samples. The stress strain graph after 150 MPa is linear indicating saturation of matrix cracks in all plies and that the load is being carried by the fibers in the 0^0 plies till failure.

Sample C2 is also cross-ply SiC/CAS with 16 plies. Figure 21 shows

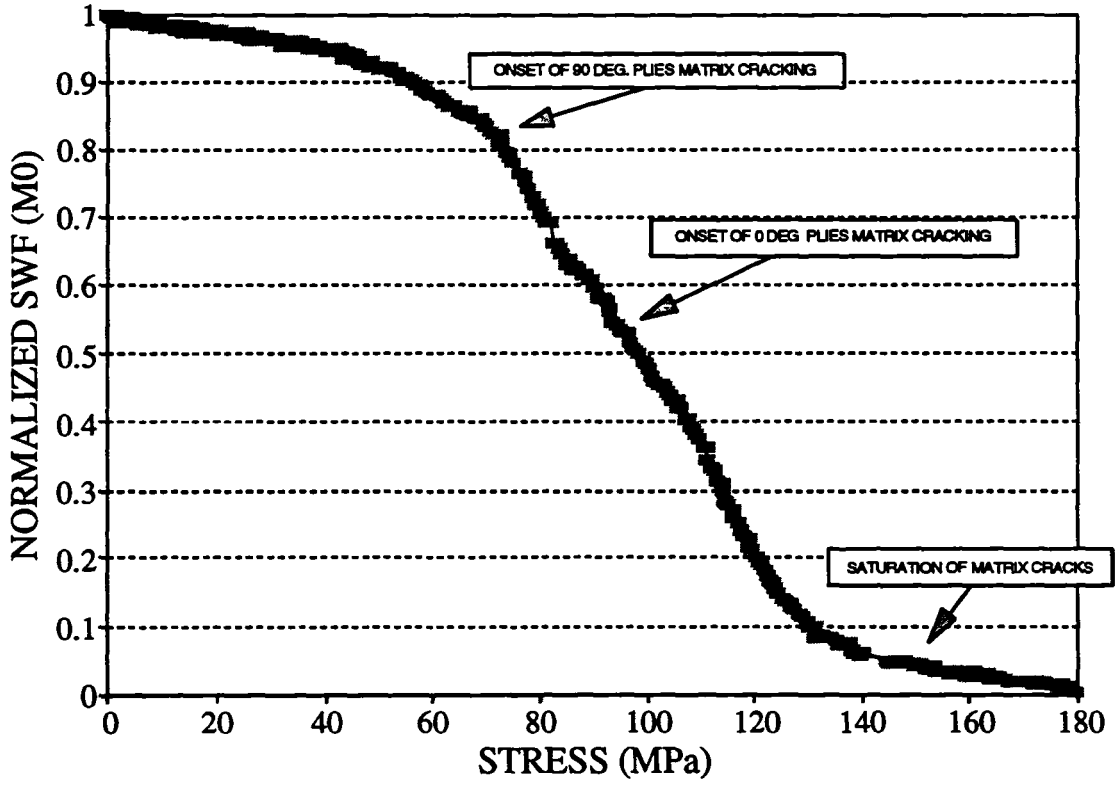

Figure 19. Normalized SWF (M0) vs stress for sample C5 (SiC/CAS,$[0/90]_{4s}$)

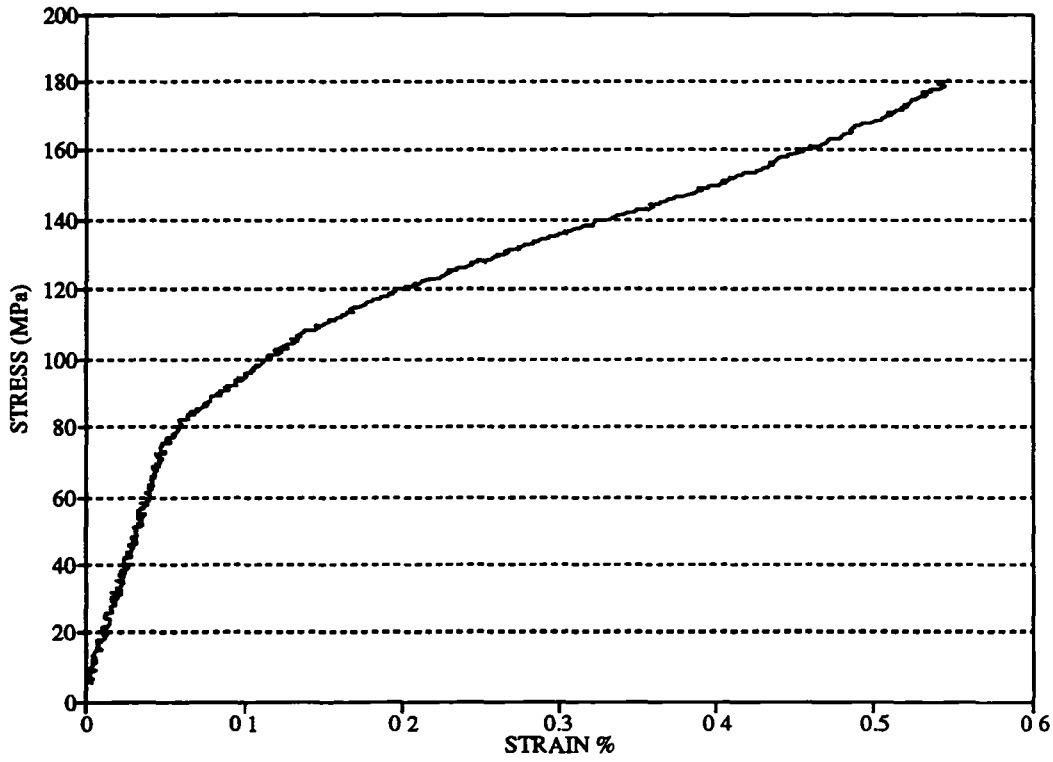

Figure 20. Stress vs strain for sample C5 (SiC/CAS, $[0/90]_{4s}$)

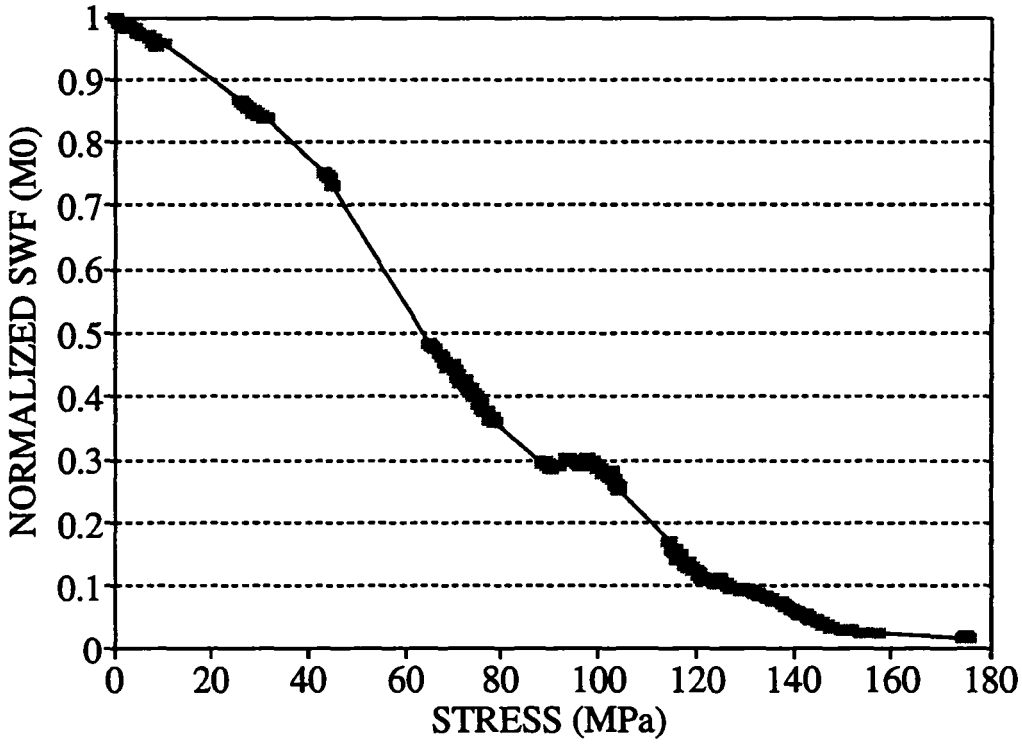

Figure 21. Normalized SWF (M0) vs stress for sample C2 (SiC/CAS, $[0/90]_{4s}$)

normalized SWF values versus stress levels. The monotonic decrease in SWF values with increasing stress levels till 85 MPa is due to the matrix cracking in the 90^0 plies. The recorded in-situ SWF values remain fairly constant over a narrow stress range at the knee till 100 MPa, followed by a second decrease in their values. This latter decrease is attributed to the matrix cracking in the 0^0 plies followed by the saturation of matrix cracks at 150 MPa in all plies and the final failure of the specimen. Significant fiber pull-out is observed in both samples C5 and C2.

Similar tests were performed on samples C6 and C7. Figures 22 and 24 show the normalized SWF (M0) values versus stress levels for samples C6 and C7, respectively. The saturation of matrix cracking in all plies in both samples takes place at approximately 150 MPa as indicated by the flat portions of the SWF graphs prior to failure. Figure 23 shows the graph of stress versus strain for sample C6. A typical strain response of a cross-ply laminate under static loads has two non-linear portions corresponding to 90^0 and 0^0 plies. The slope of the first linear portion is given by E_{xx} obtained from classical laminated plate theory followed by the first nonlinear zone caused by matrix cracking in the 90^0 plies followed by the second nonlinear zone caused by matrix cracking in the 0^0 plies. The strain at the saturation of matrix cracking is about 0.55% in both samples. The load is being carried by the fibers at this juncture and hence a second linear portion of the curve is seen till failure. Normalized SWF values show a local increase at the start of the test of sample C6 that may have been caused by erroneous instrumentation signals generated at that time. Significant fiber pull-out is observed at the failed surface as shown in Fig. 25. Figure 26 shows the interfacial failure of the fiber matrix system as cracks bifurcate and propagate around the fiber due to the weak bonding.

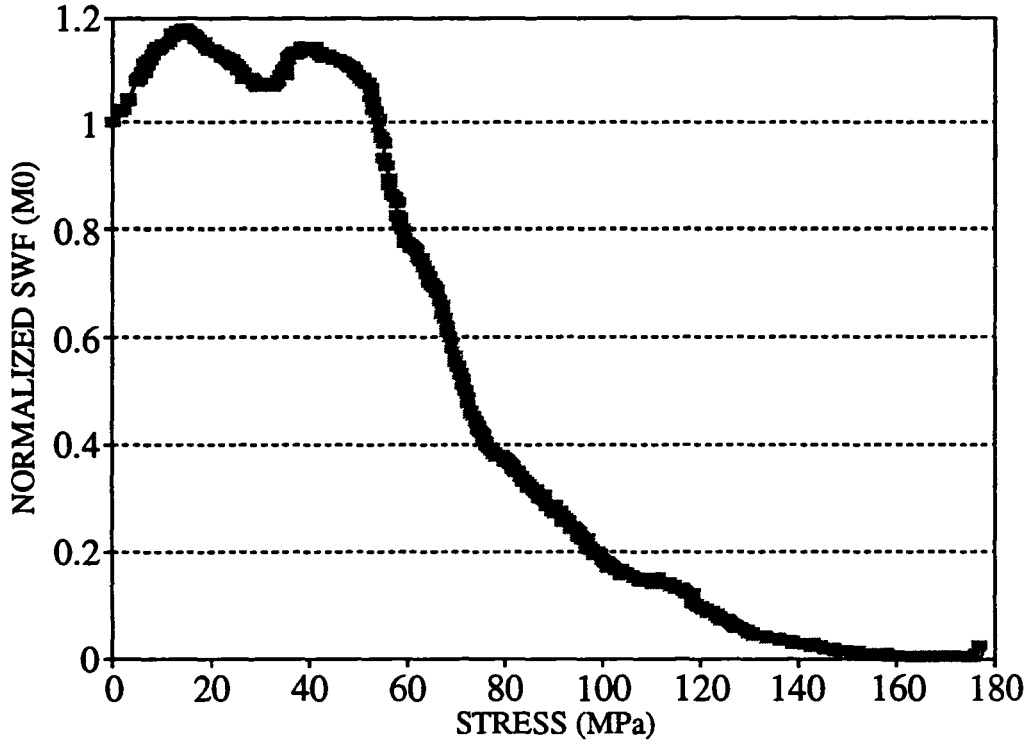

Figure 22. Normalized SWF (M0) vs stress for sample C6 (SiC/CAS, $[0/90]_{4s}$)

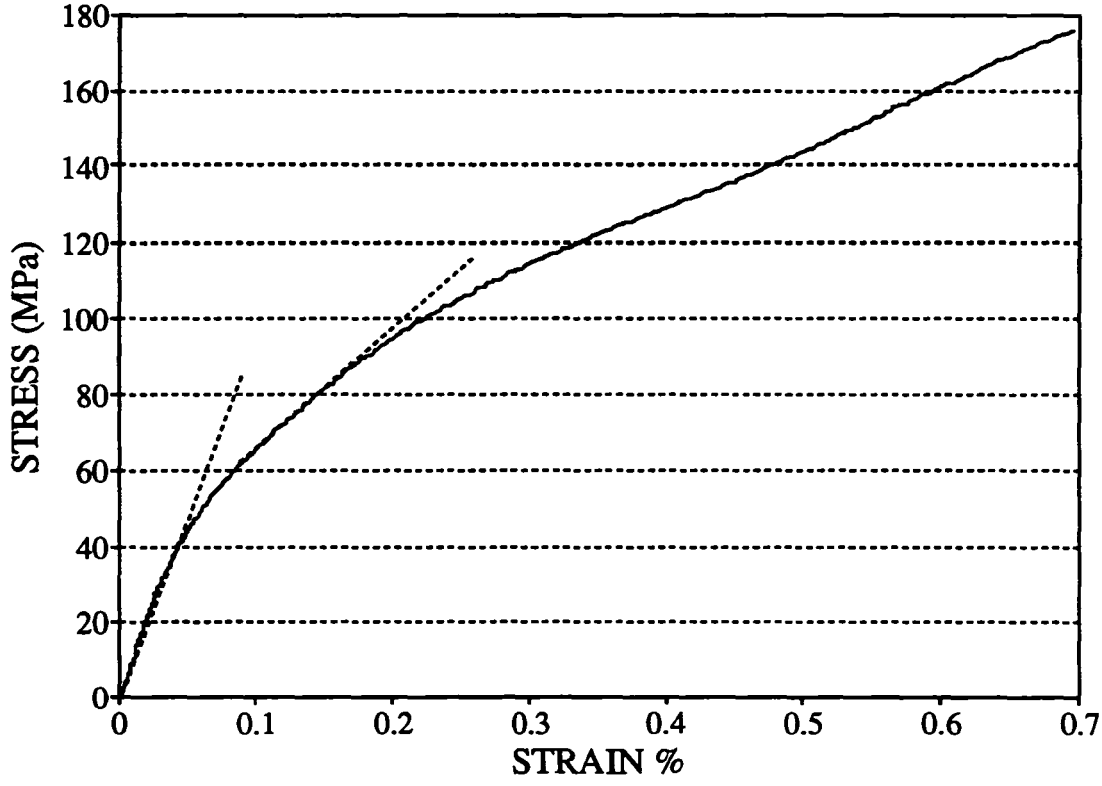

Figure 23. Stress vs strain for sample C6 (SiC/CAS, $[0/90]_{4s}$)

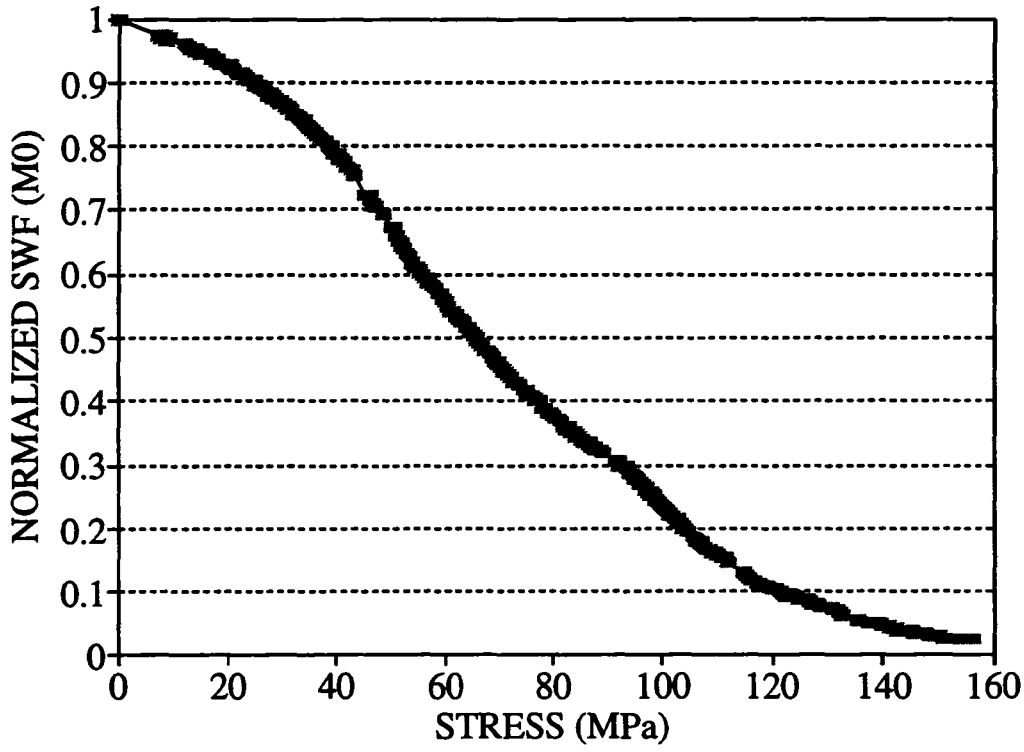

Figure 24. Normalized SWF (M0) vs stress for sample C7 (SiC/CAS, $[0/90]_{4s}$)

(a)

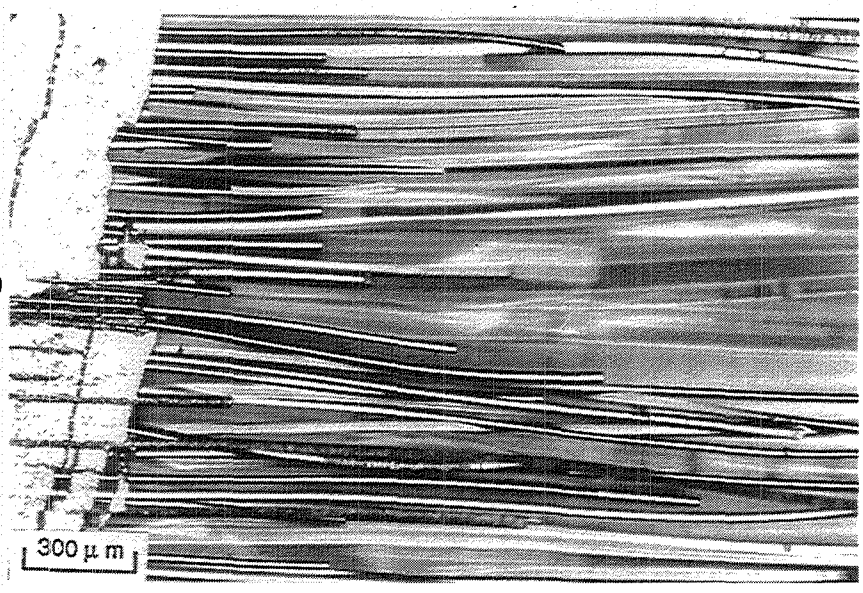

(b)

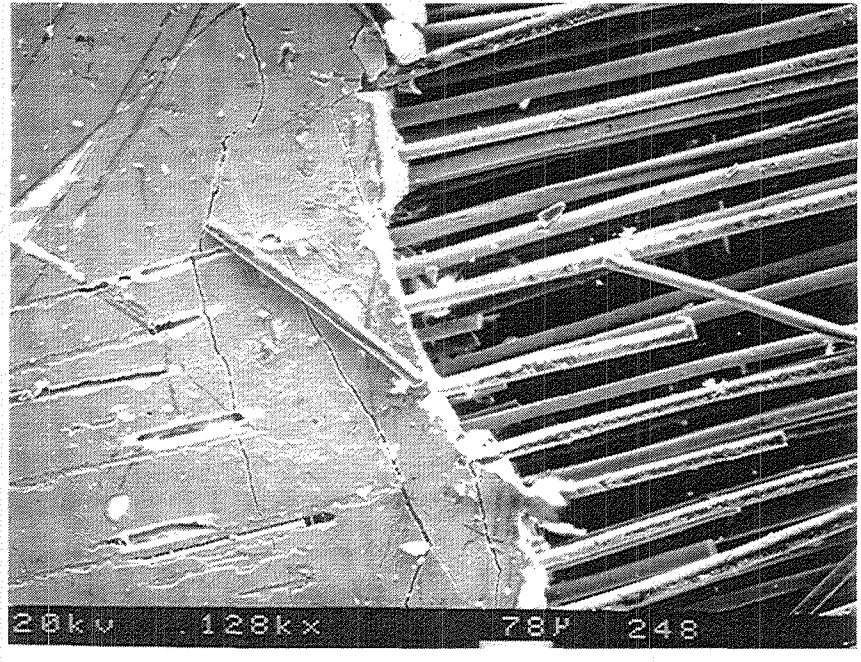

Figure 25. (a) Photo-micrograph of the failure surface of sample C6 (SiC/CAS, $[0/90]_{4s}$), (b) an enlarged view

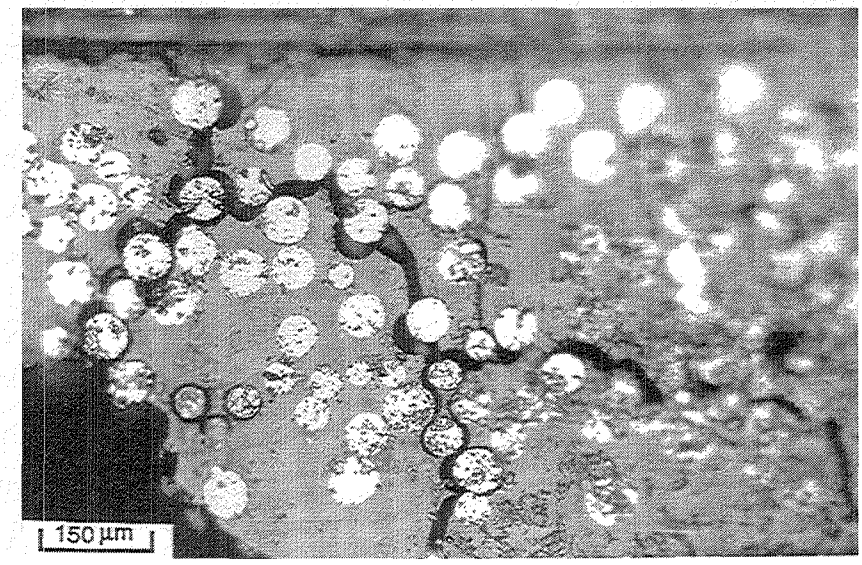

Figure 26. Photo-micrograph showing interfacial debond at failure for sample C6 (SiC/CAS, $[0/90]_{4s}$)

4.4.1 Heat treated cross-ply $[0/90]_{4s}$ SiC/CAS static tests

Samples C8 and C9 were heat treated at 1200^0 C for 48 hours prior to static tests. Both samples were subjected to quasi-static ramp loading in tension to failure at 200 lbs/min. Figures 27 and 29 show the graphs of SWF (M0) versus stress for samples C8 and C9, respectively. Final failure is catastrophic in both samples with negligible fiber pull-out observed on the failure surfaces. Figure 28 shows the stress versus strain graph of sample C8. The failure strain and ultimate strength were 0.1 %, 55 MPa and 0.14 %, 70 MPa in samples C8 and C9, respectively. The stress levels for final failure of heat treated specimens are in the range of the stress levels for cracking in the 90^0 plies of non heat treated specimens. It is presumed that the interfacial bonding is stronger due to the heat treatment and the few cracks formed in the 90^0 plies connect and cause final failure by breaking the fibers in their path instead of debonding them. The SWF values drop by 45 % in the range of 50 MPa - 70 MPa in sample C9 whereas the drop is just 10 % prior to catastrophic failure in sample C8. Real-time AU gives no indication of impending final failure in sample C8. The close proximity of flaws in this specimen which serve as crack initiation sites could cause the cracks to become critical and thereby cause premature failure.

Figure 30 (a) shows a polished surface of sample C9 used as a target for long distance optical microscope to monitor surface damage. Figure 30 (b) shows a clean fiber from the failed surface of sample C9 with very little matrix material attached to it. Figure 31 (a) and (b) are SEM photographs showing the difference in failure surface between the free edges and the mid region of the laminate of

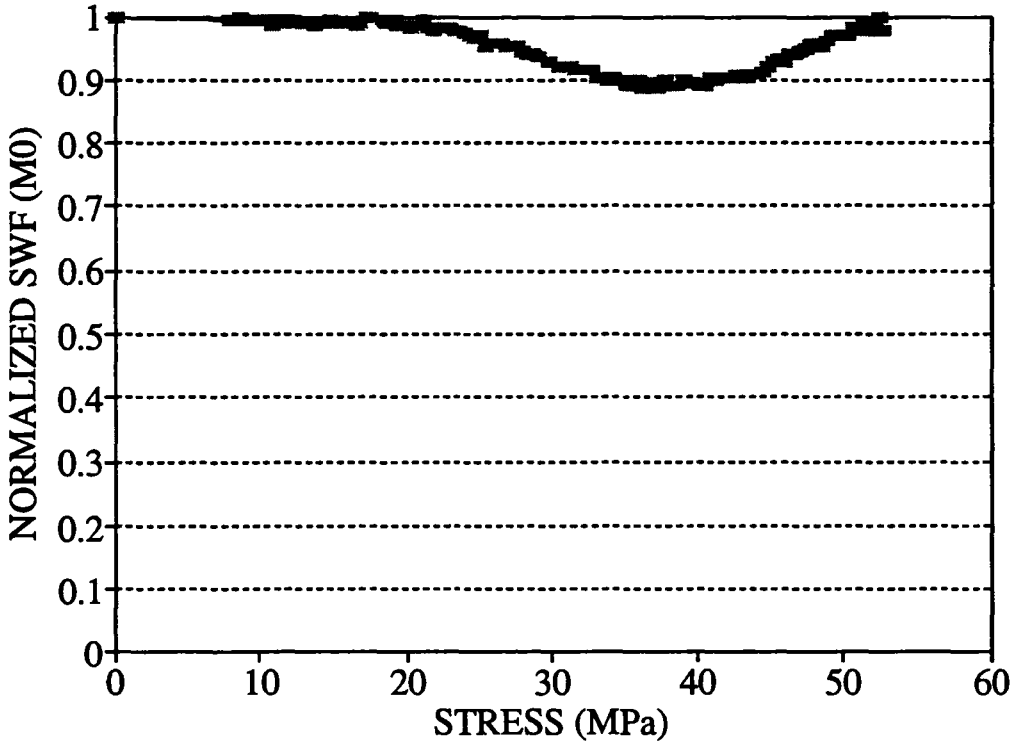

Figure 27. Normalized SWF (M0) vs stress for sample C8 (SiC/CAS, $[0/90]_{4s}$), (Heat treated at 1200°C for 48 hrs.)

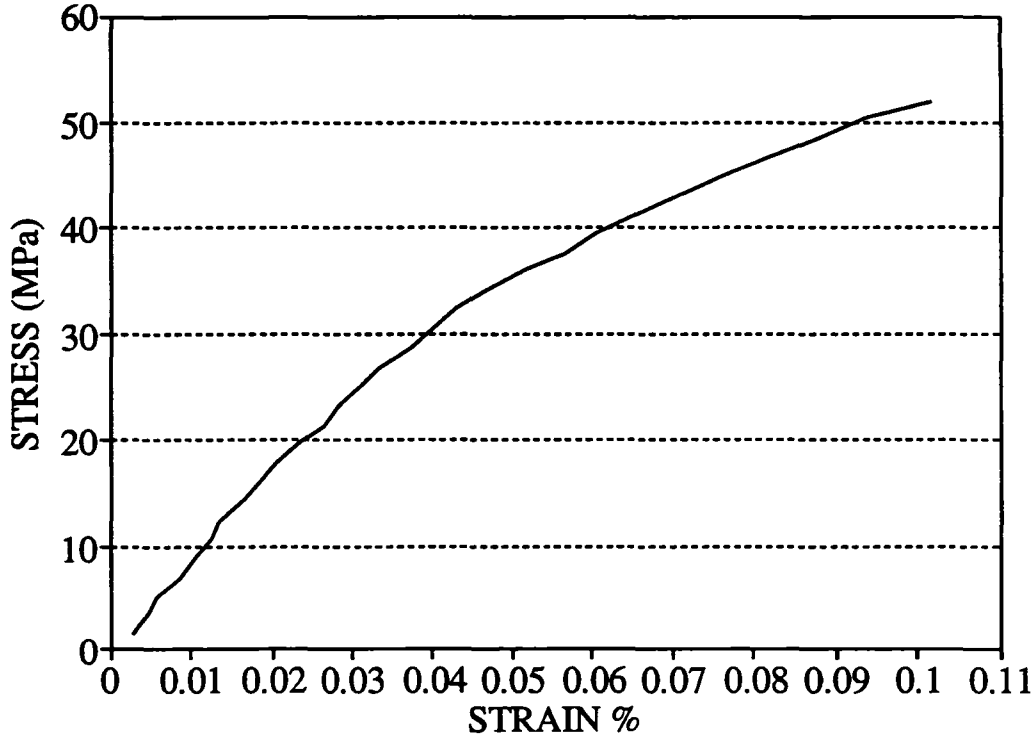

Figure 28. Stress vs strain for sample C8 (SiC/CAS, $[0/90]_{4s}$)
(Heat treated at 1200°C for 48 hrs.)

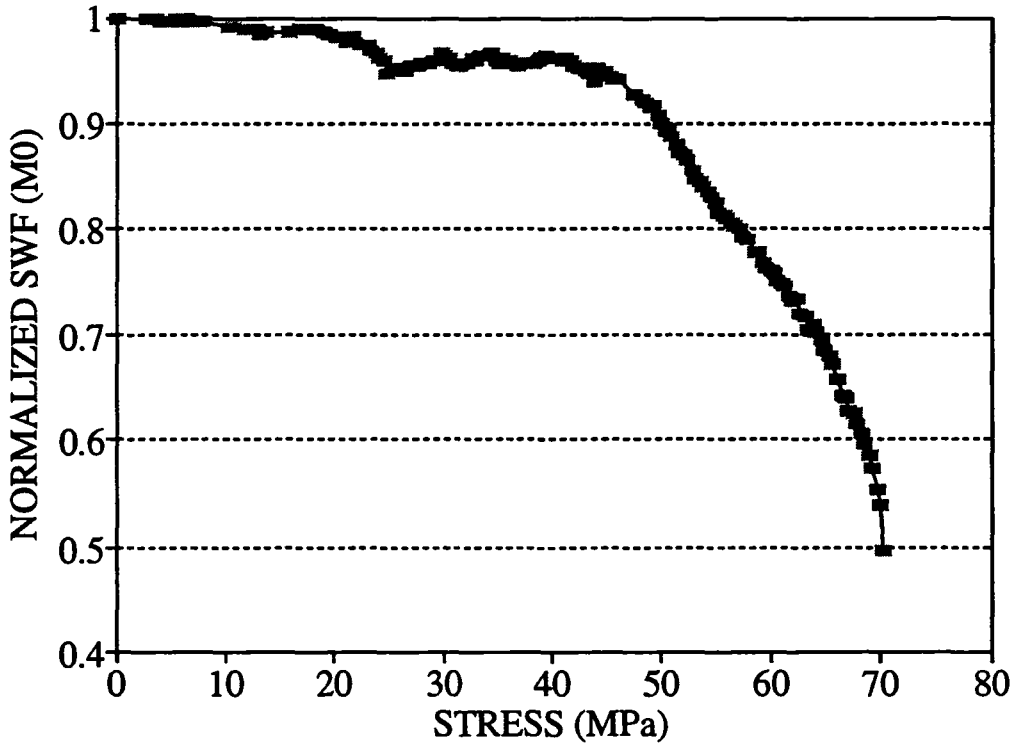

Figure 29. Normalized SWF (M0) vs stress for sample C9 (SiC/CAS, $[0/90]_{4s}$), (Heat treated at 1200°C for 48 hrs.)

(a)

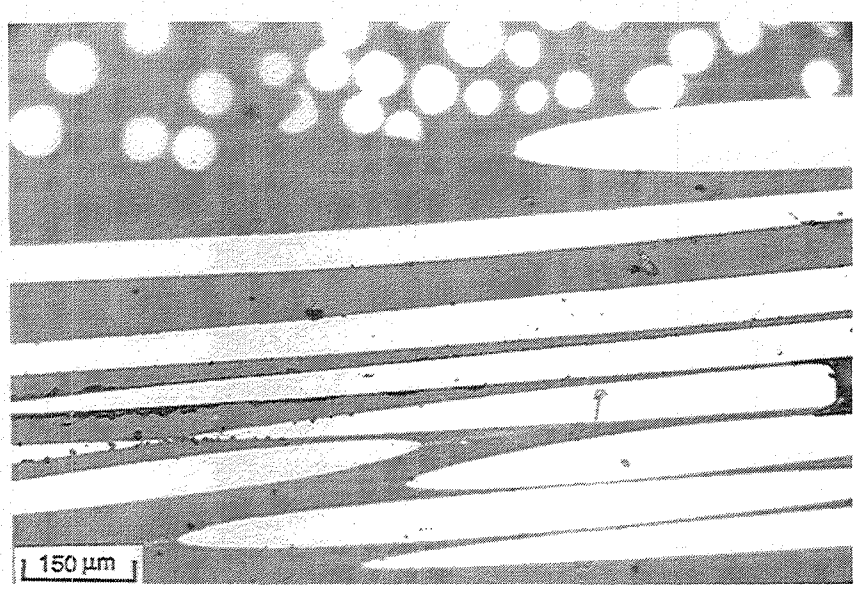

(b)

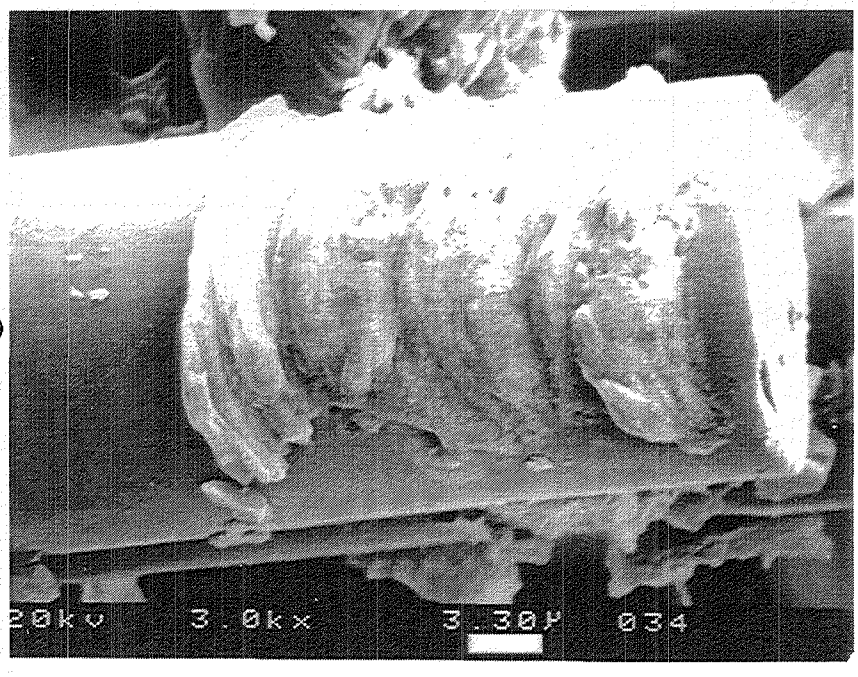

Figure 30. (a) Polished surface of heat treated sample C9 (SiC/CAS, $[0/90]_{4s}$) (b) SEM photo-micrograph of a fiber located at the mid-region of the laminate at failure (sample C9).

(a)

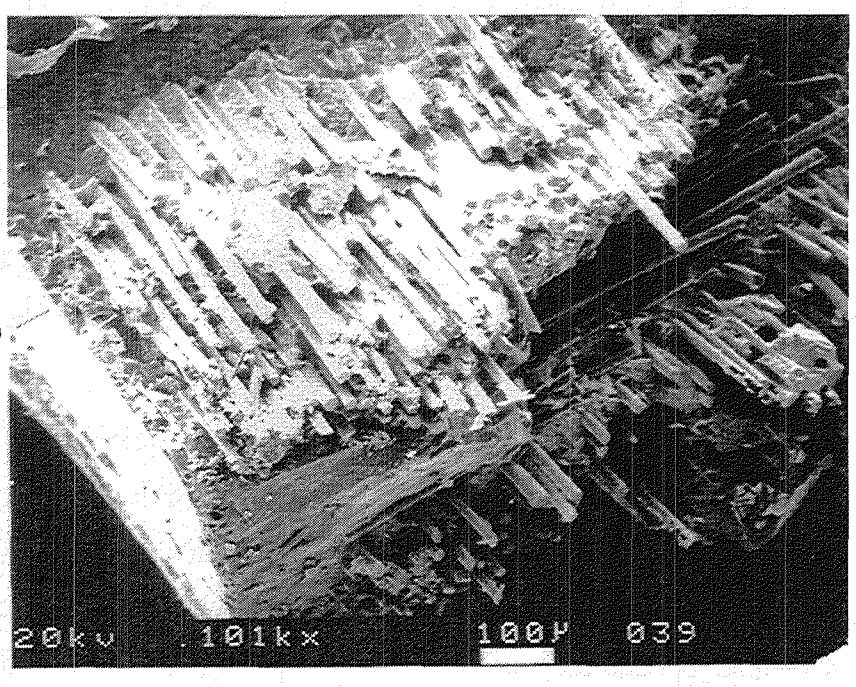

(b)

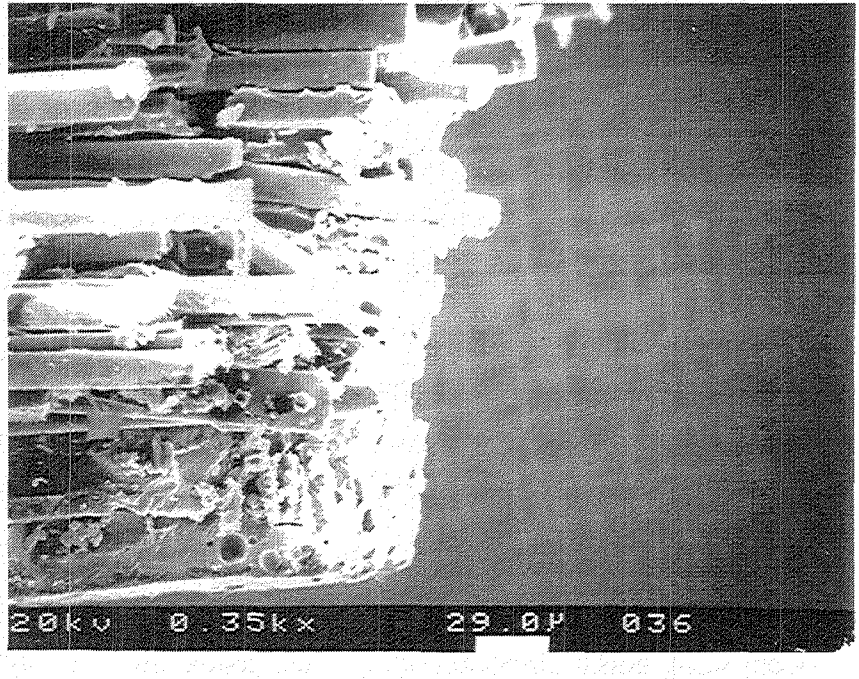

Figure 31. (a) SEM photo-micrograph of the failure surface of heat treated sample C9 (SiC/CAS, $[0/90]_{4s}$) (b) Enlarged view showing non-uniform heat treatment.

sample C9. The oxygen has diffused to about 100μm from the free surface only and hence we see clean fiber breaks close to the edges and fiber pull-out at other regions. The number of hours for heat treatment was found to be insufficient.

4.5 Failure Process of cross-ply $[0/90]_{4s}$ SiC/CAS under static loads

The failure process in a cross-ply ceramic laminate subjected to static loads consists of degradation of the 90^0 plies caused by matrix cracking in those plies, followed by the onset and saturation of matrix cracking in the 0^0 plies. At this juncture, all the load is being shared by the fibers. Interface debonding and a small number of fiber breaks also occur followed by large scale fiber breaks and fiber pull-out just prior and during final failure.

The slope of the initial linear portion of the stress strain curve is given by E_{xx} obtained from classical laminated plate theory. The start of nonlinearity in the stress strain curve caused by matrix cracking in the 90^0 plies varies from specimen to specimen and is dependent on the flaw population and distribution. The onset of matrix cracking in the 0^0 plies occurs at approximately 90 MPa - 100 MPa. The saturation of matrix cracks has occurred by 150 MPa for all cross-ply specimens tested, independently of any flaw distribution or processing parameter. The second linear portion of the stress strain curve starts at this stress level as all the load is being carried by the fibers past this point. The upper bound for the slope of the second linear portion is given by $\nu_f E_f$. This is an upper bound as some limited fiber breaks occur early and their contribution to the global strain is unaccounted. After the degradation of the 90^0 plies, all the load is being carried by the eight 0^0 plies

and hence the effective stress for onset and saturation of cracking in the remaining 0^0 plies (190 MPa and 300 MPa respectively) is the same as those observed in unidirectional material. The ultimate tensile strength of a cross-ply laminate with eight 0^0 plies is numerically half of the tensile strength of a 16-ply unidirectional specimen. The ultimate strength of the cross-ply laminate is dependent on the strength of the 0^0 plies which are the critical elements in the failure process [93,94]. The effective strength per critical ply is the same, and is consistent with, the unidirectional strength. Hence, the failure process in a cross-ply laminate is very similar to that in a unidirectional laminate apart from the initial degradation of the 90^0 plies caused by matrix cracking in those plies.

The failure in heat treated specimens is brittle in nature and is caused by cracks in the 90^0 plies which connect and result in brittle failure. The interface has a strong bond caused by oxygen ingression at the interface. The fibers in the path of propagating cracks break and hence there is no fiber bridging mechanism. The strain at failure is 20 % lower (0.12%) compared to non-heat treated specimens and the ultimate strength is reduced by 50-60% due to the heat treatment.

4.6 Quasi-isotropic $[0/\pm45/90]_{2s}$ SiC/MAS static tests

Samples MAS-8, MAS-11, MAS-1, MAS-3 and MAS-10 are 16-ply quasi-isotropic $[0/\pm45/90]_{2s}$ laminates of SiC/MAS. Samples MAS-1, MAS-3 and MAS-10 were subjected to heat treatment for 100 hours at 1100^0 C. The specimens were ramp loaded in tension to failure and AU parameters were monitored in real-time. Figure 32 shows the graph of SWF (M0) versus stress of sample MAS-8. The SWF values decrease in atleast four distinct regions (0-75 MPa, 75-125 MPa, 125-180 MPa and 180 MPa to failure). The stress/strain graph shown in Fig. 33 is bi-

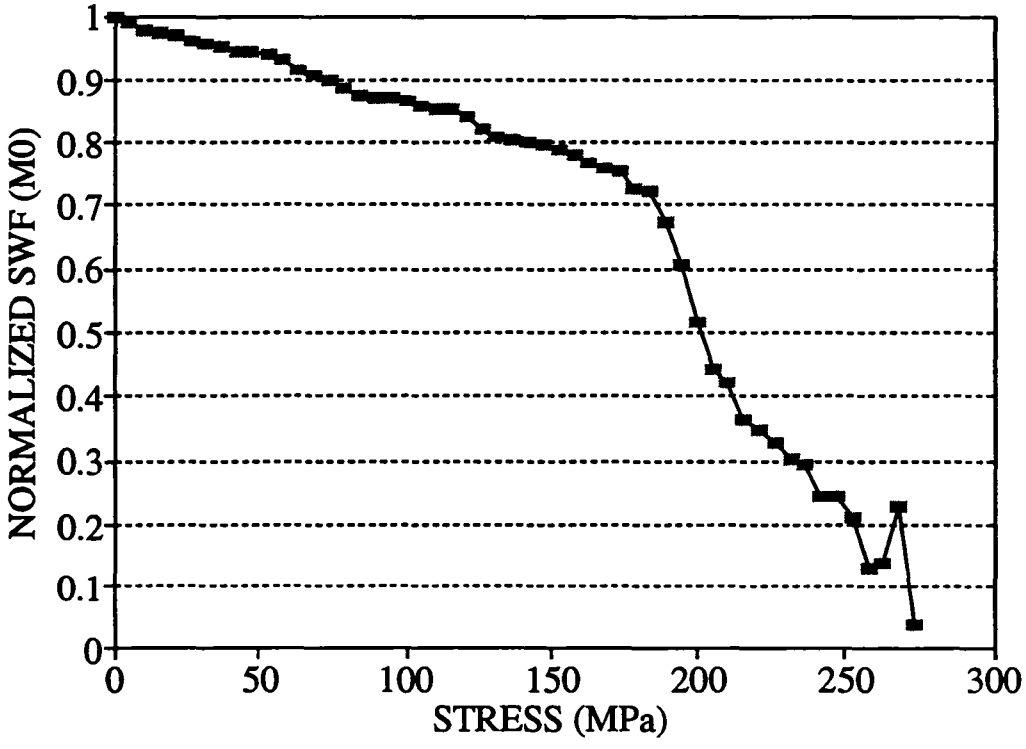

Figure 32. Normalized SWF (M0) vs stress for sample MAS-8
(SiC/MAS, $[0/\pm45/90]_{2s}$)

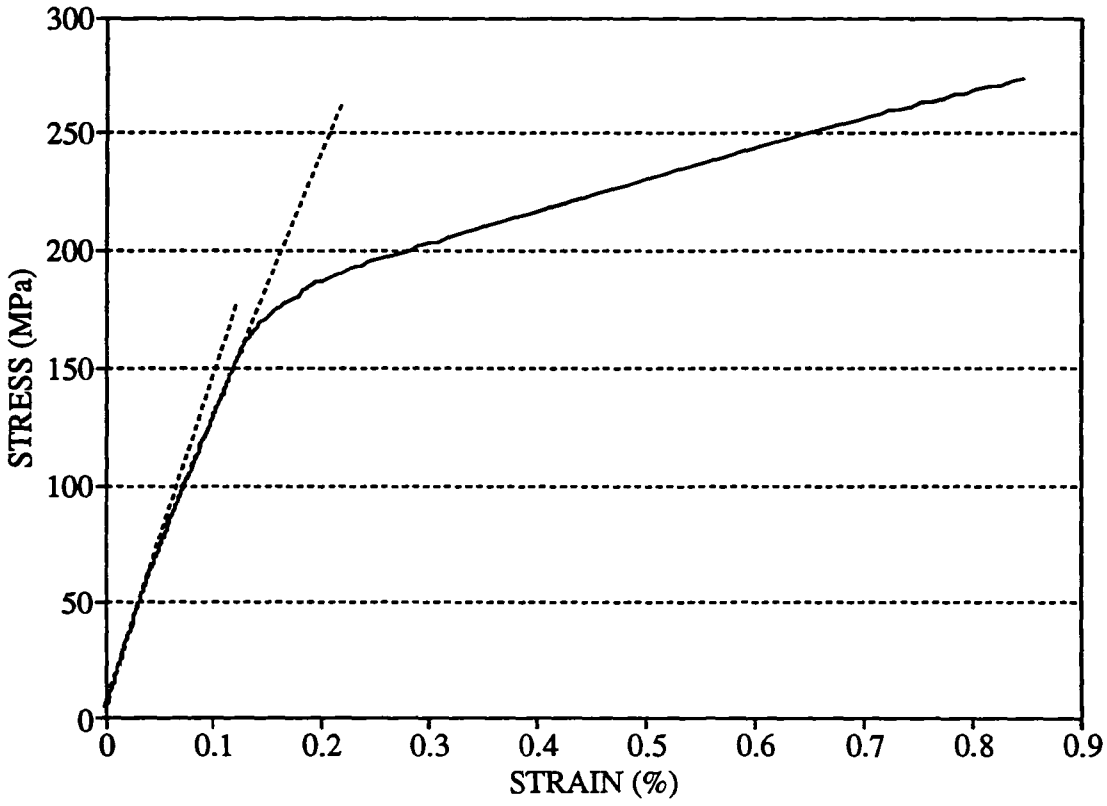

Figure 33. Stress vs strain for sample MAS-8 (SiC/MAS, $[0/\pm45/90]_{2s}$)

linear initially in the stress range of 0-170 MPa, with the intersection point between the linear ranges being at 65 MPa. It is presumed that matrix cracking in the 90^0 and $\pm 45^0$ plies occurs successively in the ranges of 75-125 MPa and 125-180 MPa. The initial decrease of SWF and the deviation from linear behavior of stress/strain graph is due to the distribution of flaws and their close proximity to each other which causes several cracks to develop at low loads. The sharp drop in SWF values occurs at 180 MPa and is attributed to matrix cracking in the 0^0 plies. The majority of the load is being carried by the 0^0 plies at this juncture. There is an increase in AE activity caused by fiber breaks prior to final failure at 270 MPa as indicated by the increase in SWF in this range. The failure strain was 0.85% for sample MAS-8 as shown in Fig. 33. The stress levels at which matrix cracks occur in different plies is based on real-time AU data. Damage occurrence on the surface of each plies was not recorded on a video and hence this is a speculation supported by AU data only.

A similar test was performed on sample MAS-11. The SWF values drop by 15 % in the range of 125-175 MPa as shown in Fig. 34, followed by a 70 % drop in SWF values in the range of 175 MPa to failure caused by matrix cracking in the 0^0 plies. The failure occurred at 260 MPa with a failure strain of 0.88 %. There is a slight initial drop in SWF values and the laminate had a bi-linear behavior as observed in the stress/strain graph.

4.6.1 Heat treated Quasi-isotropic $[0/\pm 45/90]_{2s}$ SiC/MAS static tests

Samples MAS-1, MAS-3 and MAS-10 were subjected to heat treatment prior to mechanical loading. Figure 35 shows the graph of SWF (M0) value versus

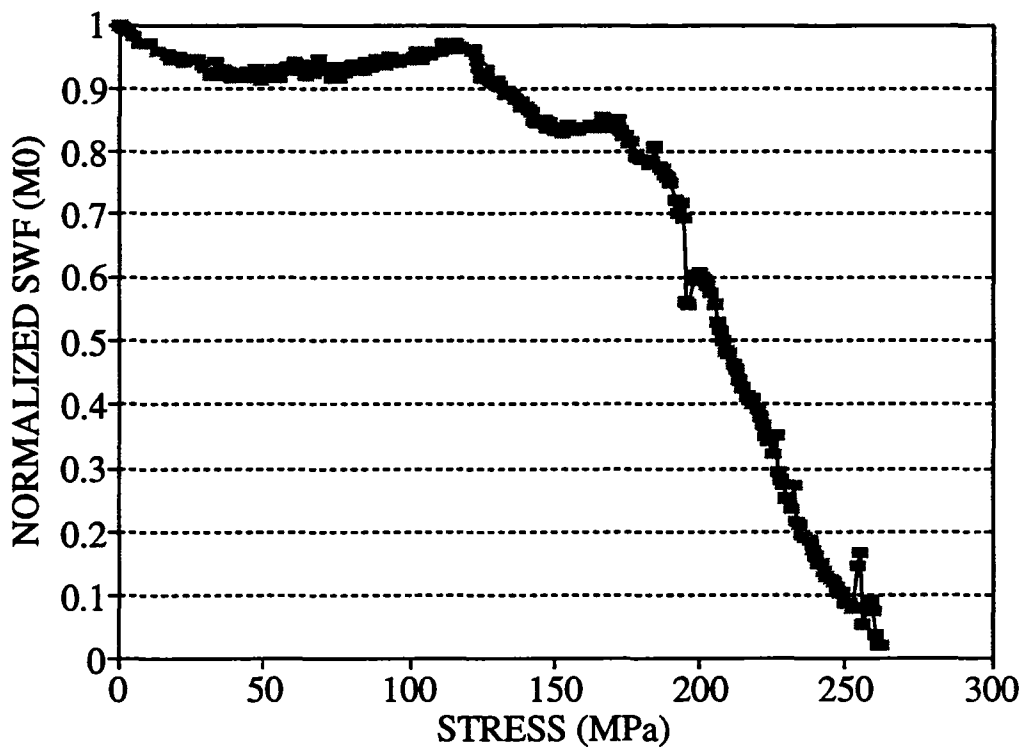

Figure 34. Normalized SWF (M0) vs stress for sample MAS-11 (SiC/MAS, $[0/\pm45/90]_{2s}$)

Figure 35. Normalized SWF (M0) vs stress for sample MAS-1
(SiC/MAS, $[0/\pm45/90]_{2s}$)

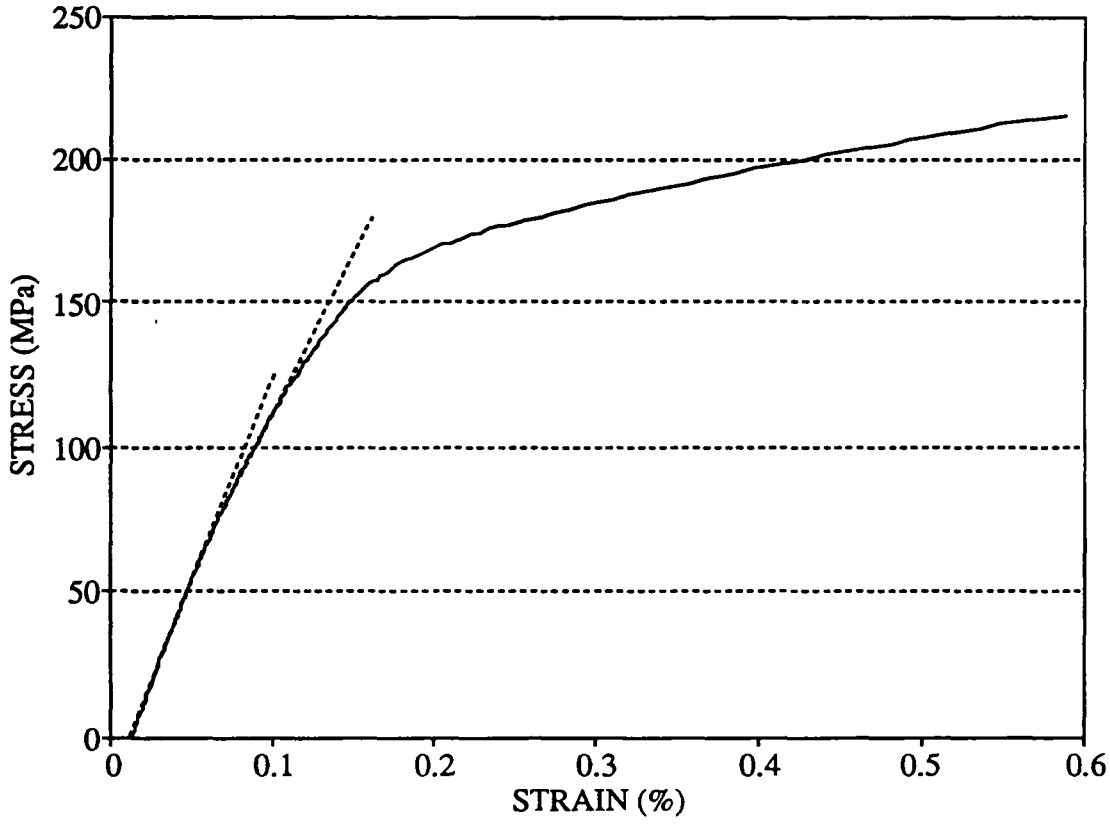

Figure 36. Stress vs strain for sample MAS-1 (SiC/MAS, $[0/\pm45/90]_{2s}$)

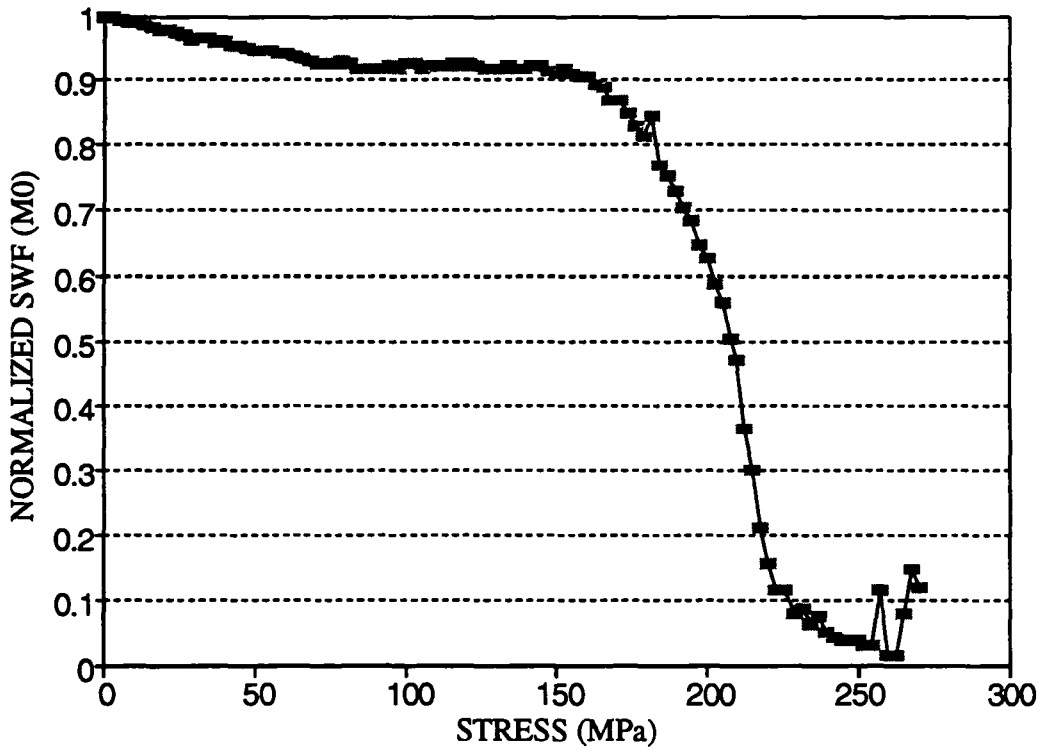

Figure 37. Normalized SWF (M0) vs stress for sample MAS-3
(SiC/MAS, $[0/\pm45/90]_{2s}$)

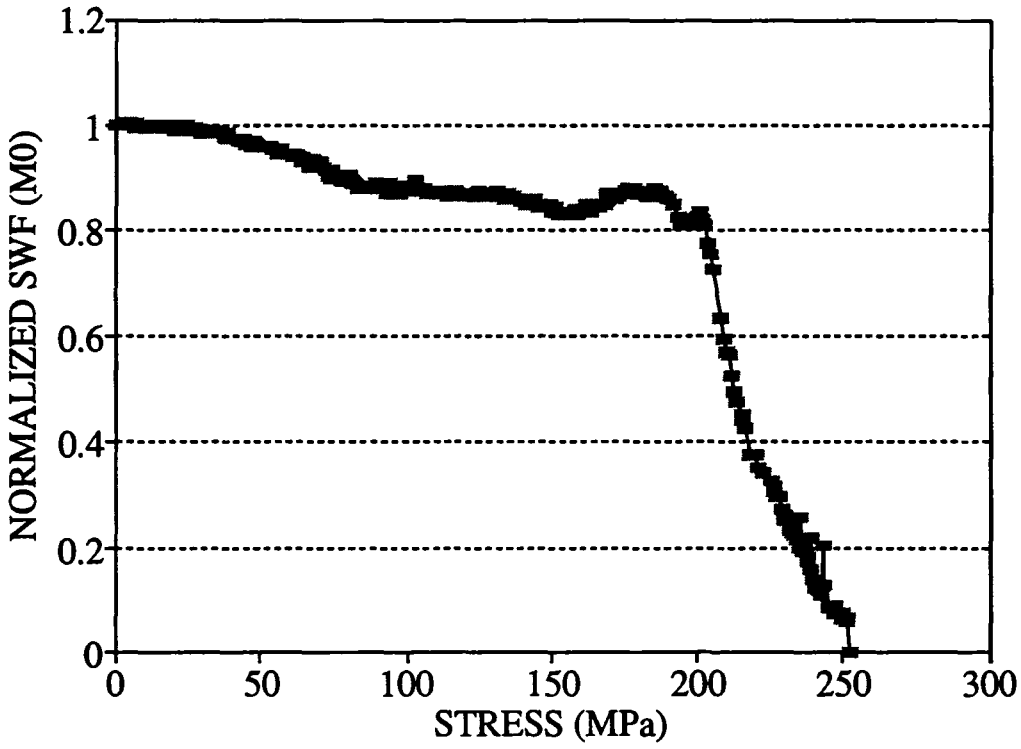

Figure 38. Normalized SWF (M0) vs stress for sample MAS-10
(SiC/MAS, $[0/\pm45/90]_{2s}$)

stress of sample MAS-1. The SWF values start decreasing from very low loads till 60 MPa (20% decrease) followed by another, slower decrease (12%) at 130 MPa. The final rapid drop in SWF values occurs from 130 MPa till final failure (60% decrease). The failure stress is 220 MPa and the corresponding failure strain is 0.58% as shown in Fig. 36. A bi-linear curve is seen in the initial portion of the stress/strain curve in the range of 0-130 MPa with the intersection point between the two linear regions being 65 MPa.

Similar static tests were run on samples MAS-3 and MAS-10. Figures 37 and 38 show the graphs of SWF (M0) versus stress which follows the same trend as that of sample MAS-1. Matrix cracking takes place in the off-axis plies prior to the start of matrix cracking in the 0^0 plies which causes the last sharp drop in SWF values. Further investigation and documentation of the surface damage during testing needs to be done as these conclusions are based on AU data only. The final failure in heat treated specimens was brittle in nature.

5. AUSSR MODEL

5.1 Introduction

The nonlinear behavior observed in a stress-strain curve for a unidirectional ceramic composite is predominantly attributed to the effect of matrix cracks. The onset of matrix cracks and the first matrix cracks observed by a long distance optical microscope occur at the same stress level as described in the previous chapter. The models presented in this chapter are an attempt to describe the damage mechanisms occurring by incorporating the effect of matrix cracks and fiber breakage on the global strain response of the laminate to increasing loads. Section 5.1 presents the fundamentals of classical laminated plate theory and the procedure for calculating strains at the outer surface of the laminate for a given load. The strains at the outer surface obtained from the models described in this chapter can be compared to the experimentally observed strains from the extensometer attached to the outer surface. Different models will be introduced in this chapter outlining the history of development of successive models as the research progressed. The acousto-ultrasonic stress-strain response (AUSSR) model introduced in this chapter is capable of predicting the strain response to increasing stress levels for unidirectional and cross-ply ceramic composite laminates. The fundamentals of classical laminated plate theory is presented as follows:

Hooke's law for an elastic material is given by

$$\sigma_{ij} = C_{ijkl}\,\varepsilon_{kl} \tag{5.1}$$

where σ_{ij} and ε_{ij} are the stress and strain components, respectively, and C_{ijkl} are the elastic stiffness coefficients. The inverse of Equation (1.1) is given by

$$\varepsilon_{ij} = S_{ijkl}\,\sigma_{kl} \tag{5.2}$$

where S_{ijkl} are the elastic compliance coefficients. It is convenient to introduce the following contracted notation to represent C_{ijkl} and S_{ijkl} in compact form:

$$\begin{array}{ccc} 11\rightarrow 1 & 22\rightarrow 2 & 33\rightarrow 3 \\ 23=32\rightarrow 4 & 13=31\rightarrow 5 & 12=21\rightarrow 6 \end{array} \tag{5.3}$$

The stress-strain relationship in a co-ordinate system aligned with principal material directions for an orthotropic material (9 independent constants) is:

$$\begin{pmatrix} \sigma_{11} \\ \sigma_{22} \\ \sigma_{33} \\ \sigma_{23} \\ \sigma_{13} \\ \sigma_{12} \end{pmatrix} = \begin{bmatrix} C_{11} & C_{12} & C_{13} & 0 & 0 & 0 \\ C_{12} & C_{22} & C_{23} & 0 & 0 & 0 \\ C_{13} & C_{23} & C_{33} & 0 & 0 & 0 \\ 0 & 0 & 0 & C_{44} & 0 & 0 \\ 0 & 0 & 0 & 0 & C_{55} & 0 \\ 0 & 0 & 0 & 0 & 0 & C_{66} \end{bmatrix} \begin{pmatrix} \varepsilon_{11} \\ \varepsilon_{22} \\ \varepsilon_{33} \\ 2\varepsilon_{23} \\ 2\varepsilon_{13} \\ 2\varepsilon_{12} \end{pmatrix} \tag{5.4}$$

For a lamina in the 1-2 plane, a plane stress state is defined by setting $\sigma_3 = \tau_{23} = \tau_{13} = 0$. For an orthotropic material under a plane stress state, this results in $\varepsilon_3 = S_{13}\sigma_1 + S_{23}\sigma_2$ and $\gamma_{23} = \gamma_{13} = 0$. The stress-strain relationships in principal

material co-ordinates for a lamina of an orthotropic material under plane stress is thus reduced to:

$$\begin{pmatrix} \sigma_1 \\ \sigma_2 \\ \sigma_{12} \end{pmatrix} = \begin{bmatrix} Q_{11} & Q_{12} & 0 \\ Q_{12} & Q_{22} & 0 \\ 0 & 0 & Q_{66} \end{bmatrix} \begin{pmatrix} \varepsilon_1 \\ \varepsilon_2 \\ 2\varepsilon_{12} \end{pmatrix} \tag{5.5}$$

Q_{ij} is the reduced stiffness matrix and can be expressed in terms of engineering elastic constants as follows:

$$\begin{aligned} Q_{11} &= \frac{E_1}{1-\nu_{12}\nu_{21}} \\ Q_{12} &= \frac{\nu_{12}E_2}{1-\nu_{12}\nu_{21}} = \frac{\nu_{21}E_1}{1-\nu_{12}\nu_{21}} \\ Q_{22} &= \frac{E_2}{1-\nu_{12}\nu_{21}} \\ Q_{66} &= G_{12} \end{aligned} \tag{5.6}$$

The stress in any other co-ordinate system in the plane of the lamina is given by:

$$\begin{pmatrix} \sigma_x \\ \sigma_y \\ \sigma_{xy} \end{pmatrix} = \begin{bmatrix} \bar{Q}_{11} & \bar{Q}_{12} & \bar{Q}_{16} \\ \bar{Q}_{12} & \bar{Q}_{22} & \bar{Q}_{26} \\ \bar{Q}_{16} & \bar{Q}_{26} & \bar{Q}_{66} \end{bmatrix} \begin{pmatrix} \varepsilon_x \\ \varepsilon_y \\ 2\varepsilon_{xy} \end{pmatrix} \tag{5.7}$$

$\bar{Q}_{ij}$ is the reduced stiffness matrix for an arbitrary orientation. Alternatively, the stress strain relationship can be written for the K th layer with arbitrary orientation as:

$$(\sigma)_k = [\,\bar{Q}\,]_k\,(\varepsilon)_k \tag{5.8}$$

Kirchoff's hypotheses for plates assumes that laminates consist of perfectly bonded laminae with bonds being extremely thin and non-shear deformable. The displacements are continuous across lamina boundaries and there is no relative slip between lamina. Normals to the middle surface remain straight and normal under deformations ($\gamma_{xz} = \gamma_{yz} = 0$). And, finally, the strains perpendicular to the middle surface is negligible ($\varepsilon_z = 0$).

The implications of these assumptions on the laminate displacements u, v, w, in the x, y, z direction results in the following:

$$\begin{pmatrix} \varepsilon_x \\ \varepsilon_y \\ 2\varepsilon_{xy} \end{pmatrix} = \begin{pmatrix} \varepsilon_x^o \\ \varepsilon_y^o \\ 2\varepsilon_{xy}^o \end{pmatrix} + Z \begin{pmatrix} K_x \\ K_y \\ K_{xy} \end{pmatrix} \tag{5.9}$$

where,

$$\begin{pmatrix} \varepsilon_x^o \\ \varepsilon_y^o \\ 2\varepsilon_{xy}^o \end{pmatrix} = \begin{pmatrix} \dfrac{\partial u_o}{\partial x} \\ \dfrac{\partial v_o}{\partial y} \\ \dfrac{\partial u_o}{\partial y} + \dfrac{\partial v_o}{\partial x} \end{pmatrix} \tag{5.10}$$

are the middle surface strains and

$$\begin{pmatrix} K_x \\ K_y \\ K_{xy} \end{pmatrix} = - \begin{pmatrix} \dfrac{\partial^2 w_o}{\partial x^2} \\ \dfrac{\partial^2 w_o}{\partial y^2} \\ \dfrac{2\partial^2 w_o}{\partial x \partial y} \end{pmatrix} \tag{5.11}$$

are the middle surface curvatures. The superscript 'o' denotes middle surface values.The stresses in the Kth layer are then expressed in terms of the laminate middle surface strains and curvatures as:

$$\begin{pmatrix} \sigma_x \\ \sigma_y \\ \sigma_{xy} \end{pmatrix}_k = \begin{bmatrix} \bar{Q}_{11} & \bar{Q}_{12} & \bar{Q}_{16} \\ \bar{Q}_{12} & \bar{Q}_{22} & \bar{Q}_{26} \\ \bar{Q}_{16} & \bar{Q}_{26} & \bar{Q}_{66} \end{bmatrix}_k \left\{ \begin{pmatrix} \varepsilon_x^o \\ \varepsilon_y^o \\ 2\varepsilon_{xy}^o \end{pmatrix} + Z \begin{pmatrix} K_x \\ K_y \\ K_{xy} \end{pmatrix} \right\} \tag{5.12}$$

The resultant forces and moments for an N layered laminate are obtained by integrating the stresses in each lamina through the laminate thickness (2H).

$$\begin{pmatrix} N_x \\ N_y \\ N_{xy} \end{pmatrix} = \int_{-H}^{H} \begin{pmatrix} \sigma_x \\ \sigma_y \\ \sigma_{xy} \end{pmatrix}_k dz = \sum_{K=1}^{N} \int_{Z_{K-1}}^{Z_K} \begin{pmatrix} \sigma_x \\ \sigma_y \\ \sigma_{xy} \end{pmatrix}_k dz \tag{5.13}$$

and

$$\begin{pmatrix} M_x \\ M_y \\ M_{xy} \end{pmatrix} = \int_{-H}^{H} \begin{pmatrix} \sigma_x \\ \sigma_y \\ \sigma_{xy} \end{pmatrix}_k z\, dz = \sum_{K=1}^{N} \int_{Z_{K-1}}^{Z_K} \begin{pmatrix} \sigma_x \\ \sigma_y \\ \sigma_{xy} \end{pmatrix}_k z\, dz \tag{5.14}$$

where z_K and z_{K-1} are the distance in the z direction from the mid-plane of the laminate to the outer and inner boundary of the K th lamina, respectively. Substitution of the stresses from equation 5.12 gives

$$\begin{pmatrix} N_x \\ N_y \\ N_{xy} \\ M_x \\ M_y \\ M_{xy} \end{pmatrix} = \begin{bmatrix} A_{11} & A_{12} & A_{16} & B_{11} & B_{12} & B_{16} \\ A_{12} & A_{22} & A_{26} & B_{12} & B_{22} & B_{26} \\ A_{16} & A_{26} & A_{66} & B_{16} & B_{26} & B_{66} \\ B_{11} & B_{12} & B_{16} & D_{11} & D_{12} & D_{16} \\ B_{12} & B_{22} & B_{26} & D_{12} & D_{22} & D_{26} \\ B_{16} & B_{26} & B_{66} & D_{16} & D_{26} & D_{66} \end{bmatrix} \begin{pmatrix} \varepsilon_x^o \\ \varepsilon_y^o \\ 2\varepsilon_{xy}^o \\ K_x \\ K_y \\ K_{xy} \end{pmatrix} \tag{5.15}$$

where,

$$A_{ij} = \sum_{K=1}^{N} \left(\bar{Q}_{ij}\right)_k (Z_k - Z_{k-1}) \tag{5.16}$$

is the extensional stiffness matrix,

$$B_{ij} = \frac{1}{2} \sum_{K=1}^{N} \left(\bar{Q}_{ij}\right)_k (Z_k^2 - Z_{k-1}^2) \tag{5.17}$$

is the extension-bending coupling matrix, and

$$D_{ij} = \frac{1}{3} \sum_{K=1}^{N} \left(\bar{Q}_{ij}\right)_k (Z_k^3 - Z_{k-1}^3) \tag{5.18}$$

is the bending stiffness matrix of the laminate.

The ply properties obtained from the rule of mixtures and ply orientation with respect to the load axis are used to calculate the laminate stiffnesses (A_{ij} , B_{ij} , D_{ij}). We can calculate the mid-plane strains and curvatures for a given set of laminate stiffnesses (A_{ij} , B_{ij} , D_{ij}) at a given load (P) using equation (5.15). The strains at the outer ply surface can be calculated from the mid-plane strains and curvature using equation 5.9 and can be compared with the strains obtained from an extensometer attached to the outer surface of the laminate during the test. For quasi-static ramp loading in tension, the mid-plane strains and curvatures are obtained from equation (5.15) using N_x = P N/m; $N_y = N_{xy} = M_x = M_y = M_{xy} = 0$. Thermal loads are also incorporated to take into account residual stresses and their effect.

5.2 Ply-discount Scheme

The strains in the outer surface of a laminate can be calculated given the loadings and the ply properties as explained in the previous section. To account for differences in laminate strains caused by damage in the individual plies, the ply properties need to be degraded. The degraded properties would reflect the effect of matrix cracking, for example on the global strain response to increasing loads.

The slope of the initial portion of the stress/strain curve for unidirectional

composites is given by the rule of mixtures ($E_c = v_f E_f + v_m E_m$). It is assumed that no matrix cracking or any other form of damage takes place in this linear portion till the critical cracking stress (σ_{cr}) calculated by the Budiansky's model is reached. According to the Budiansky's model, a steady state cracking occurs instantaneously at this critical stress. It is assumed that the matrix becomes incapable of carrying any load and the majority of the load at this juncture is being carried by the fibers. The ply properties are recalculated with E_m and G_m of the matrix reduced to zero. The strain response shows a jump at this stress level due to the sharp reduction in the values of the constituent matrix properties. The second linear portion of the graph corresponds to $v_f E_f$ as all the load is being carried by the fibers. Figure 39 illustrates the global strain response predicted by the ply-discount scheme.The laminate becomes more complaint after matrix cracking and the final failure occurs when all the fibers have broken.

Obviously, this simplified model does not accurately predict the behavior of real materials. The nonlinearity seen in BMC materials occurs over a wide strain range and there are no sharp jumps as predicted by the ply-discount scheme.Also, the assumption of steady state cracking occurring instantaneously at σ_{cr} is not correct. The matrix properties need to be degraded over a range of stress or strain levels.

5.3 AUSSR model for unidirectional ceramic composites

5.3.1 Introduction

The first attempt to use real-time AU data along with classical laminated plate theory to predict the strain response to increasing stress levels is presented

below. The ply properties were varied over a stress range with the help of real-time AU data by varying E_m and G_m of the matrix to incorporate the accumulating effect of increasing numbers of matrix cracks. The E_m and G_m of the matrix are varied linearly over $\Delta\sigma$ from 100 % to 0 %. The range of stress levels ($\Delta\sigma$) over which matrix cracks occurs is given by the onset and saturation of matrix cracking stress levels obtained from the AU data. Figure 39 shows the effect of the linear reduction of matrix properties (with the help of AU data) to predict the global strain response of the laminate. This model is an improvement on the more simple ply-discount scheme, but the predictions are still not close to the observed stress-strain response of a unidirectional ceramic composite. Although the prediction of the onset of the non-linear portion of the stress strain curve is close to the experimental data, the slope of the predicted curve at the onset of matrix cracking shows a sharp change, unlike the experimental data.

5.3.2 AUSSR model

The acousto-ultrasonic stress-strain response (AUSSR) model was formulated to study the failure mechanisms of unidirectional SiC/CAS ceramic composites. The model uses real-time AU data along with classical laminated plate theory to predict the strains measured at the outer plies in the gage section for a given load. Instead of using a linear fit to the AU data in the matrix cracking range, as in the previous section, a Weibull distribution was used to fit the variation of the real-time AU parameter with increasing stress levels. Researchers [90,92] have shown that the matrix crack density plotted versus stress follows a Weibull distribution; hence, a two parameter Weibull distribution was chosen here. Figure 40 shows the degradation of SWF values for a typical unidirectional SiC/CAS ceramic composite laminate and the corresponding Weibull distribution curve with Weibull parameters α = 15 and β = 235 MPa selected to approximate this

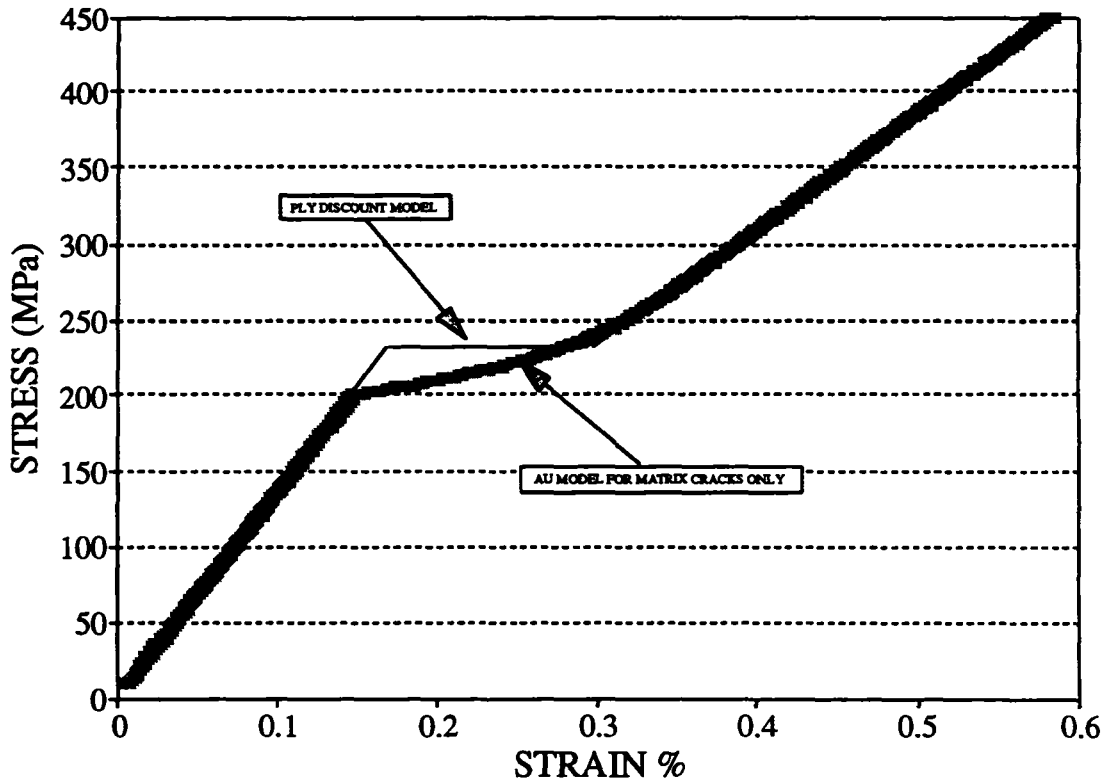

Figure 39. Strain response to increasing stress - ply discount scheme and linear variation of E_m and G_m over matrix cracking stress range.

degradation curve. The elastic moduli of the matrix material, E_m and G_m , used in the classical laminated plate theory fortran code are now varied over the same stress range from 100% to 0% using the same Weibull parameters $\alpha = 15$ (shape parameter) and $\beta = 235$ MPa (location parameter). Here it is assumed that the matrix degrades in a similar fashion compared to the real-time AU parameter SWF (M0). This assumption takes into account the effect of matrix cracking and its contribution to the observed global strains. Strains are then predicted for each increment of stress using classical laminated plate theory and the variation of matrix properties using Weibull parameters obtained from real-time AU data. The results of this calculation are shown in Fig. 41, together with the actual observed stress-strain curve.

The initial linear portion of the curve from prediction (E_c=136 GPa) is a close fit to the real data (E_c=131 GPa). The changes in the slopes in the nonlinear zone follows the same trends till 0.35% strain. The slope of the second linear zone of the predicted curve is $v_f E_f$ (fiber volume fraction * elastic moduli of fiber = 77 GPa) and is stiffer than the corresponding slope from the actual data.

Results from AU have shown the occurrence of local fiber breaks together with matrix cracking in this range. The difference between the relative actual compliance of the specimen compared to the AUSSR model is due to the loss of load bearing fibers because of the fiber breaks occurring during loading and is unaccounted for in this model. The final slope could be modified by $\xi v_f E_f$ ($0<\xi<1$), where ξ depends on the percentage of fibers broken until saturation of matrix cracks. Also the strains at which the second linear zone starts is less than the actual strain as the contribution from the additional strains caused by fiber breakage has not been accounted for in the AUSSR model.

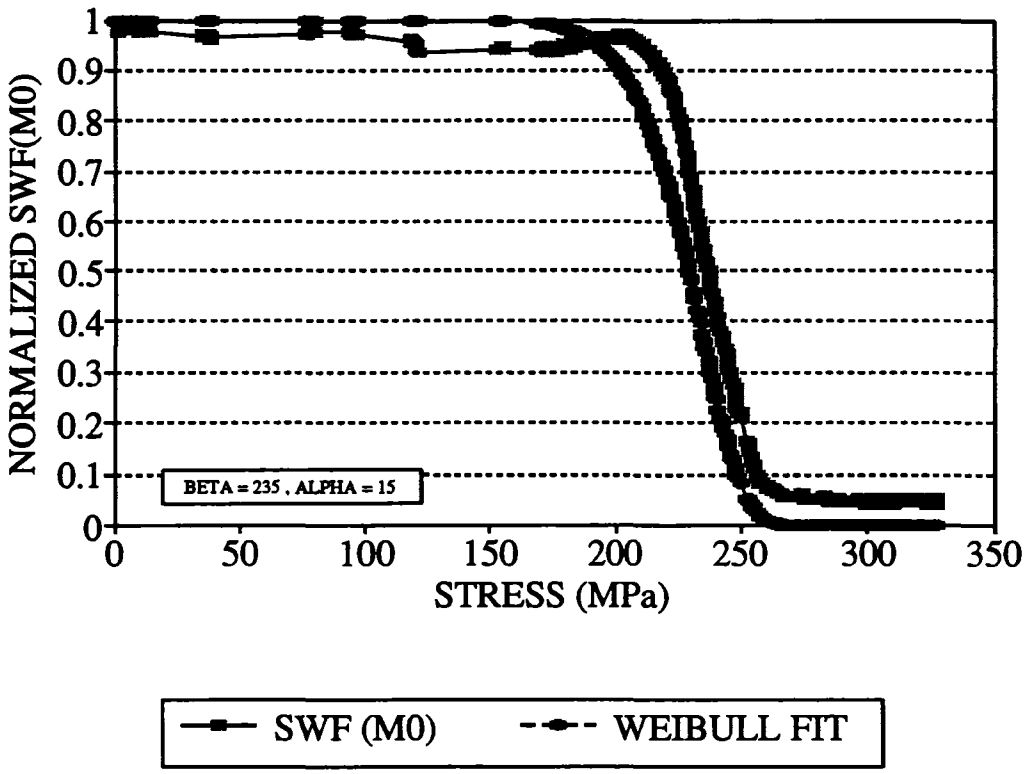

Figure 40. Weibull distribution fit to a typical AU (SWF(M0) data for SiC/CAS $[0_8]_s$ ceramic composite (α = 15 and β = 235 MPa)

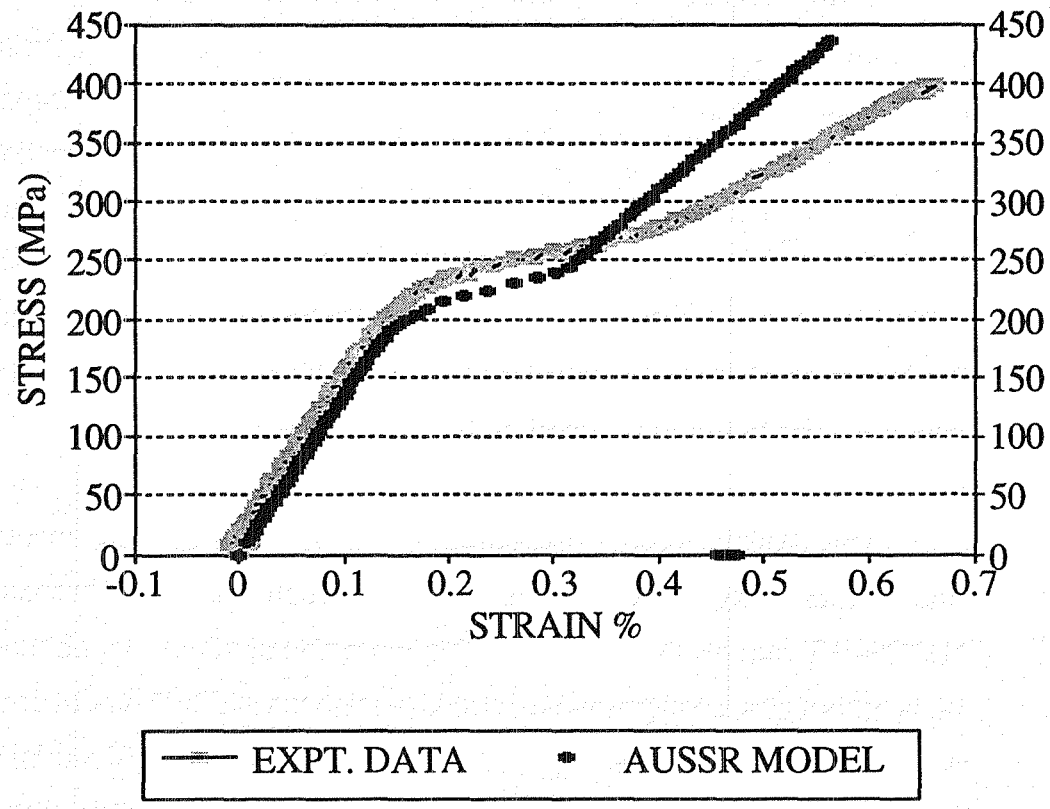

Figure 41. AUSSR model predictions and experimental stress-strain curve for unidirectional SiC/CAS $[0_8]_s$ ceramic composite.

5.3.3 AUSSR-WZ model

Zhu and Weitsman [95] presented a mechanics model which relates the response of a unidirectional ceramic composite laminate to matrix cracking, fiber-matrix interfacial slips and fiber breaks. Fiber breaks occurring during or before matrix cracking and their modulus softening effect were also incorporated along with matrix cracking to predict the strain response of the unidirectional ceramic composite laminate. Figure 42 obtained from the Weitsman and Zhu model (WZ model) shows the relative value of incremental strain due to fiber breaks $\Delta\varepsilon_s / \varepsilon$ vs σ_a, where ε is the total strain and σ_a is the global stress applied to the laminate. The incremental strain $\Delta\varepsilon_s$ calculated from the WZ-model uses constituent property values similar to the ones used in the present analysis.

The AUSSR model presented in the previous section accounts for only matrix cracks and hence was modified to account for fiber breaks to form an AUSSR-WZ model. The corresponding incremental strain $\Delta\varepsilon_s$ obtained from Fig. 42, is added at each increment of stress level to the AUSSR model predictions.The strain response to increasing stress level for the AUSSR-WZ model is presented in Fig. 43. The predictions of the AUSSR-WZ model are similar to the AUSSR model and closely follow the trend of experimental data till 0.35% strain. The additional strains from the WZ model over predicts beyond this range and hence the predicted global strains are higher than the experimental data, unlike the AUSSR model, although the slope of the AUSSR-WZ model is closer to the experimental data in comparison with the AUSSR model.

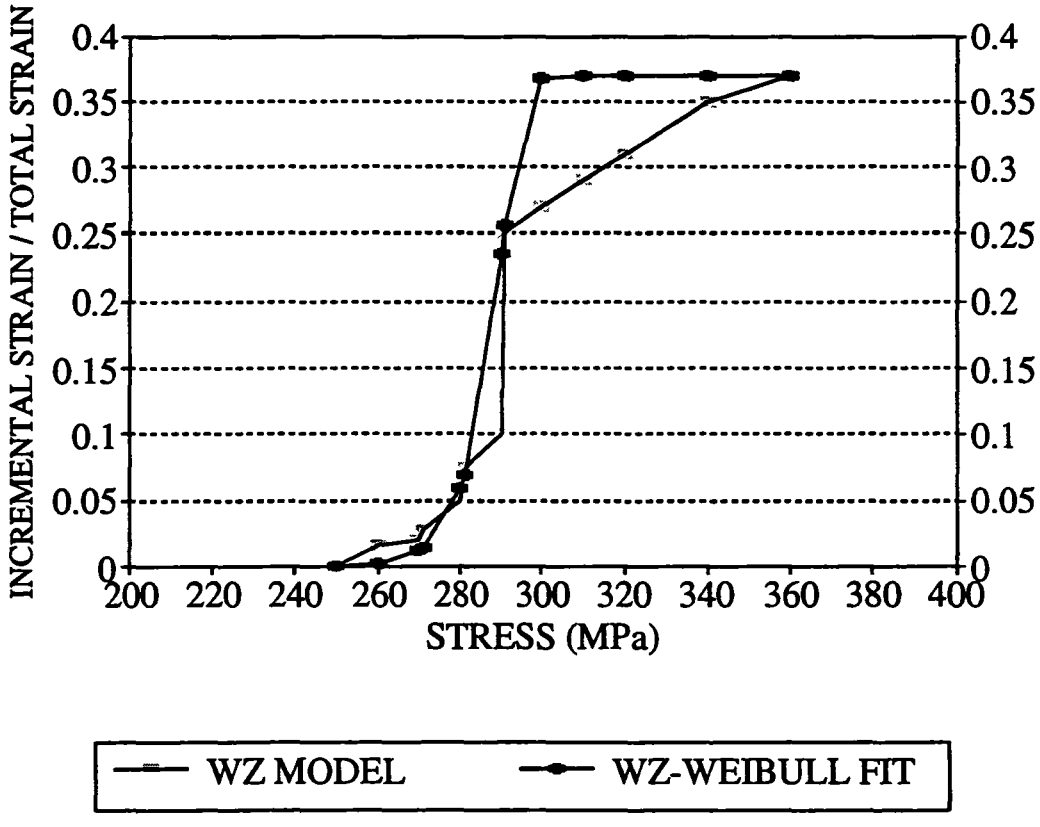

Figure 42. Weitsman's (WZ) model predictions of additional strains due to fiber breaks and Weibull distribution curve fit to the model. (α = 50 and β = 290 MPa)

5.3.4 AUSSR-WZ-WB model

The expected number of fiber breaks obtained from WZ model over a stress range follows a Weibull distribution [95]. A Weibull distribution with $\alpha_f = 50$ (shape parameter) and $\beta_f = 290$ MPa (location parameter) was used to fit the $\Delta\varepsilon_s / \varepsilon$ vs σ_a predicted from the WZ model as shown in Fig. 42. It is assumed that the majority of fiber breaks for this material system occurs at 290 MPa and at a very narrow range ($\alpha_f = 50$).

$$\frac{\Delta\varepsilon_s}{\varepsilon} = \{1 - e^{-(\frac{\sigma}{290})^{50}}\}\ 0.37 \tag{5.19}$$

The incremental strain obtained from equation 5.19 was added to the AUSSR modeling results to obtain predictions for an AUSSR-WZ-WB model as shown in Fig. 44. The AUSSR-WZ-WB model incorporates the additional strains due to fiber breakage by using Weibull parameters α_f and β_f.These Weibull parameters are different than the parameters used for modeling matrix cracks in the AUSSR models. The AUSSR-WZ and AUSSR-WZ-WB models show a secondary nonlinear zone (hump) caused by the prediction of a large amount of fiber breaks at approximately 290 MPa. It has been experimentally observed in a few samples that a large amount of fiber breaks occurs around 250 MPa. The Weibull parameter β_f was changed accordingly to the observed 250 MPa stress level and the strain response was recalculated for this modified AUSSR-WZ-WB model. Figure 45 shows the trend of strain response to increasing stress levels obtained from the modified AUSSR-WZ-WB model. This result follows closely to

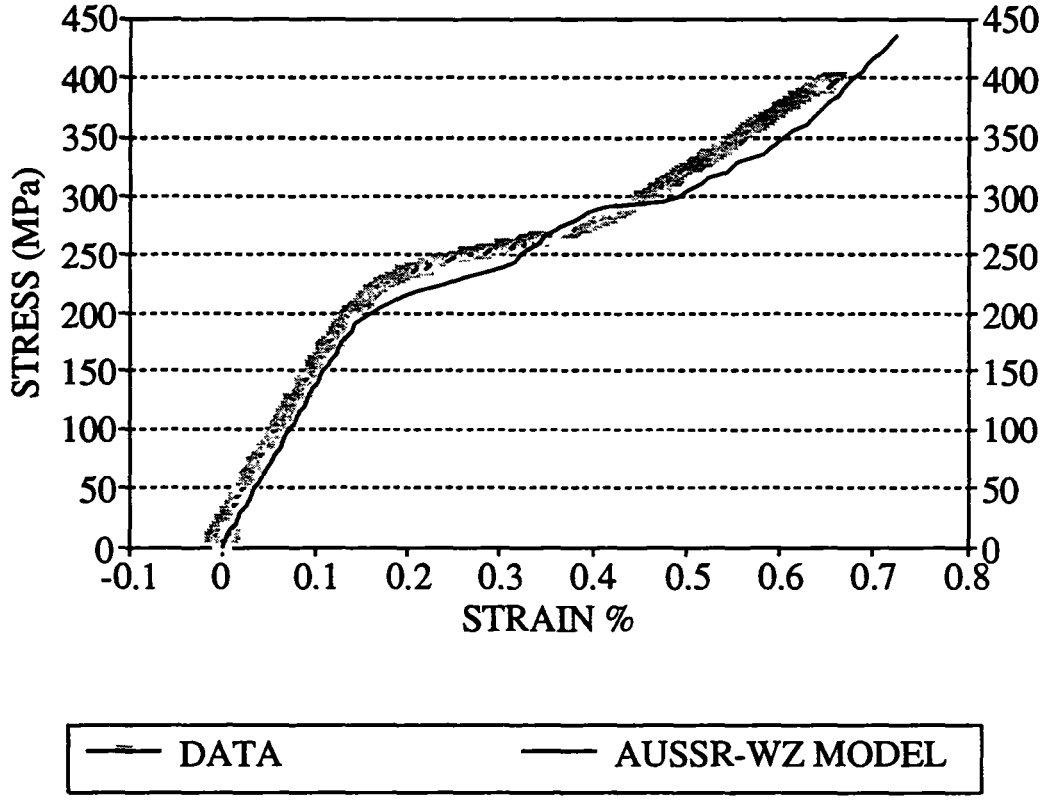

Figure 43. AUSSR - WZ model predictions and experimental stress-strain curve for unidirectional SiC/CAS $[0_8]_s$ ceramic composite.

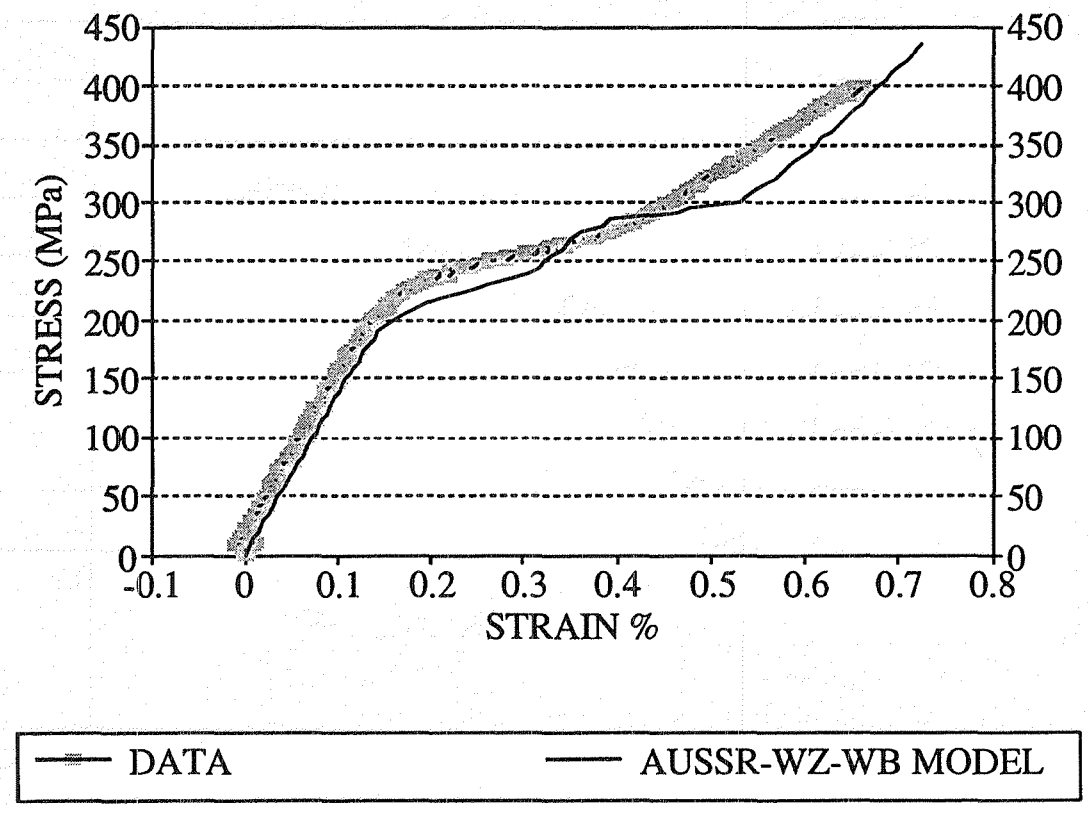

Figure 44. AUSSR - WZ - WB model predictions and experimental stress-strain curve for unidirectional SiC/CAS $[0_8]_s$ ceramic composite.

the experimental data and has no secondary non-linear zone. The slope of this model in the second linear range is higher than the experimental data although it is an improvement on the previous models. The onset of the second linear zone is still at a higher strain than the experimental curve as the additional strains are over-predicted by WZ model.

5.3.5 Modified AUSSR model

The AUSSR model was again modified to account for the average number of fiber breaks occurring during matrix cracking obtained from real-time AU data. The effective fiber volume fraction was re-calculated and the AUSSR model predictions were modified accordingly as explained below.

Sample U5 was loaded in tension until saturation of matrix cracks. The majority of load is being borne by the fibers at this juncture. It was the author's intention to calculate the energy in terms of SWF (M0) obtained from all the fiber breaks. As explained in chapter 4, the specimen was unloaded to zero load and reloaded to failure in constant displacement control mode. Extensive acoustic emission generated by the fiber breaks was observed between 350 MPa (0.508 mm) and 425 MPa (0.762 mm) as shown in Fig. 10. The sharp peaks were generated from fiber breaks, assuming no other damage mode was present, and all the load is being carried by the fibers after saturation of matrix cracks.The area under these local peaks was summed (Σ M0) to obtain the energy content from the damage events, namely, fiber breaks, based on the above assumption. It is also assumed that each fiber breaks once and loses its load bearing capability. It is further assumed that each fiber break generates the same amount of acoustic emission as the breaks occur in the same plane at a distance 'd' away from the AU receiver transducer.

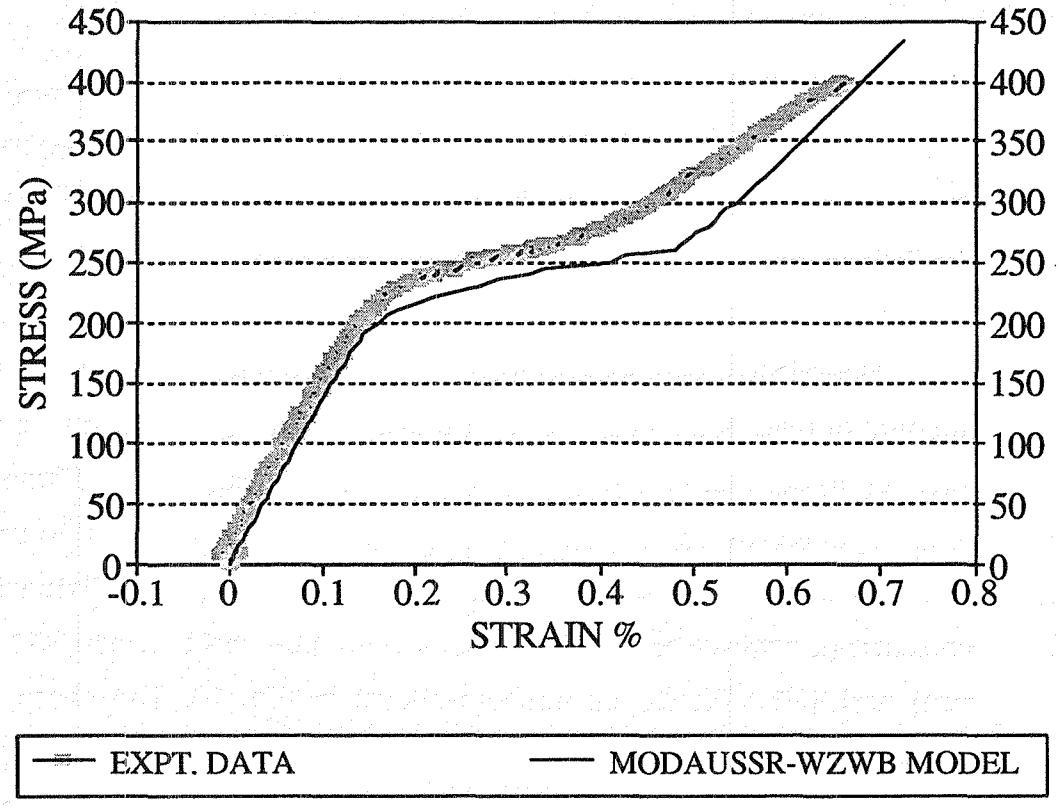

Figure 45. Modified AUSSR - WZ - WB model predictions and experimental stress-strain curve for unidirectional SiC/CAS $[0_8]_s$ ceramic composite.

The average number of fibers were calculated (87000) assuming the fiber volume fraction value (0.4) and fiber dimensions obtained from the manufacturer were accurate. The contribution from each fiber ($M0_f$) was calculated assuming each fiber breaks only one time. The local high peaks of SWF (M0) attributed to fiber breaks for a typical sample were summed and compared to $M0_f$ to calculate the average number of fiber breaks (20000) that have occurred prior to the ultimate failure zone. The effective fiber volume fraction (ξv_f=0.31) was calculated by assuming the broken fibers are not load bearing and hence could be assumed to behave as a matrix material filling up the volume without sharing any load [96].

The fiber volume fraction was altered to reflect the change after saturation of matrix cracks in the AUSSR model. The Weibull parameters α and β account for the effect of matrix cracking and the effective volume fraction accounts for the fiber breaks. The modified AUSSR model predictions shown in Fig. 46 approximates the experimental stress strain curve for a unidirectional SiC/CAS composite. The underlying assumption is that all fiber breaks which occur during matrix cracking occur at the one stress level after the saturation of matrix cracks and hence a jump in strain value is seen at that stress level in the modified AUSSR model predictions. The effective fiber volume fractions could be altered as and when the sharp peaks corresponding to fiber breaks are observed during static tests to obtain accordingly better modified AUSSR model predictions. The slope of the second linear zone ($\xi v_f E_f$ = 61 GPA) is closer to the experimental data than the other models. The prediction of the modified AUSSR model could be further improved by changing the effective fiber volume ratio over a range at which the fiber breaks occur. The onset of the second linear zone in the stress strain curve is experimentally higher than the predictions of the modified AUSSR model as the additional strain contribution was not taken into consideration. The ultimate

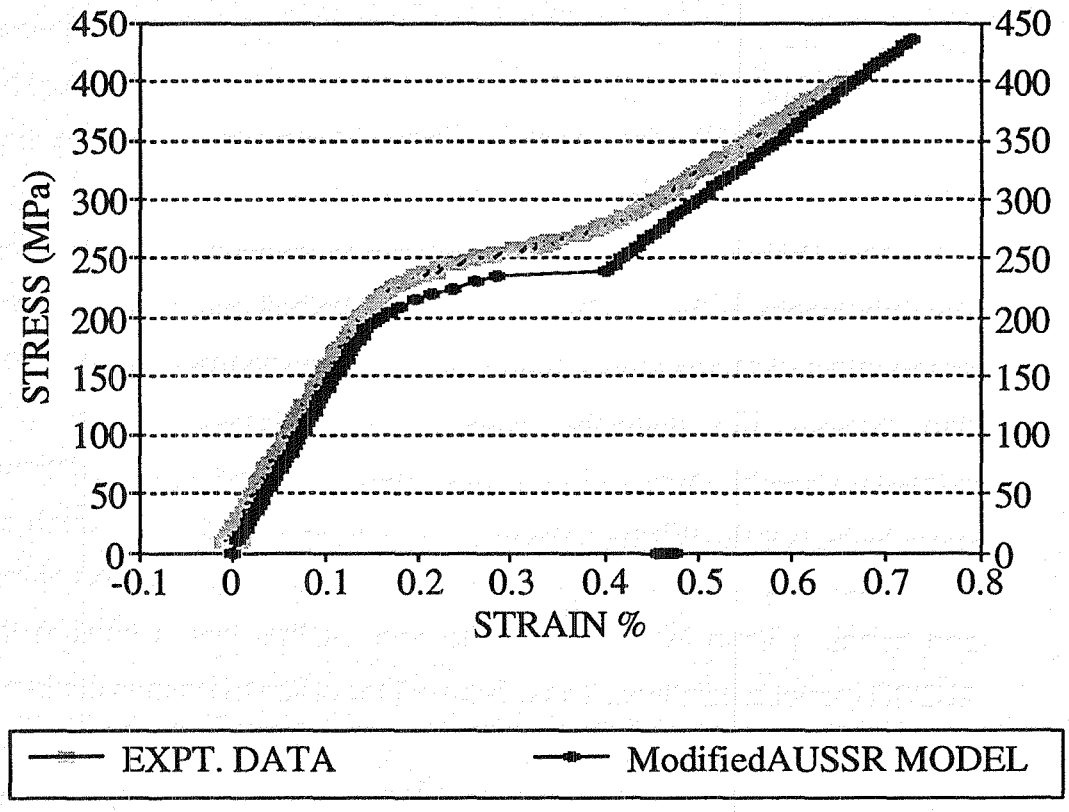

Figure 46. Modified AUSSR model predictions and experimental stress-strain curve for unidirectional SiC/CAS $[0_8]_s$ ceramic composite.

strength in all these models can be predicted by equation (4.6) although it is also an over prediction compared to the experimental results.

5.4 AUSSR model for cross-ply ceramic composites

Matrix cracking occurs in 90^0 plies prior to occurring in the 0^0 plies and occurs in both ply types over a range of stress levels, as indicated by real-time AU data. The ply properties used in the classical laminated plate theory fortran code for the AUSSR model were degraded accordingly by degrading the constituent properties of the matrix (E_m^0, E_m^{90}; G_m^0, G_m^{90}) for the respective plies from 100% to 0% over the respective stress ranges with the help of AU data. The degradation of elastic moduli for respective plies was done with the help of two sets of Weibull parameters α_{90}= 2.5, β_{90} = 60 MPa and α_0 =7, β_0 = 118 MPa. The β_0 value is half that of the Weibull location parameter β=235 MPa used in the AUSSR model for unidirectional composites as there are only eight 0^0 plies in comparison with 16 plies in the unidirectional SiC/CAS composite laminate. The stress ranges ($\Delta\sigma^{90}$ and $\Delta\sigma^0$) over which this matrix cracking takes place are obtained from the AU data. The Weibull shape parameters α_{90}= 2.5, β_{90} = 60 MPa and α_0 =7, β_0 = 118 MPa is obtained by approximating the AU data curve over each stress range ($\Delta\sigma^{90}$ and $\Delta\sigma^0$). The degradation of ply properties by degrading the elastic properties of the respective matrix constituent properties takes into account effect of global strain response to matrix cracking occurring in each ply.

Figure 47 shows the AUSSR model predictions for the strain response of a cross-ply SiC/CAS laminate $[0/90]_{4s}$ subjected to increasing stress levels along with the actual observed stress-strain curve. The trends are similar to the experimental curves with two non-linear zones each corresponding to matrix

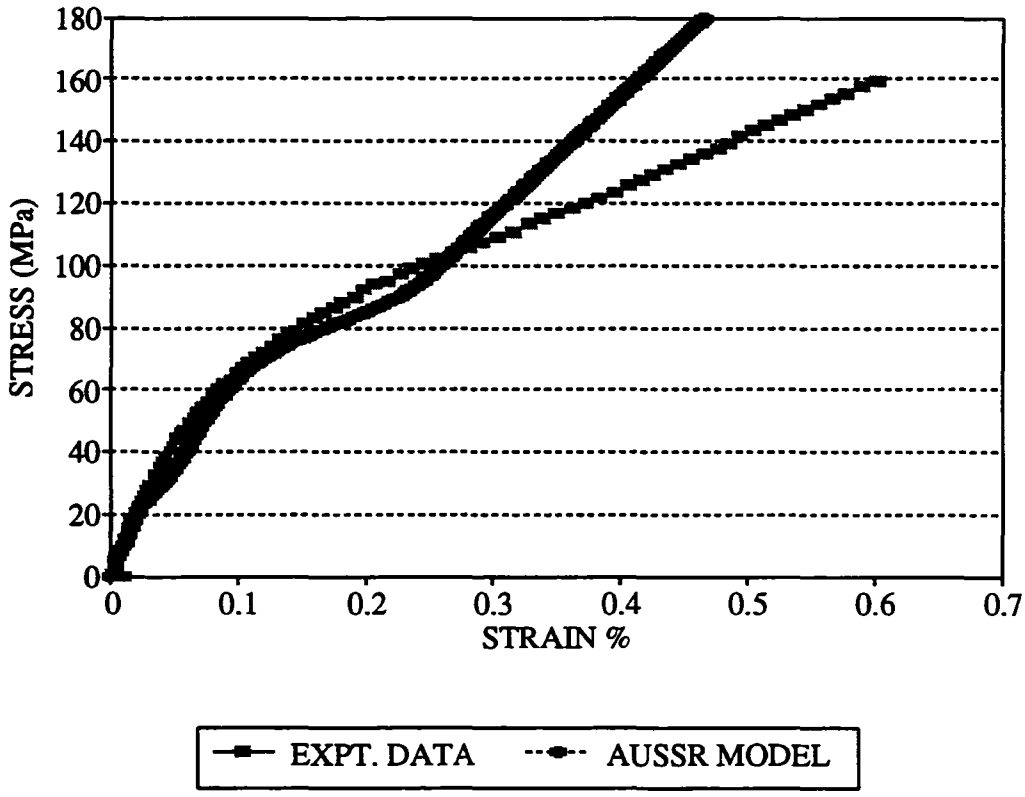

Figure 47. AUSSR model predictions and experimental stress-strain curve for cross-ply SiC/CAS $[0/90]_{4s}$ ceramic composite.

cracking in the 90^0 plies and 0^0 plies which occur in sequence. The initial slope of the curve is given by $E_c = E_{xx}$ obtained from the classical laminated plate theory. The predicted curve deviates from the actual stress-strain curve at 0.12 % strain. Further work needs to be done incorporate fiber break effects and to obtain the correct value of α_0 for a cross-ply laminate using a numerical technique to approximate the SWF degradation curve. After the initial degradation of the 90^0 plies, the damage progression and mechanism is similar to the unidirectional ceramic composite material.

5.5 Summary

The AUSSR model predicts strain response to increasing stress levels by incorporating the damage modes and their effect upon the global strain response of a laminate with the help of real-time AU data and classical laminated plate theory. The ply properties are varied according to the real-time AU data by varying the E_m and G_m of the matrix to take into account the occurrence of matrix cracks. The change in the elastic moduli due to matrix cracks causes the non-linear zone of the stress-strain curve generated by the model and closely fits the experimental data.

The Weibull shape parameter, α, denotes the spread of the range at which matrix cracking occurs. This parameter is a processing parameter; the larger the value of α, the smaller is the range over which matrix cracking occurs and thus the better is the reliability of the processing technique. The spread in the matrix cracking range is caused by defects and flaws created in the processing stage, producing crack initiation sites in the matrix material. This parameter could be used as a quality control tool. The location parameter, β=235 MPa, is nearly the critical

cracking stress level (σ_{cr}=207 MPa) calculated with the Budiansky, Hutchinson and Evans (BHE) model [83]. This model assumes steady state matrix cracking whereby cracking takes place at a certain critical stress level and not over a range as seen in real materials. The β parameter is dependent on the in-situ constituent properties, residual stresses caused by thermal coefficient mismatch between the constituents, and the properties at the interface. The Weibull parameters (α and β) obtained from the real-time AU parameter are used to closely predict the global strains on the edge of a laminate of SiC/CAS ceramic composites below approximately 0.35% strain as shown in the Fig.41. The modified AUSSR-WZ-WB model is a further improvement on the prediction of AUSSR model by incorporating fiber breaks, although the strains caused by fiber breaks are over predicted. The modified AUSSR model incorporates the fiber breaks during matrix cracking by altering the effective fiber volume fraction and is an improvement on all of the previous models.

The models developed by the author show the effects of each damage mode on the global strain response. The predictions of the models approximate the typical experimental curve and hence supports the assumptions made by the author in interpreting the AU results in terms of the different damage modes present and their onset and progression during static tests. The basic damage mechanisms during static tests are deciphered with the help of real-time AU data and supported by the AUSSR models.

The initial linear portion of the curve is the axial stiffness of the unidirectional SiC/CAS composite given by the rule of mixtures. The onset of non-linearity in the stress strain curve is caused by the onset of matrix cracking as shown in the AUSSR model and can be calculated from the Weibull parameters. The onset of the matrix cracking exposes the fiber to an oxygen rich environment

at high temperatures causing oxidative embrittlement of the interface and thereby causing catastrophic failure. The stress at the onset of matrix cracking calculated from the Weibull parameters should be used as a design stress instead of the critical cracking stress obtained from the Budiansky's model for thermo-structural applications.

The cross-ply AUSSR model shows a similar trend to the experimental data as both the model and the experimental data have two non-linear zones each corresponding to matrix cracking in the 90^0 and 0^0 plies respectively. The two non-linear zones in the stress strain curve have been modelled by two sets of Weibull parameters (α_{90}, β_{90} ; α_0, β_0) for 90^0 and 0^0 plies, respectively. Further work needs to be done to obtain the correct value of α_0 and also incorporate the effect of fiber breaks in the model. Damage mechanics of the cross-ply is similar to that for the unidirectional ceramic composite apart from the initial 90^0 plies degradation caused by the matrix cracks in those plies.

6. FATIGUE TESTING

6.1 Introduction

There were two primary objectives in conducting fatigue tests at room temperature. The first objective was to generate an S-N curve (load amplitude vs Log (failure cycles)) for un-notched cross-ply $[0/90]_{4s}$ SiC/CAS ceramic composite material system. S-N curves serve as a guideline for estimation of life of a structural component made of the same material when loads and in-service fluctuations of loads are known. The second objective was to monitor the damage progression during fatigue loading with the help of the real-time AU technique without interrupting the tests. Previously, researchers have monitored the damage state during fatigue by stopping the test at regular intervals and performing AU measurements under static loads. Thus, the feasibility of successfully assessing the damage in ceramic composites by AU has already been done. However, interrupting a test to perform AU measurements or other NDE tests could change the characteristics of the damage mechanism and, more importantly, the exact progression of damage might be missed. This is the first known time an AU practitioner has attempted to record AU data and assess damage in real-time under dynamic fatigue loads without interrupting the test. The real-time AU technique developed by the author is a non-disruptive, non-destructive technique to assess and monitor damage in ceramic composites. This technique also assists in studying the failure mechanisms of cross-ply SiC/CAS ceramic composites under cyclic loads.

Tension-tension (R=0.1) room temperature fatigue tests were conducted on cross-ply $[0/90]_{4s}$ SiC/CAS ceramic specimens at 10 Hz. The load amplitudes selected to run the fatigue tests ranged from 60% to 90% of the ultimate tensile strength (UTS). Validation of the real-time AU technique is presented in this chapter followed by the fatigue test results. The observed failure process is also described along with the experimentally determined S-N curve of the SiC/CAS cross-ply ceramic composite.

6.2 Validation of the real-time AU technique during fatigue tests

The AU technique needs to be validated before basing our conclusions on AU data regarding damage progression. To assure ourselves that the real-time AU technique monitors damage progression during a fatigue test, the AU technique was investigated first with the use of two control experiments. The real-time AU data recorded during cyclic loading is claimed to monitor the damage state and its progression. The changes in AU signals are claimed to have been caused by changes in the damage state and not due to extraneous signals from the noise produced by the fluctuating loads. The fluctuating stress level does have a fluctuating, but constant, effect on the AU signals. As long as the signals are averaged over at least one load cycle and the interval over which averaging is done is constant, the energy content of the received signal, as measured by the SWF (M0) averaged over one load cycle, is constant. Any change observed in the energy content of the received AU signal is then attributed to changes in the damage state level.

To validate these hypotheses, two controlled experiments on two different materials were performed. An isotropic material (mild steel) and a SiC/CAS ceramic composite specimen were selected for this experiment.

A mild steel specimen of dimensions similar to the ceramic specimens (6" x 0.5" x 0.13") was subjected to tension-tension fatigue (R = 0.1) at 10 Hz with the load amplitude at 20% of UTS. The fatigue testing conditions were similar to the ones used in subsequent SiC/CAS tests. A very low load amplitude was selected so as not to induce fatigue damage during testing. Real-time AU data were recorded without interrupting the test. The recorded AU signals were averaged over 10 cycles to obtain the AU parameter. The real time SWF (M0) parameter plotted versus cycles showed a flat, straight line. Hence, if no damage takes place at such low load amplitudes and there is no couplant degradation, the expected SWF (M0) versus elapsed cycles graph is found to be a straight line with zero slope.

A unidirectional SiC/CAS specimen sample G16 $[0_9]_s$ was loaded in quasi-static tension till saturation of matrix cracks. After saturation of matrix cracks, the load is carried by the fibers only. The specimen was then fatigued (R = 0.1; f = 10 Hz) at 25% UTS. The load level was again selected so as not to induce any additional damage during testing. Matrix cracks can occur at very low loads due to initial flaws in the specimens as shown in the previous chapters. SWF (M0) is very sensitive to matrix cracking and hence saturation of matrix cracks was allowed to take place prior to fatigue testing. This reduces any possibility of additional damage occurrence during the controlled experiment. Figure 48 shows the normalized SWF (M0) versus cycles for sample G16. The resulting graph is a flat line. The initial fluctuation was caused by the adjustment of load level during the initial cycles.

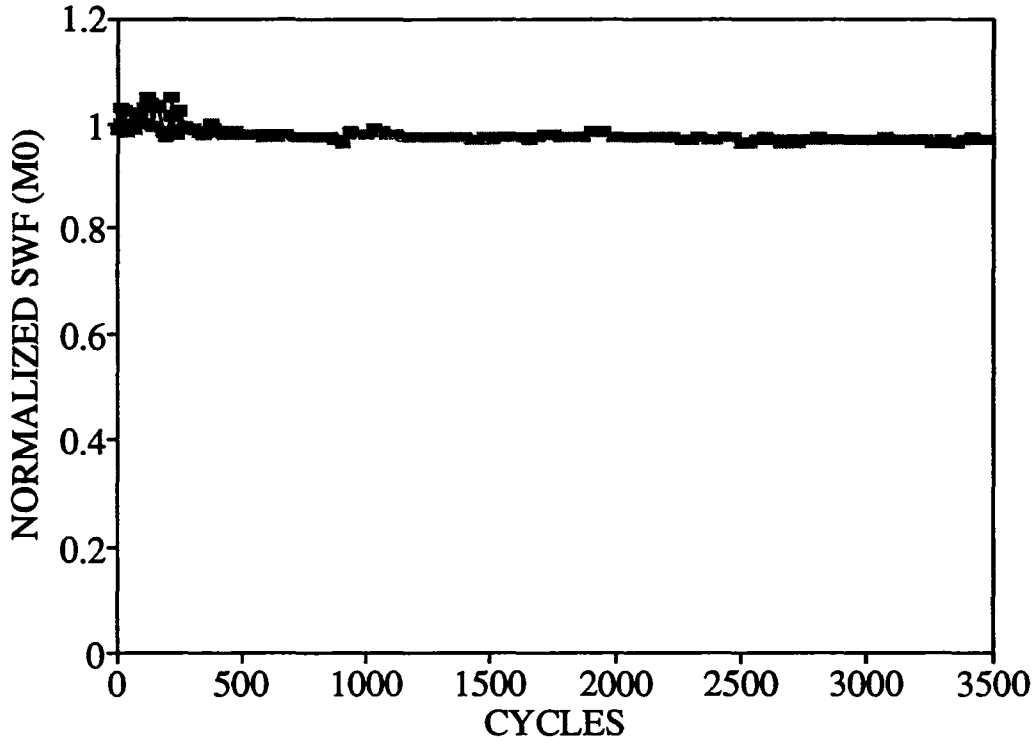

Figure 48. Validation of real-time AU set-up for fatigue testing.

These experiments validate the inherent assumptions of the real-time AU set-up. Any decrease in SWF (M0) values during fatigue can be attributed to an increase in damage. The real-time AU NDE technique can be used as a continuous, damage monitoring system.

6.3 Fatigue testing

6.3.1 Introduction

Fatigue tests were performed on SiC/CAS $[0/90]_{4s}$ specimens. The specimens were cut from a second SiC/CAS cross-ply plate (6.5" x 6.5" x 0.127") supplied by Corning Inc. C-scan and radiography were performed on the plate prior to cutting by a diamond wheel. Figures 49 and 50 show the c-scan and radiograph of the cross-ply plate with no observable porosity and inclusions. The dimensions of a typical cut specimen were 6" x 0.5" x 0.127". End tabs were attached to prevent crushing damage during loading. The edges were polished to facilitate good edge replication of surface damage.

To obtain an S-N curve, load amplitudes were selected in the range of 60% to 90% of ultimate tensile strength. At least three specimens were subjected to each of the load amplitudes of 60% and 90% of UTS. The remainder of the specimens were subjected to load amplitudes of 85% , 75% and 65% UTS. Two specimens from the first cross-ply plate were also cyclically loaded with load amplitudes of 66.66% and 75% respectively. The results of these latter two specimens were not included in generating the S-N curve as the densifications of

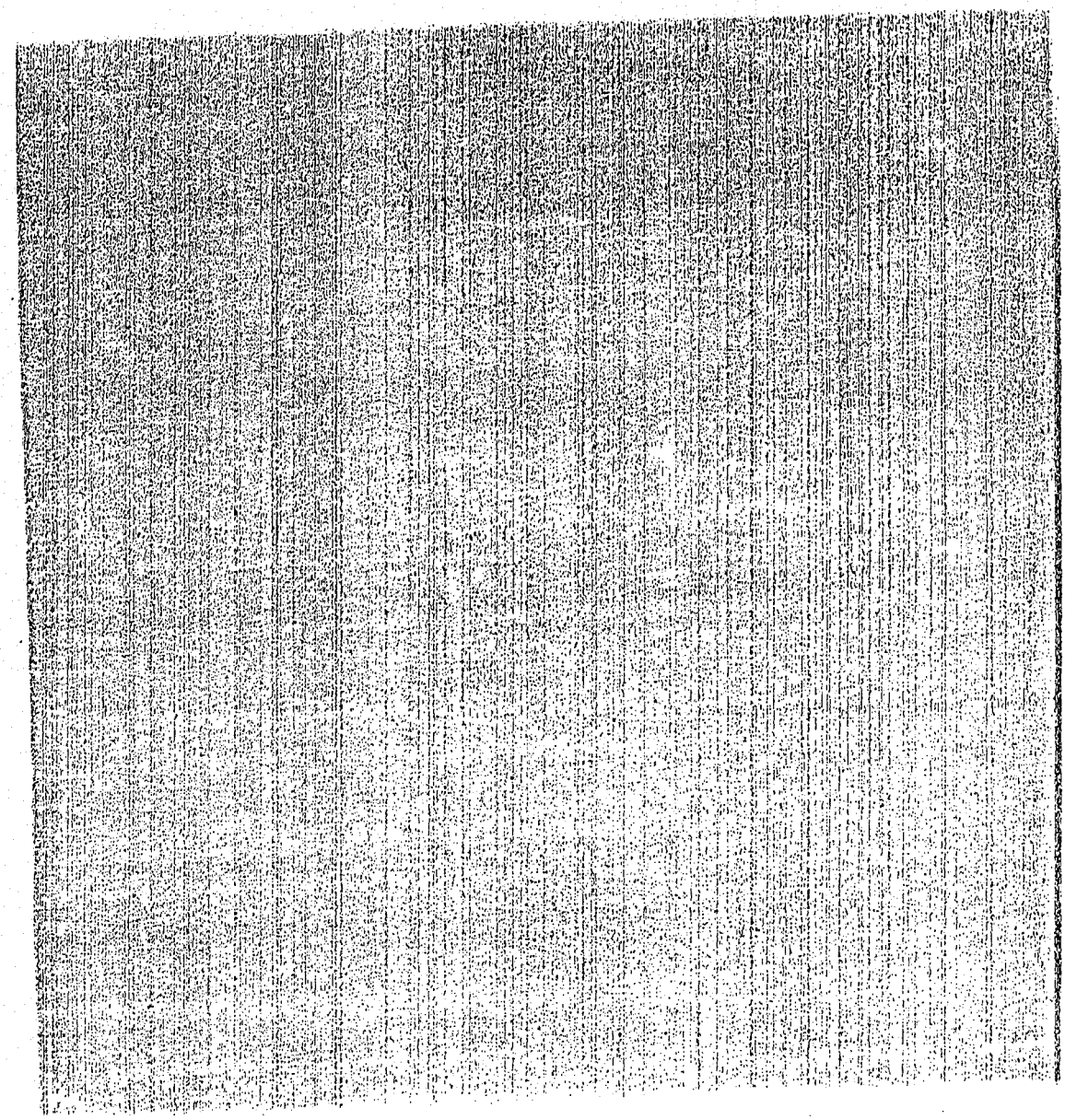

Figure 49. Ultrasonic C-scan of cross-ply SiC/CAS $[0/90]_{4s}$ ceramic composite plate

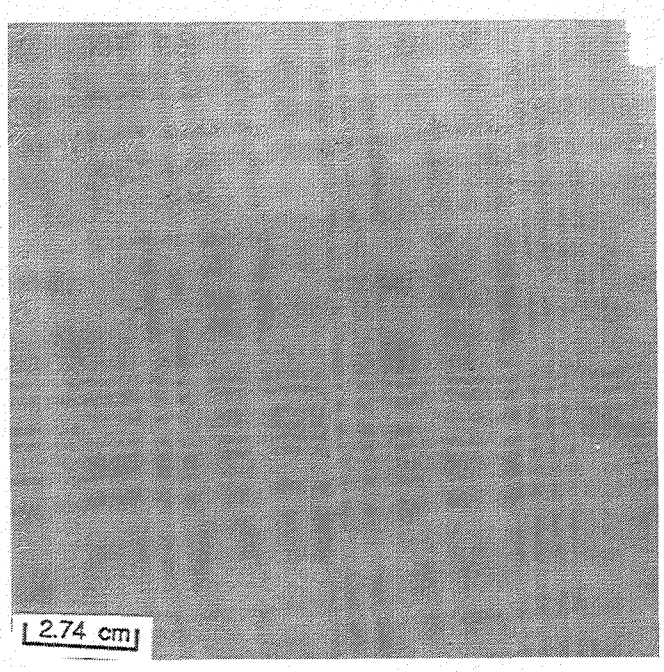

Figure 50. X-ray radiograph of cross-ply SiC/CAS $[0/90]_{4s}$ ceramic composite plate

the first and the second cross-ply plates were different.

Damage was documented at different points of the fatigue tests to study the failure mechanisms during fatigue. The monitoring of damage was done by recording and analyzing real-time AU signals. At least one test was run un - interrupted at each load amplitude. Other techniques used to document damage during a fatigue test are listed below.

Normalized dynamic stiffness versus cycles was also monitored. During fatigue, different damage modes occur at different times and each has an effect on the subsequent stiffness of the laminate. The progression of damage from initial onset to failure for the same load amplitude was observed to rarely deviate from specimen to specimen provided the test conditions were kept the same. If the normalized dynamic stiffness drops by x% before failure, one can stop the next specimen at the same x% of normalized dynamic stiffness and document the damage. The extent of damage is expected to be similar in both samples. Dynamic stiffness monitoring is also a real-time NDE technique and can be used to complement the AU results.

Edge replication of the damaged surface was done at each interruption of the tests. Edge replication shows the matrix crack density present on the damaged surface. Static stiffness has also been found to be a good parameter to monitor the damage state of the fatigued material. The trends from the static stiffness test obtained at each interruption of a fatigue test were compared also with the AU results.

X-ray radiography was performed at a few of the interruptions. Scanning electron microscope (SEM) analysis was also done on the failed surface to obtain

an insight to the failure characteristics of the specimens.

The fatigue results in this chapter are subdivided into three sections, namely, high load amplitude fatigue (80%-90% of ultimate tensile strength), medium load amplitude fatigue (70%-80% of ultimate tensile strength) and low load amplitude fatigue (60%-70% of ultimate tensile strength). The ultimate nominal tensile strength for the SiC/CAS $[0/90]_{4s}$ ceramic composite obtained from static tests was 163 MPa. The S-N curve obtained for this material is presented at the end of the fatigue results. Representative results of specimens at each load amplitude will be presented and discussed in detail.

6.3.2 High load amplitude fatigue

The graph of normalized SWF (M0) versus % life of sample C18 is shown in Fig. 51. This specimen was subjected to cyclic loading to failure without interruption (f = 10 Hz ; σ_{max} = 90% of ultimate strength and R = 0.1). The specimen failed in the gage section after 4053 cycles and a significant amount of fiber pullout was observed. The SWF (M0) values decreased by 60% in the first 8% of the fatigue life. The majority of matrix cracking had already taken place by this time as indicated by the AU data. A very slow decline in SWF values was observed till just prior to failure. The peak seen at 30% of the fatigue life can be attributed to acoustic emission, probably from fiber breakage. The receiving AU transducer acts as an AE transducer receiving additional high energy signals from the fiber breakage events. Figure 52 shows the formation of parallel transverse matrix cracks as observed in static tests.

Figure 53 shows the graph of normalized SWF (M0) and normalized static stiffness vs % of life for sample C12. The fatigue test was interrupted to document

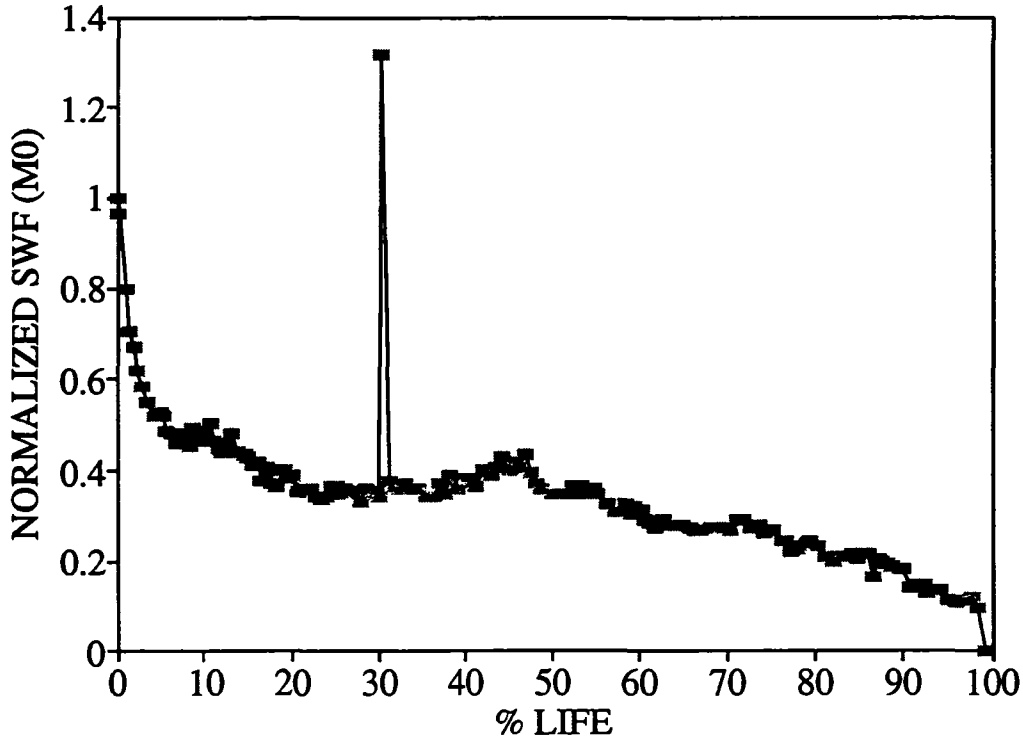

Figure 51. Normalized SWF (M0) vs % life for sample C18, SiC/CAS $[0/90]_{4s}$ (σ_{max}= 90% UTS)

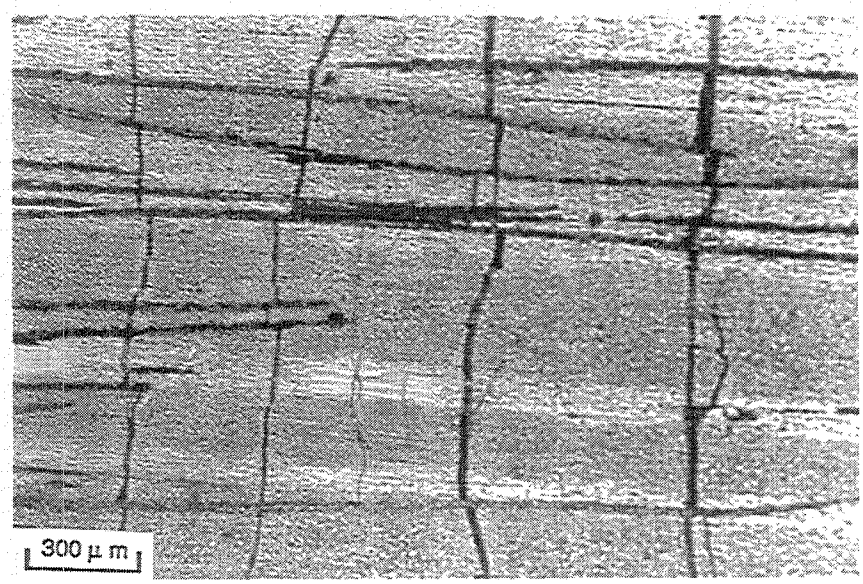

Figure 52. Photo-micrograph of transverse matrix cracks at failure in sample C18

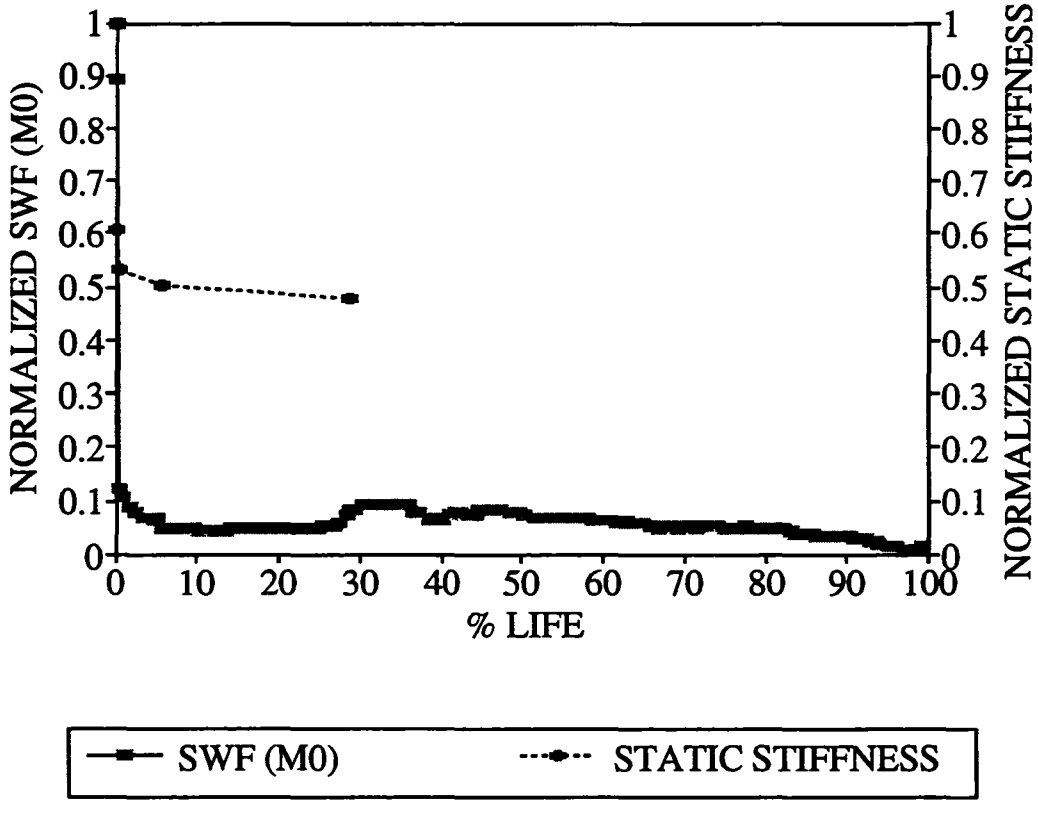

Figure 53. Normalized SWF (M0) and normalized static stiffness vs % life for sample C12, SiC/CAS $[0/90]_{4s}$ (σ_{max} = 90% UTS)

damage at various points of the fatigue life. Edge replicas of the damaged surface and static stiffness were recorded at each interruption. The SWF values drop by 95% at 8% of the fatigue life. The sharp drop is caused by matrix cracking occurring perpendicular to the load axis as observed in sample C18 and other brittle matrix composites. The SWF values thereafter show a gradual decline in their values until failure at 3482 cycles. The normalized static stiffness follows the same trend as the AU data. Figure 54 shows an enlarged view till 10% of life (350 cycles) to better illustrate this point. Significant fiber pullout was also observed at the failed section as shown in Fig. 55. Figure 56 shows fiber/matrix debond with the matrix crack propagating around the weak interface of sample C12.

Sample C13 was also subjected to cyclic loads at 90% of ultimate strength. The normalized SWF (M0) and normalized static stiffness follows similar trends throughout its fatigue life (N_f = 2243 cycles) as shown in Fig 57. Progressive damage on the specimen surface is seen in the successive edge replicas taken at different points of the fatigue life as shown in Fig. 58. Sample C19 was fatigued at 85% of ultimate strength without interrupting the test. A 70% initial drop in SWF (M0) values was observed at 10% of its fatigue life (N_f = 6791 cycles) as shown in Fig. 59. The SWF values increase just prior to failure. It is speculated that the cause of this increase could be due to acoustic emission from some damage events being detected over an extended number of cycles. The failure surface characteristics showed no deviation from the previous samples and hence further investigation needs to be done to verify this supposition.

6.3.3 Medium load amplitude fatigue

Sample C17 was fatigued at 75% of ultimate strength. The initial drop in SWF (M0) is 80% in the first 10% of its fatigue life (N_f = 50147 cycles), followed

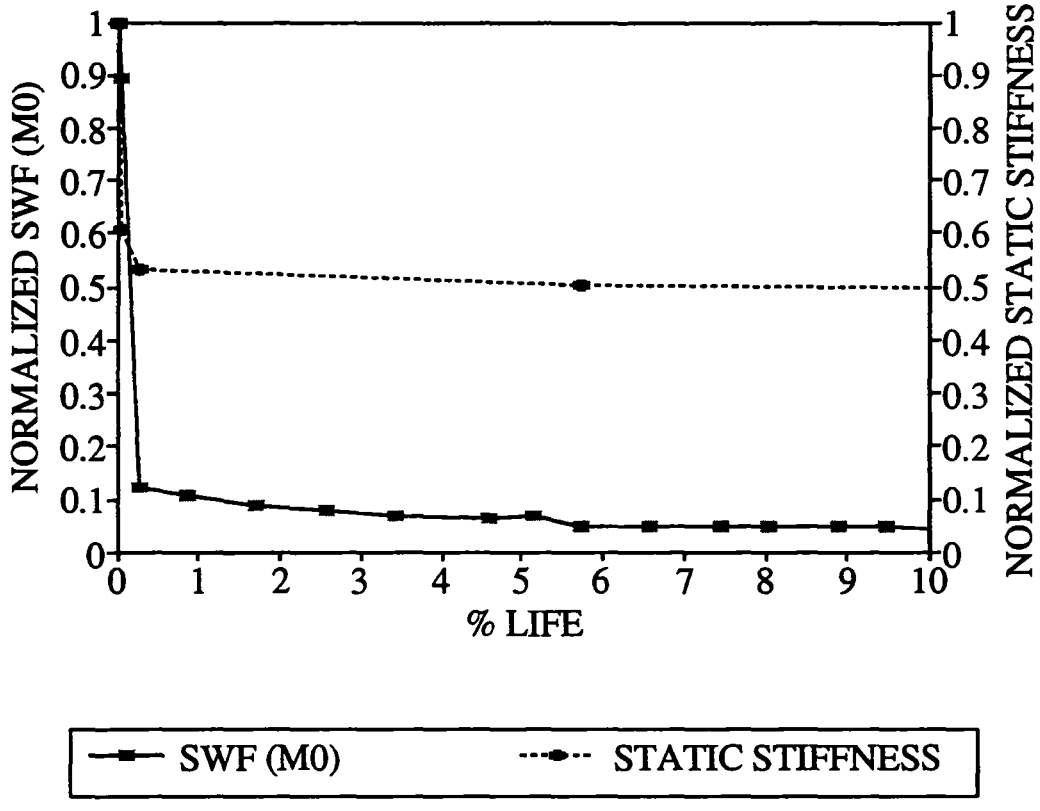

Figure 54. Normalized SWF (M0) and normalized static stiffness vs % life for sample C12, SiC/CAS $[0/90]_{4s}$ at early life (σ_{max} = 90% UTS)

(a)

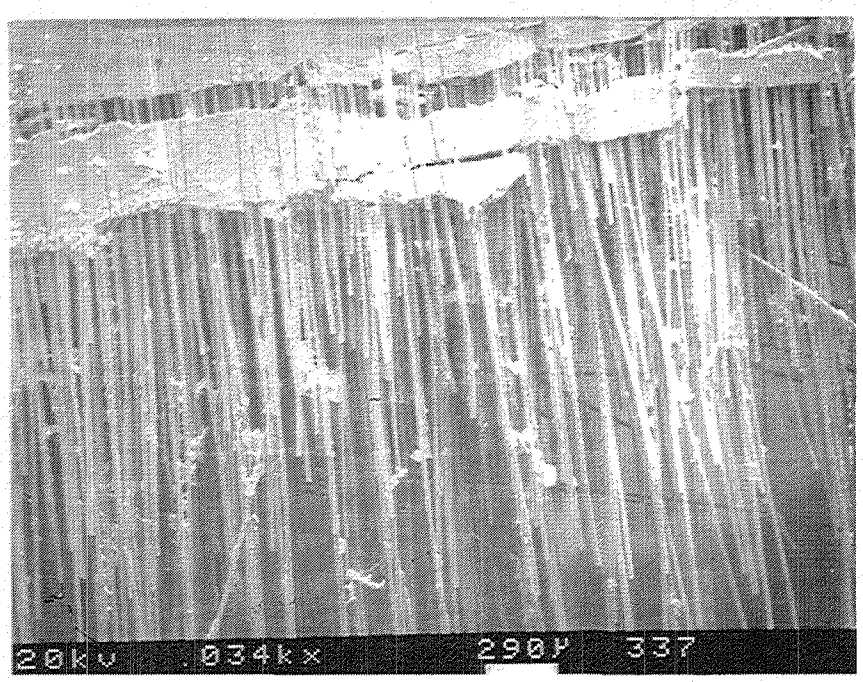

(b)

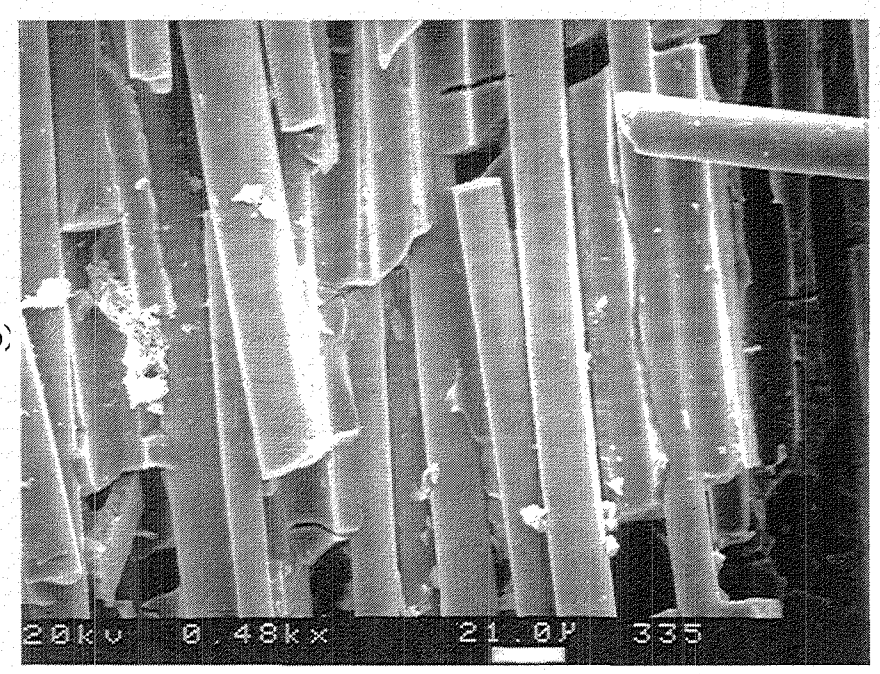

Figure 55. (a) SEM photo-micrograph of the failure surface of sample C12, SiC/CAS $[0/90]_{4s}$, (b) An enlarged view of the failure surface

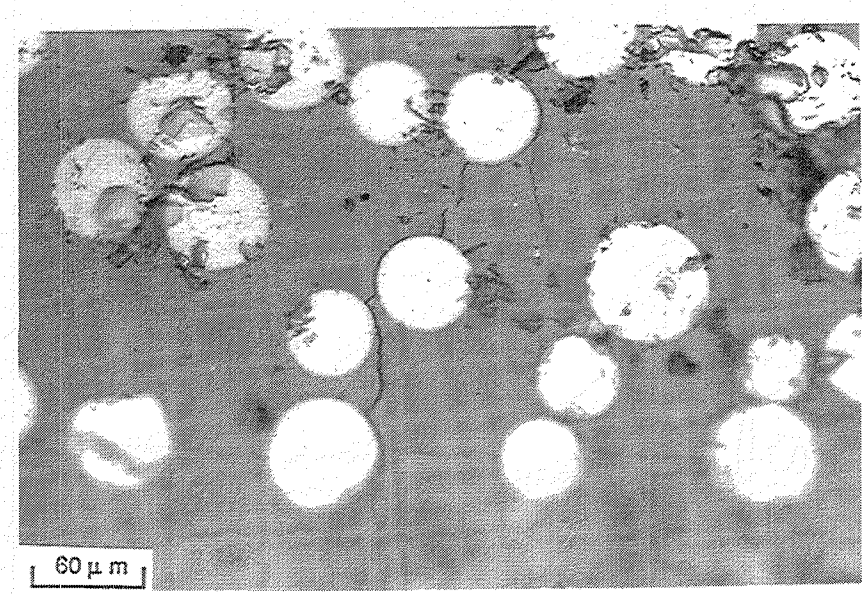

Figure 56. Photo-micrograph showing debonding at the fiber/matrix interface of sample C12, SiC/CAS $[0/90]_{4s}$

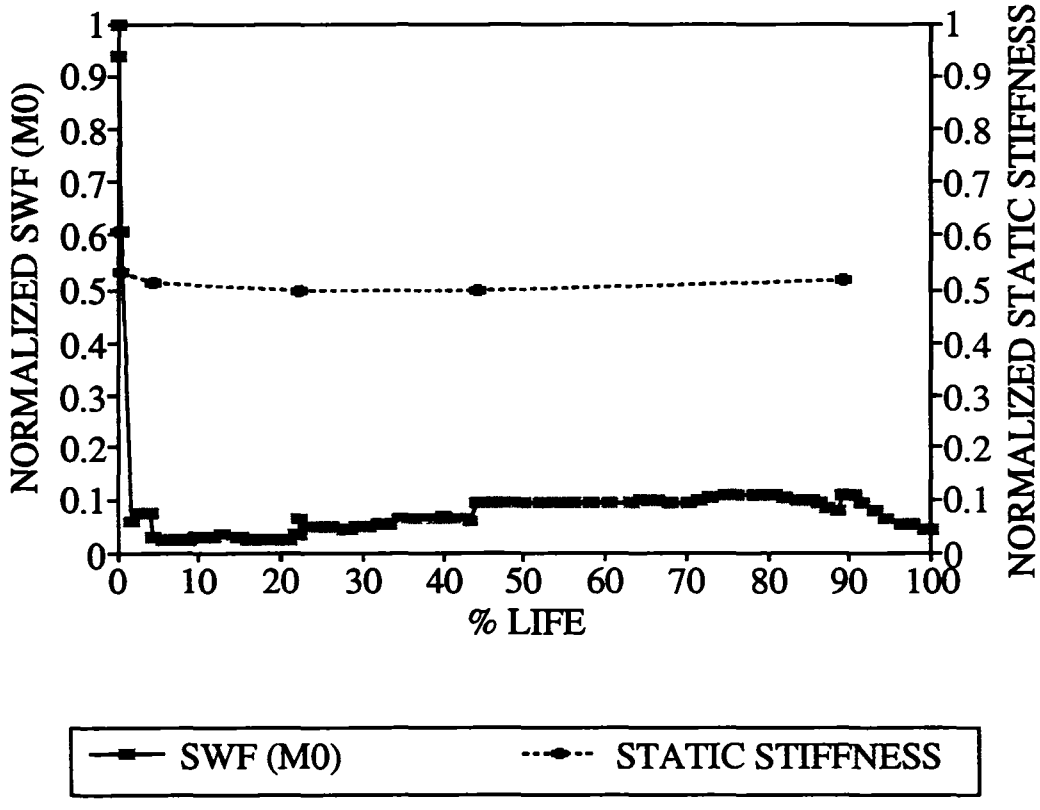

Figure 57. Normalized SWF (M0) and normalized static stiffness vs % life for sample C13, SiC/CAS $[0/90]_{4s}$ (σ_{max} = 90% UTS)

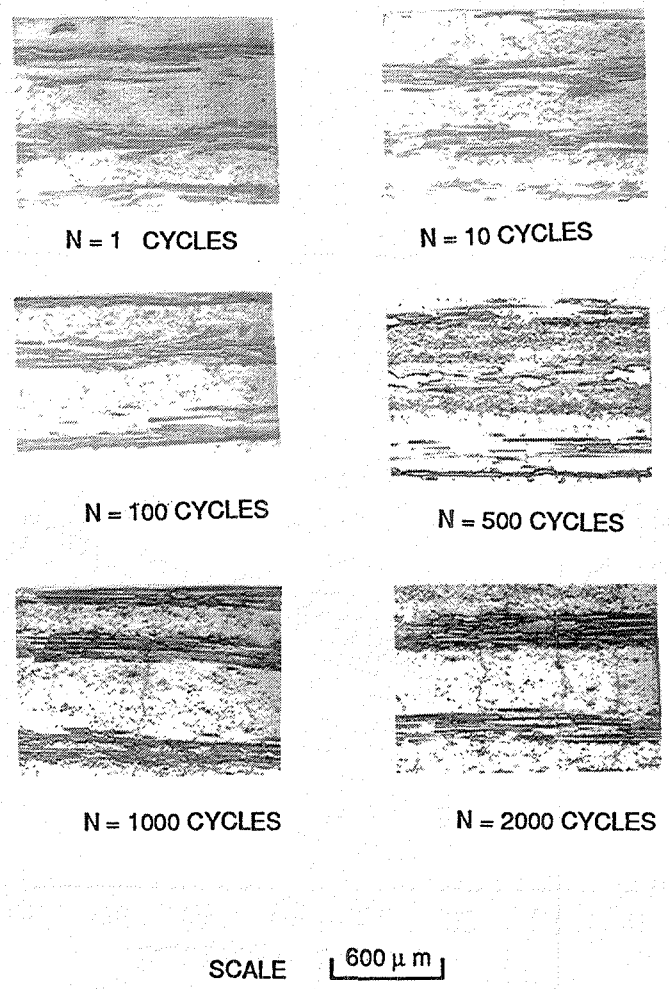

Figure 58. Edge replicas of the damaged surface of sample C13, SiC/CAS $[0/90]_{4s}$ (σ_{max} = 90% UTS)

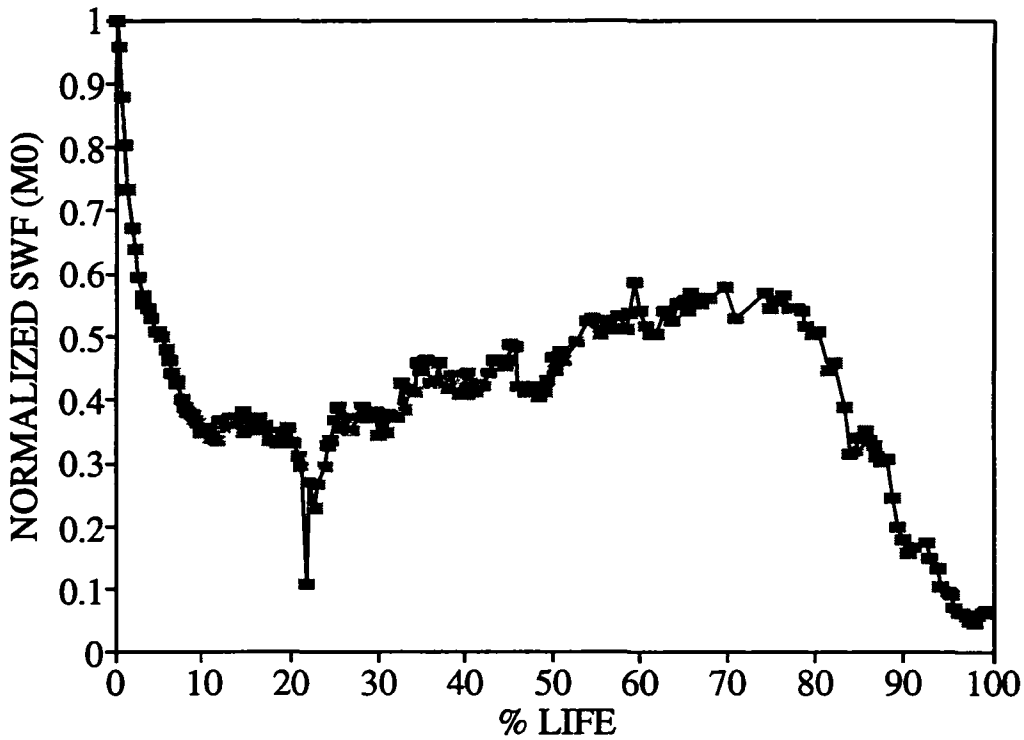

Figure 59. Normalized SWF (M0) vs % life for sample C19, SiC/CAS $[0/90]_4$. (σ_{max} = 85% UTS)

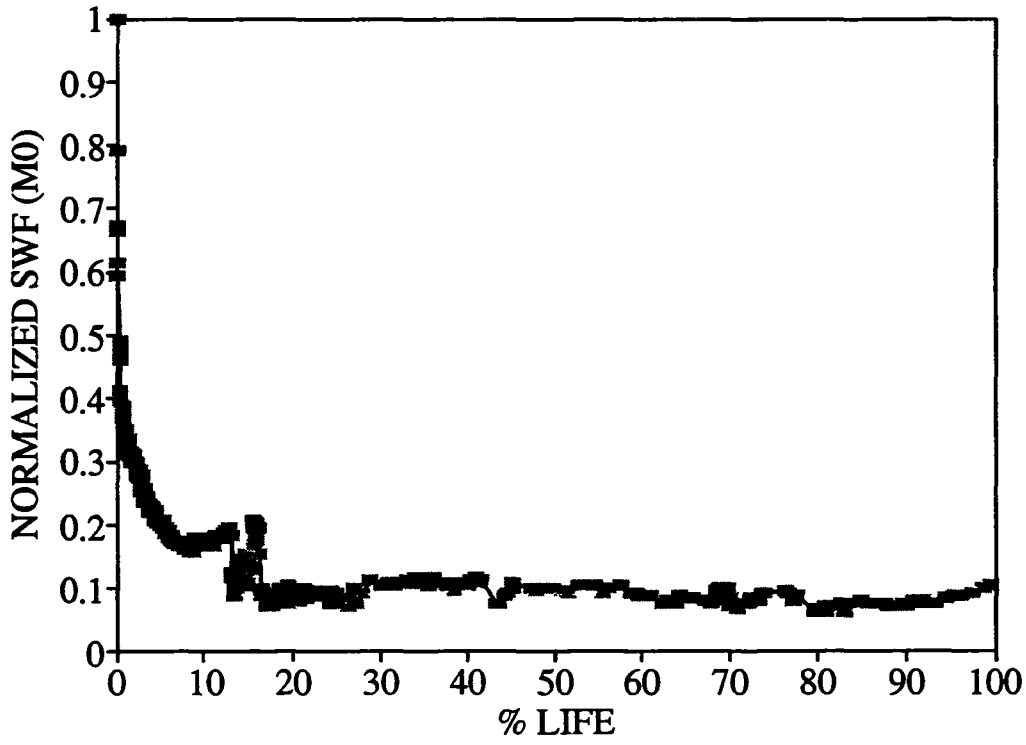

Figure 60. Normalized SWF (M0) vs % life for sample C17, SiC/CAS $[0/90]_{4s}$ (σ_{max} = 75% UTS)

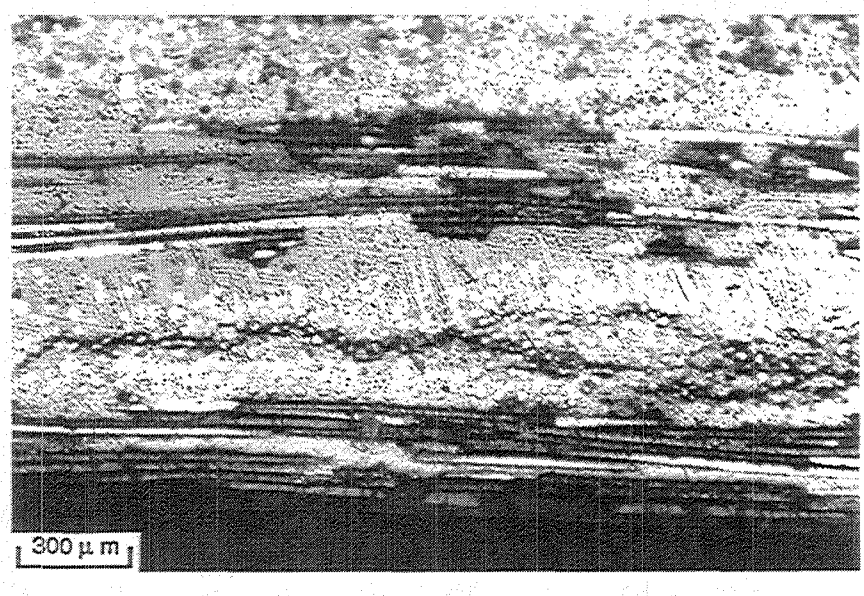

Figure 61. Local delaminations in the 90° plies of sample C17, SiC/CAS $[0/90]_{4s}$ (σ_{max} = 75% UTS)

by a flat curve till failure as shown in Fig. 60. The initial drop in SWF values is also more gradual in comparison with the higher load amplitude fatigue test results. There are small jumps in SWF values seen at 15% of the fatigue life prior to a flat curve. These jumps could have been caused by acoustic emission from damage events occurring during these cycles. Figure 61 shows local delamination connected by transverse matrix cracks in the 90^0 plies. This damage mode is not seen in similar specimens with the same lay-up subjected to static loads.

Sample C4 was also fatigued at 75% ultimate strength. Figure 62 shows the normalized SWF and normalized static stiffness values plotted with the corresponding number of cycles for sample C4. Stiffness measurements and SWF values follow the same trends indicating damage accumulation with the increasing number of cycles. The majority of damage takes place before 25 cycles (2.5% life). The specimen failed at 961 cycles, very low in comparison with other samples tested at the same load amplitude. The difference may have been a result of the specimens being cut from two different plates.

6.3.4 Low load amplitude fatigue

Sample C11 was subjected to cyclic loading at 60 % of the ultimate strength. Figure 63 shows the graph of normalized SWF (M0) and normalized static stiffness vs % of life for sample C11. The static stiffness shows a trend similar to the AU data. An enlarged view showing the variation of SWF (M0) and static stiffness till 500 cycles is plotted in Fig. 64. The majority of the damage occurred in the first few cycles. Edge replicas showing progressive damage at different cycles is shown in Fig. 65. The specimen failed at 488,743 cycles at one end tab with extensive fiber pull-out as shown in Fig. 66. Figure 67 (a) and (b) are SEM photomicrographs showing dynamic fracture of the fibers at failure with fibers

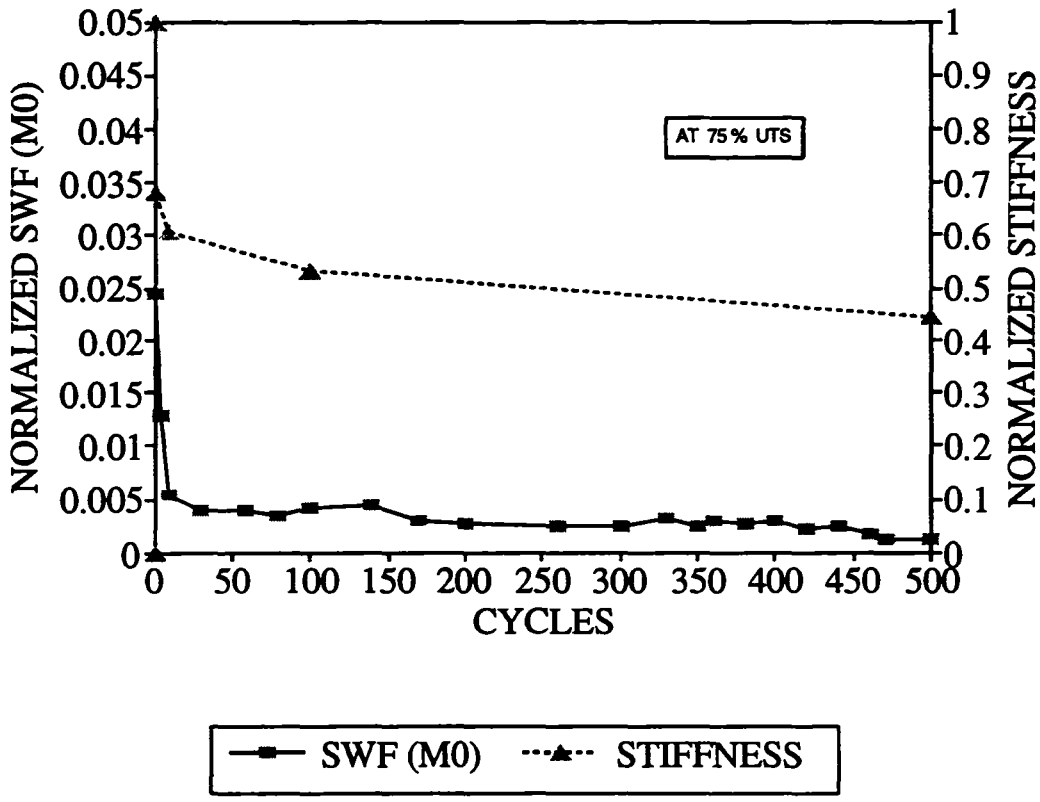

Figure 62. Normalized SWF (M0) and normalized static stiffness vs cycles for sample C4, SiC/CAS $[0/90]_{4s}$ (σ_{max} = 75% UTS)

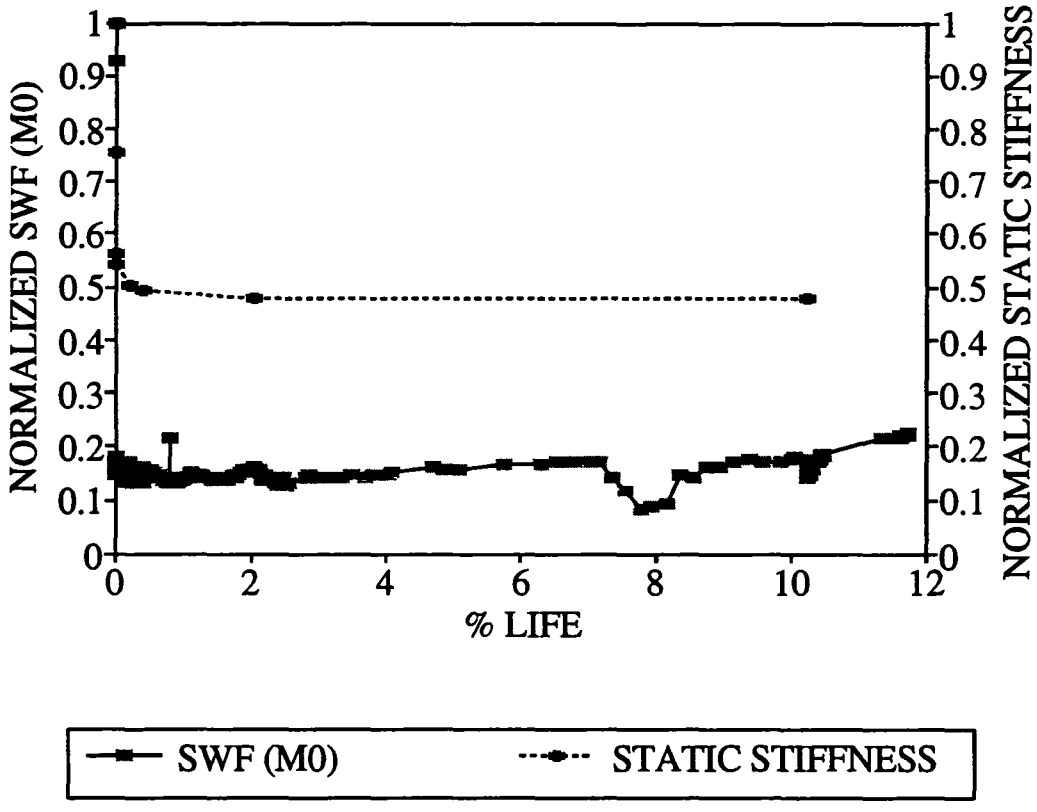

Figure 63. Normalized SWF (M0) and normalized static stiffness vs % life for sample C11, SiC/CAS $[0/90]_{4s}$ (σ_{max} = 60% UTS)

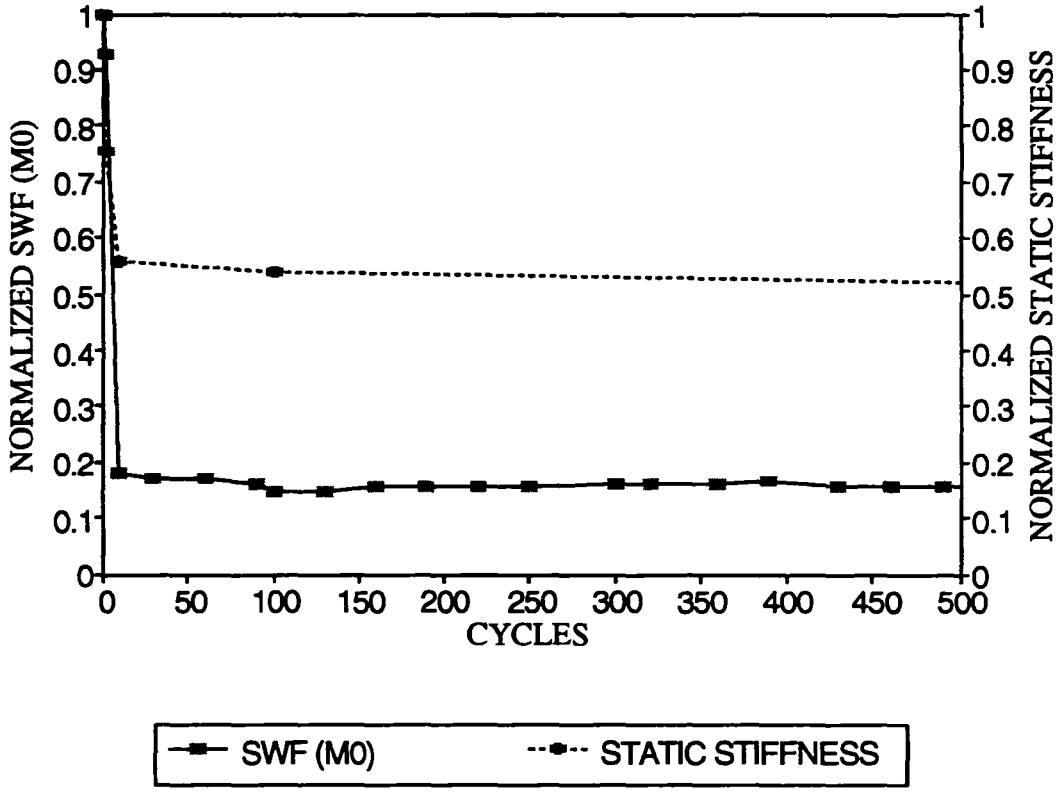

Figure 64. Normalized SWF (M0) and normalized static stiffness vs cycles for sample C11, SiC/CAS $[0/90]_{4s}$ at early life (σ_{max} = 60% UTS)

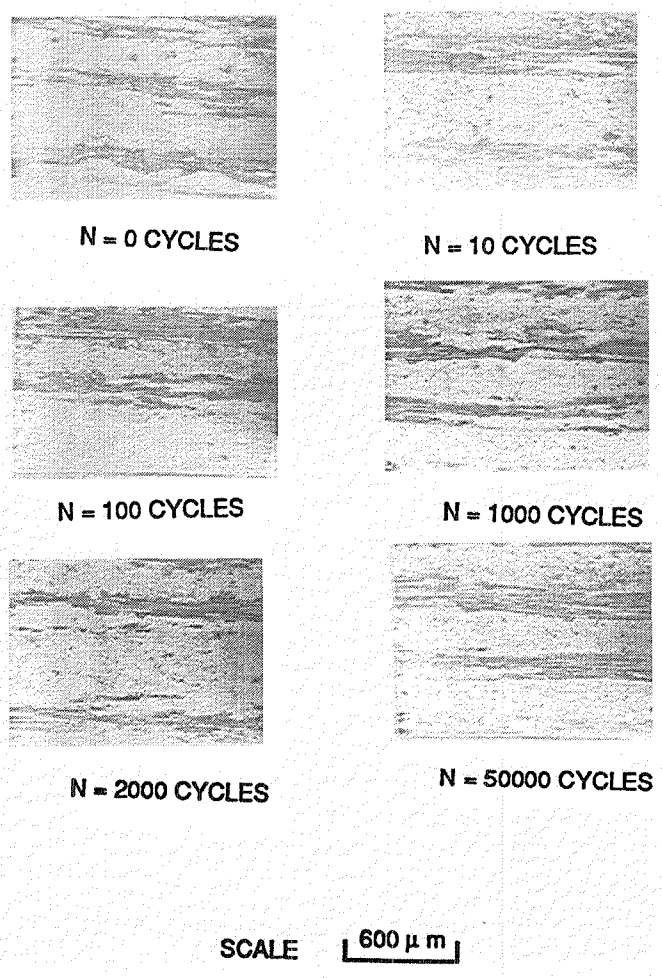

Figure 65. Edge replicas of the damaged surface of sample C11, SiC/CAS $[0/90]_{4s}$ (σ_{max} = 60% UTS)

Figure 66. SEM photo-micrograph of the failure surface of sample C11, SiC/CAS $[0/90]_{4s}$

(a)

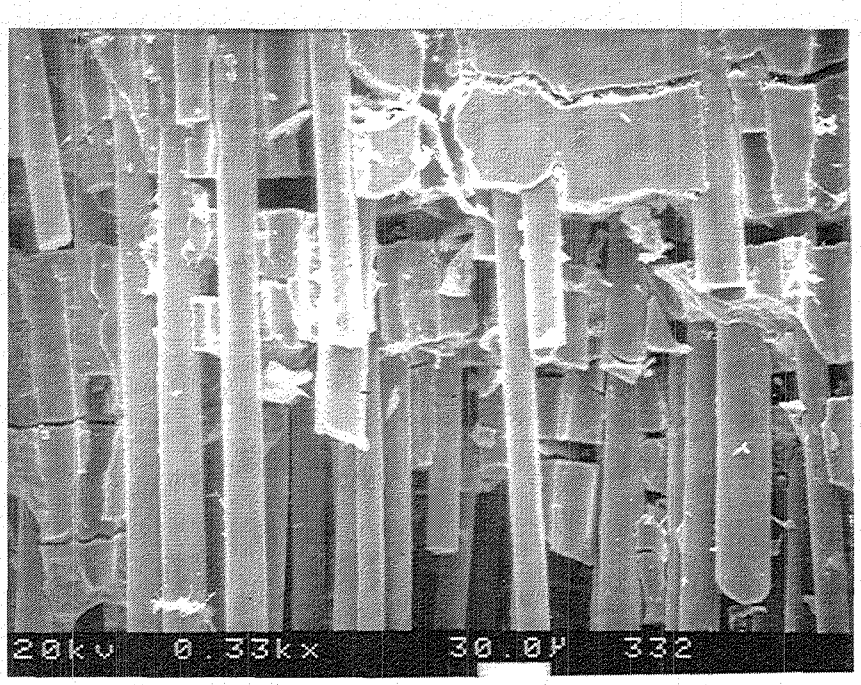

(b)

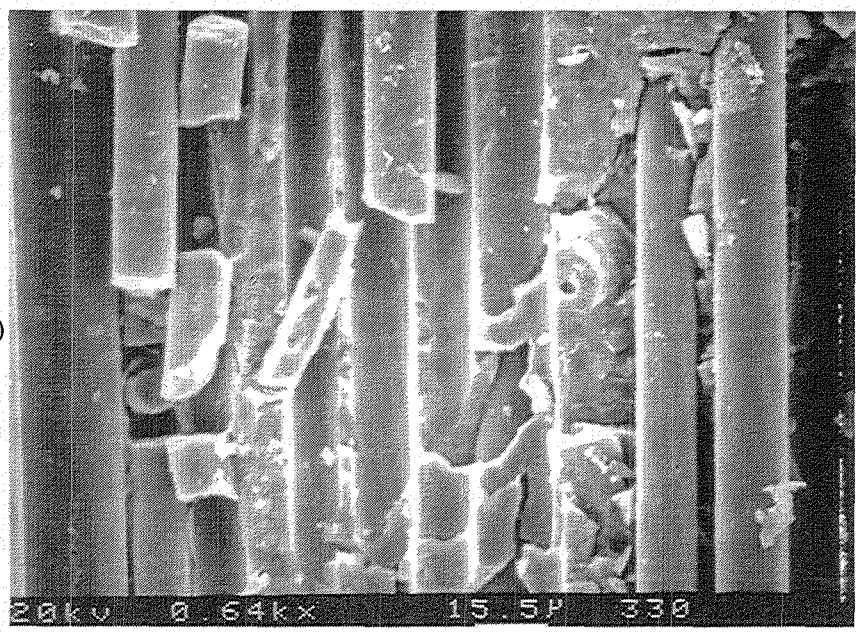

Figure 67. (a) SEM photo-micrograph of the failure surface of sample C11, SiC/CAS $[0/90]_{4s}$, (b) An enlarged view

in the path of the final catastrophic crack propagation breaking more than once. The fibers are clean indicating a weak interface-no bond situation between the fibers and matrix.

Sample 16 and Sample 20 were fatigued also at 60% ultimate strength. The trends of SWF (M0) values are similar to C11 and are shown in Fig. 68 and Fig. 69. The cycles to failure for C16 and C20 are 317,929 and 374,913 cycles respectively. The failure locations for all three samples (C11, C16 and C20) were at the end tabs as shown in Fig. 70. It appears to be a shear mode failure at the end tabs. The initiation of the final failure is at the mid $[90]_2$ plies caused by matrix cracks connecting in the mid 90^0 plies with delamination and the adjacent 0^0 plies matrix cracks. The connected cracks become critical, causing localized fiber fracture which results in the final failure of the laminate. The initiation of the final failure for low stress amplitude fatigue is at the end tabs due to the global stress concentration caused there by the gripping action. The conical shape of the failure surface is due to the effect of the post-initiation failure mechanism. The post-initiation failure path seeks the free edge which is not in the same plane due to the extension of the end tabs. The closest free edge is at the end of the end-tabs which is at a distance (d) from the failure initiation plane. The distance (d) depends on the location of the grips with respect to the end-tabs. This determines the conical shape of the failure surface. High stress amplitude fatigue shows a similar final failure mechanism. In the latter case, the closest free edge is in the same plane and hence the failure surface produced is perpendicular to the load axis. The post-initiation failure path in both cases seeks the nearest free edge as the stress intensity factor k_I is increased due to the close proximity of the free edge.

Sample C3 was cyclically loaded at 66.66% of ultimate tensile strength. Figure 71 shows the normalized SWF and normalized stiffness values plotted

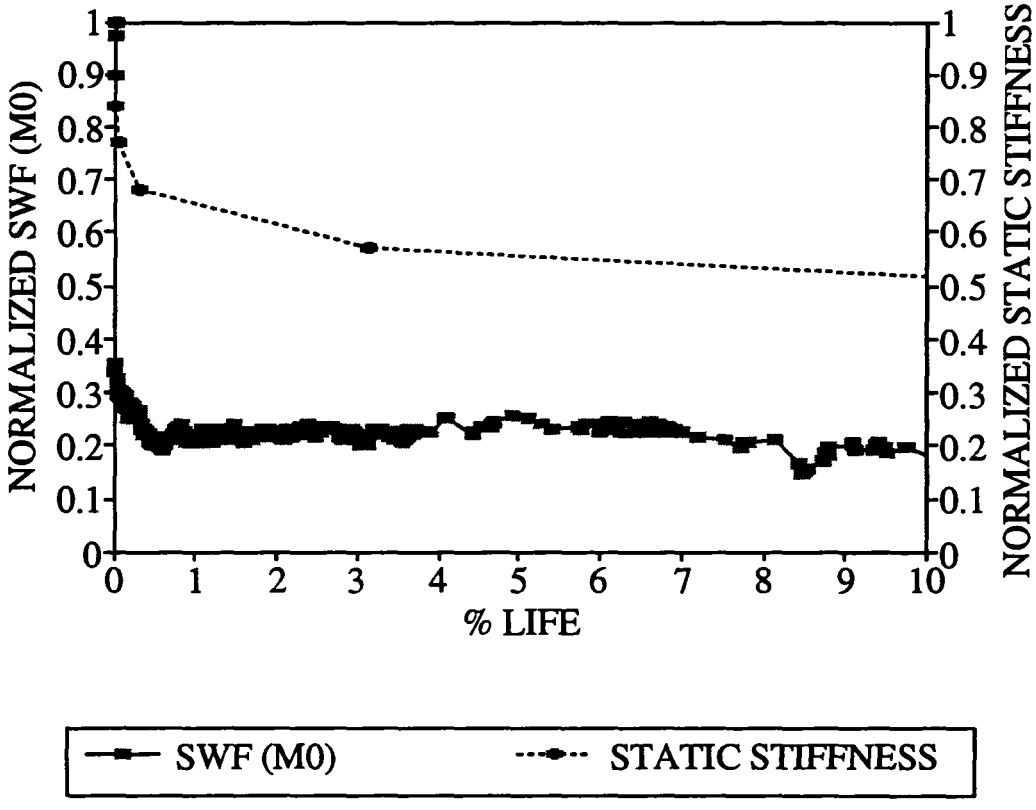

Figure 68. Normalized SWF (M0) and normalized static stiffness vs % life for sample C16, SiC/CAS $[0/90]_{4s}$ (σ_{max} = 60% UTS)

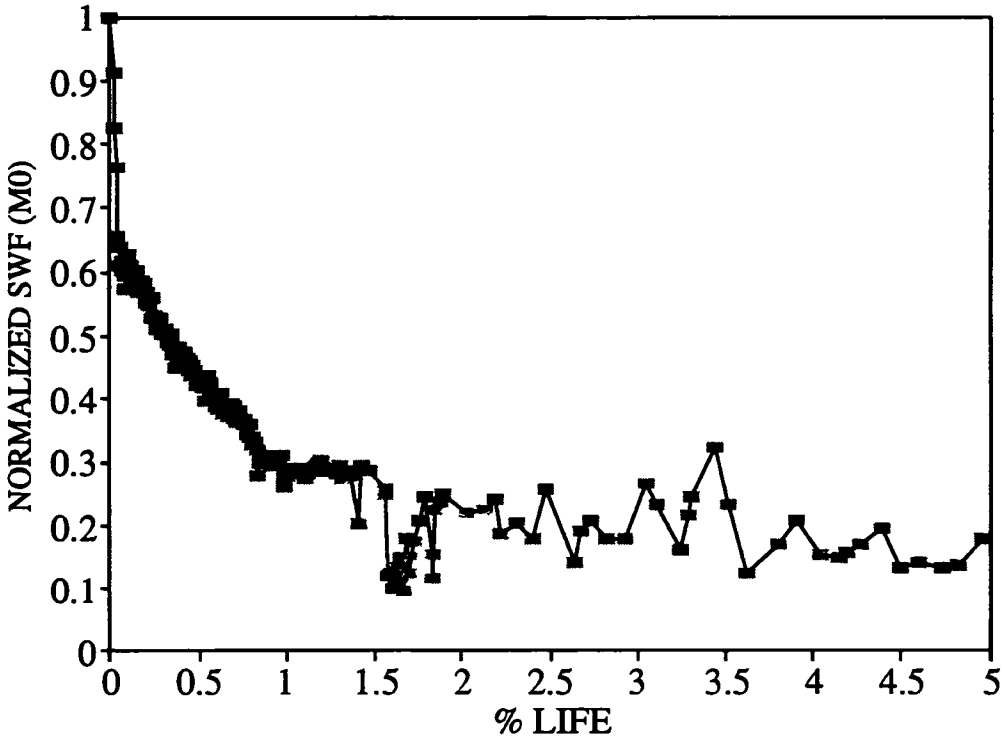

Figure 69. Normalized SWF (M0) vs % life for sample C20, SiC/CAS $[0/90]_{4s}$ (σ_{max} = 60% UTS)

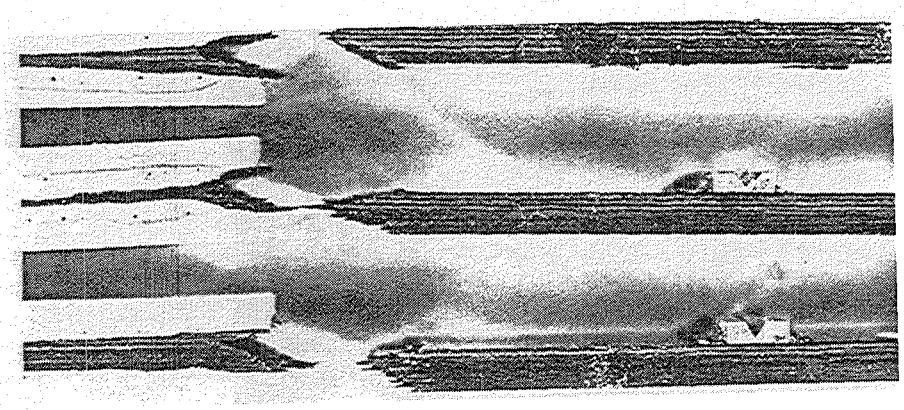

Figure 70. Photograph showing failure locations of samples C11, C16 and C20 SiC/CAS $[0/90]_{4s}$ (σ_{max} = 60% UTS)

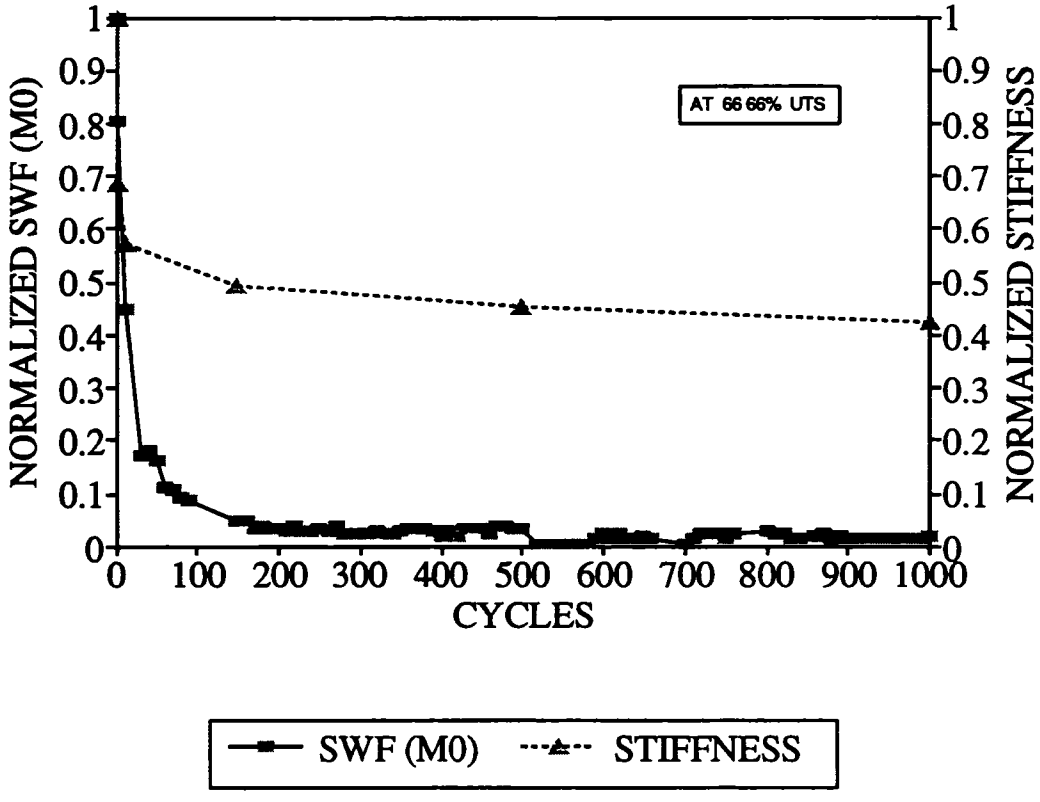

Figure 71. Normalized SWF (M0) and normalized static stiffness vs cycles for sample C3, SiC/CAS $[0/90]_{4s}$ (σ_{max} = 66% UTS)

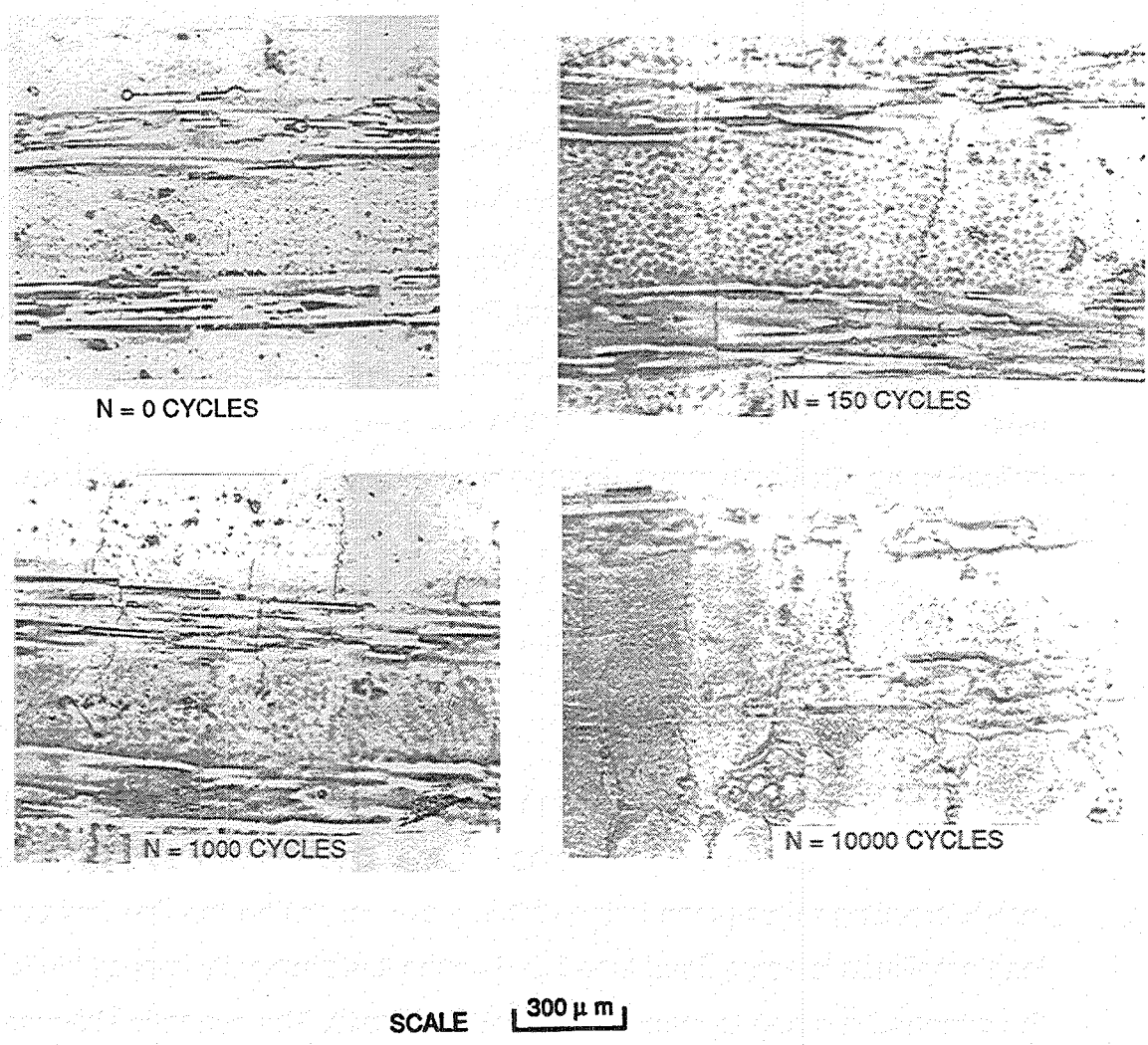

Figure 72. Edge replicas of the damaged surface of sample C3, SiC/CAS $[0/90]_{4s}$ (σ_{max} = 66% UTS)

versus the corresponding number of cycles for sample C3. The damage accumulation with increasing number of cycles is followed by similar reductions in stiffness and SWF values. Figure 72 shows edge replicas taken at the gauge length of sample C3 indicating progressive damage at different points of the fatigue life. Specimen C3 failed at 41,966 cycles. Local delamination between transverse matrix cracks in 90^0 plies is observed and shown in Fig. 73. The failure surface indicated extensive fiber pullout. Maximum damage in sample C3 took place between 0-50 cycles. After 150 cycles the SWF values remain fairly constant indicating no additional major damage occurring until catastrophic failure.

Samples C14 and C15 were fatigued at 65% ultimate tensile strength. The trends of SWF (M0) are similar to low amplitude fatigue samples and are shown in Fig. 74 and Fig. 75 respectively.

Dynamic stiffness was also monitored in all specimens along with edge replication and static stiffness to complement the AU results. Damage in terms of matrix cracking takes place in the first few cycles. During the first few cycles the load amplitude is being fined tuned and hence it is physically impossible to record the changes in strain to measure dynamic stiffness. The dynamic stiffness, along with static stiffness, remains unchanged after the initial first drop in its value for SiC/CAS cross-ply specimens for the loading levels described above. Hence the results of dynamic stiffness are not presented here. In the future, a data acquisition system with continuous peak strain monitoring should be utilized to obtain dynamic stiffness curves.

X-ray radiography done on a few samples produced similar results as also seen in the case of static tests.

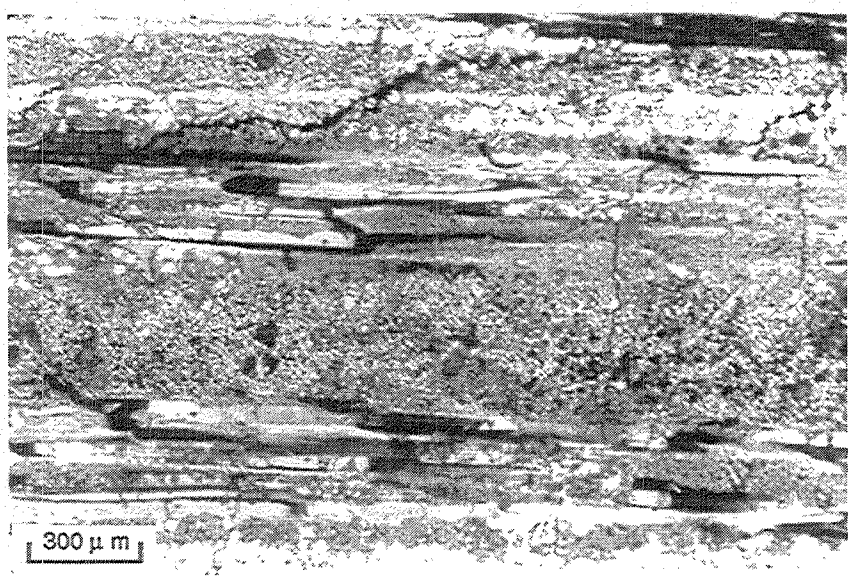

Figure 73. Local delaminations in the 90° plies of sample C3, SiC/CAS $[0/90]_{4s}$ (σ_{max} = 66% UTS)

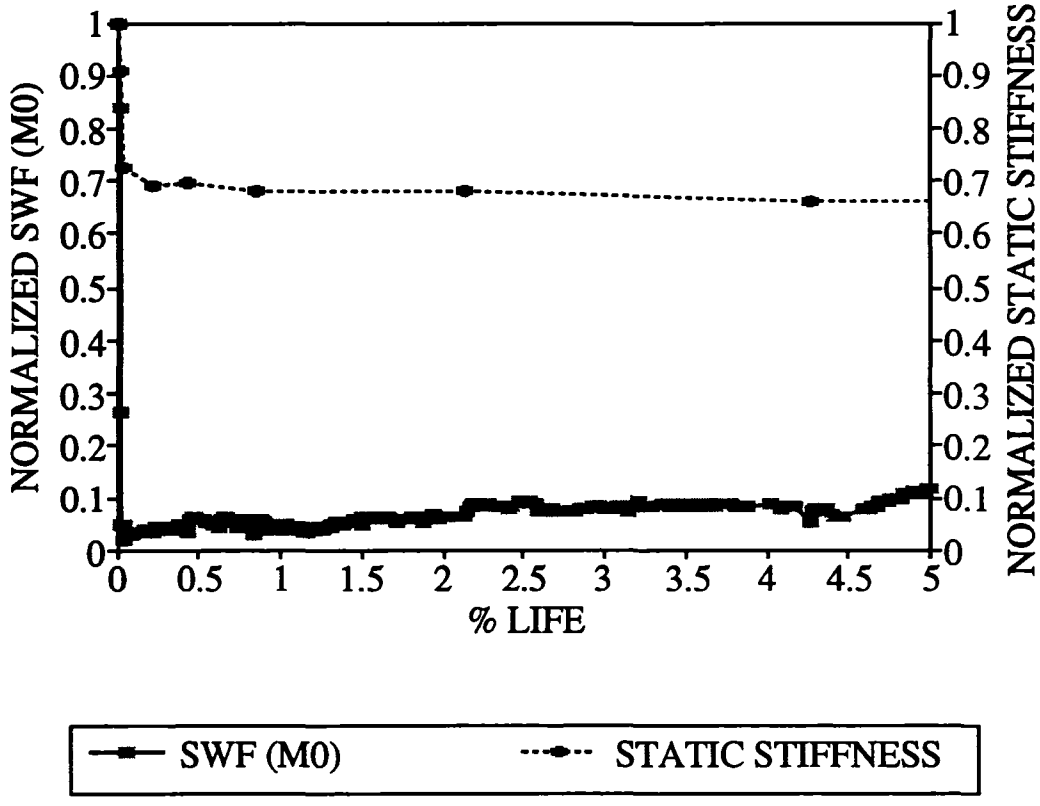

Figure 74. Normalized SWF (M0) and normalized static stiffness vs % life for sample C14, SiC/CAS $[0/90]_{4s}$ (σ_{max} = 65% UTS)

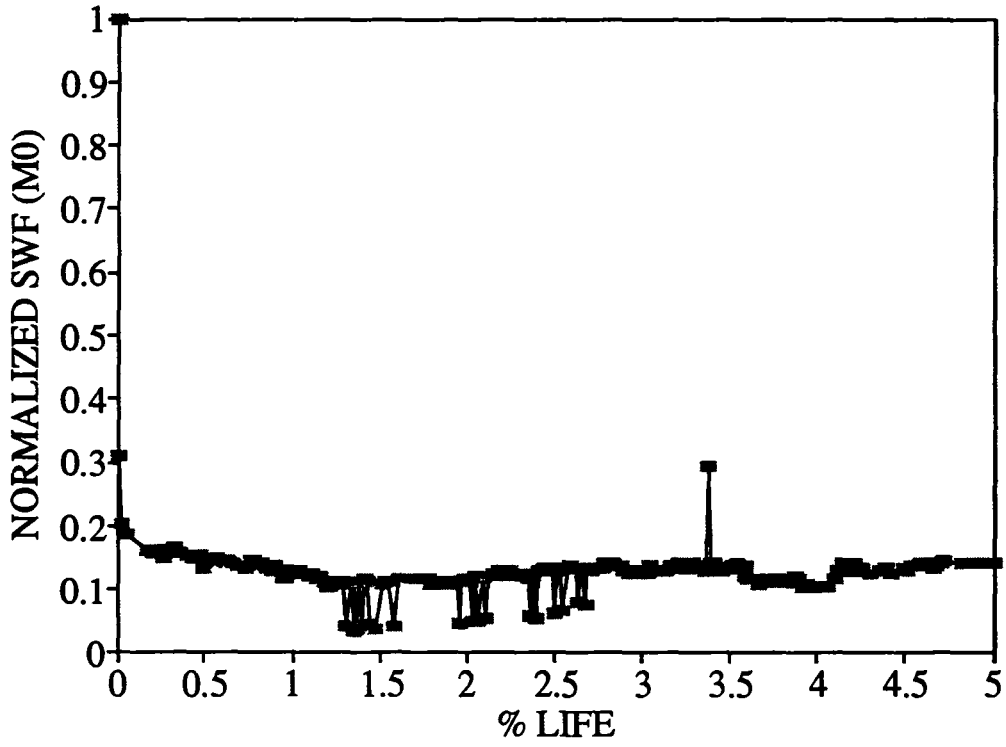

Figure 75. Normalized SWF (M0) vs % life for sample C15, SiC/CAS $[0/90]_{4s}$ (σ_{max} = 65% UTS)

6.4 S-N Curve

The S-N curve stress amplitude vs Log (cycles to failure), was generated using cross-ply SiC/CAS $[0/90]_{4s}$ specimens from the second plate only. Sample C3 and C4 were cut from different plates each having a different density, and hence were not included in the data set. The range of load/stress amplitude was selected from 60% to 90% of ultimate tensile strength. At least three samples were fatigued at the two extremities of this range. The S-N data shown in Fig. 76 are nearly linear. Therefore, a linear regression analysis was performed to obtain the coefficient of variance ($R^2 = 0.988$):

$$\frac{\sigma_a}{\sigma_u} = -0.13919 \log N + 1.387776 \qquad \textbf{(6.1)}$$

Surprisingly, there is not much scatter in the S-N data points obtained during the fatigue tests. In general, S-N curves for polymeric composites show a scatter of data points by an order of magnitude. All the present specimens were fatigued with the same test conditions and were cut from the same panel, perhaps contributing to a well behaved S-N curve for the SiC/CAS cross-ply material system. A knee in the S-N curve for polymeric composites is observed above 60% of ultimate strength and is used to define the endurance limit. A knee is not seen in SiC/CAS for the range of stress amplitudes used here, but this does not rule out the possibility of its existence. It is speculated that a knee exists at stress amplitudes below which matrix cracking does not occur at the very first cycle (45% of ultimate tensile strength). The S-N curve generated here could serve as a guideline for life prediction of a cross-ply SiC/CAS material system.

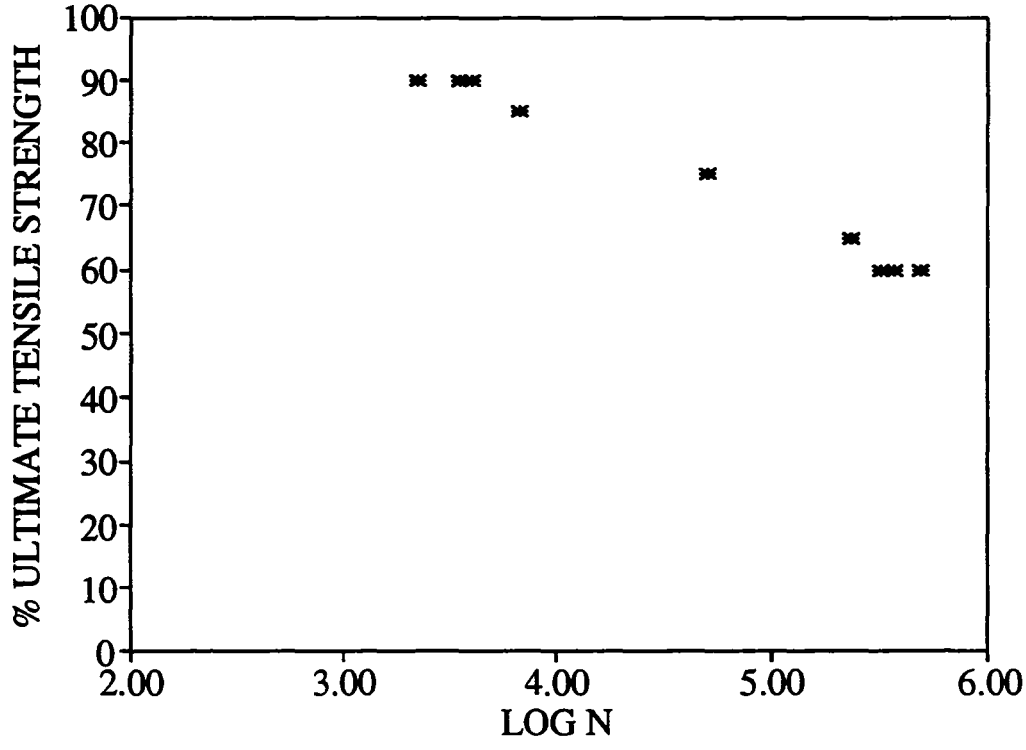

Figure 76. S-N curve for cross-ply SiC/CAS $[0/90]_{4s}$ ceramic composite.

6.5 Failure process during Fatigue

Fatigue damage is defined as cycle dependent degradation of internal integrity [97]. Fatigue damage is primarily concerned with damage events/process which contribute to degradation in stiffness, life or the engineering properties of the material. The changes in mechanical response may not be of the same order as changes in internal integrity. The damage events observed in composite materials include matrix cracking, debonding of fiber/matrix interface, delamination, fiber fracture accompanying these damage modes and final fiber fracture. These damage modes do not occur independently but are inter-linked and hence complex to analyze. The amount of research done on fatigue characteristics of SiC/CAS ceramic composites has been limited till now. Researchers [108-110] have shown a similarity between failure/damage mechanisms occurring during static and fatigue tests for the SiC/CAS material system. Fatigue characteristics at elevated temperature are different generally than room temperature fatigue tests [110]. For the present work, fatigue tests were run at room temperature and the damage process described here is for room temperature.

The typical damage modes during fatigue consist of (a) matrix cracking and accompanying fiber breaks at or near the matrix crack planes, (b) the matrix crack coupling, interfacial debonding and accompanying fiber breaks, (c) onset of delamination and accompanying fiber breaks, (d) local delamination growth with perhaps localized fiber breaks, and (e) final failure of the laminate caused by extensive fiber breaks. Random fiber breaks are also observed for statistically weak fibers.

The failure/damage process in a ceramic composite consists of initiation and growth of several different damage modes and the complex interaction

between them. The damage process in un-notched SiC/CAS cross-ply $[0/90]_{4s}$ ceramic composite at the load levels used here can be considered in three stages. Stage 1 occurs during the first 8-10% of life during which damage develops at a very rapid rate. The damage mode that occurs during this stage is matrix cracking in the 90^0 and 0^0 plies with saturation by the end of the first stage and accompanied by a few fiber breaks. The SWF (M0) values also drop by 70% - 90% during this stage and a similar drop of 50% is seen in the static stiffness of the laminate. The maximum stress level for low load amplitude tests used here is higher than the stress level for the onset of matrix cracking in the 90^0 and 0^0 plies. Hence, matrix cracking occurs in all plies during the first cycle and saturates during the first 10-20 cycles. The edge replicas taken at different cycles show the increase in crack density in the first 10 cycles. In ceramic composites the stiffness of the matrix is comparable to the fiber, unlike polymeric based composites (PMC) for which the fibers are considerably stiffer than the matrix. The reduction in static stiffness is around 50% due to matrix cracking compared to only 10% in polymeric composites.

The SWF values are reduced by a slightly higher amount at higher load amplitudes compared to low load amplitudes. The rate of decrease of SWF values is also dependent on the stress amplitude. The higher the stress amplitude, the faster is the saturation of matrix cracks in all plies, resulting in a steeper drop of SWF values. Quasi-static tests show the relation between SWF values and the matrix crack density with increasing stress levels. Since the range of stress amplitudes selected are higher than the onset stress level for matrix cracks, the difference in the % SWF drop at a fixed % of life during the first stage between the high and the low load amplitude is small.

A characteristic damage state (CDS) is reached at the end of the first stage

[112]. The pattern of crack spacing is similar to that for quasi-static tests. The saturation of matrix cracks at the end of the first stage is said to be a characteristic damage state (CDS) as the saturation spacing is independent of the load history. CDS is a laminate property defined by the constituent ply properties, the lay-up and the thickness of each ply, and the residual stresses. This matrix crack saturation and the corresponding crack spacing is a 'stable damage state' defined for each specific laminate. CDS can be used as the starting point of description of fatigue damage.

The second stage corresponds to the next 70% - 80% of the life during which time damage continues to grow at a very slow rate. The plateau observed in the normalized SWF (M0) and normalized static stiffness curves correspond to this stage. The various damage modes initiating and growing in the second stage have little effect on the laminate stiffness. The matrix cracks interconnect with further fiber/matrix debonding in the 0^0 plies and initiation of local delamination occurs in this stage of the damage process. Local delamination has been observed only during fatigue loading at low and medium stress amplitudes. This does not rule out the possibility of slight delamination occurring at high stress amplitudes that was undetected, although delamination was not observed during static tests. Local delaminations as shown in Fig. 61, are initiated by the matrix cracks and occur preferentially at positions closer to the free edge surfaces as there is no constraint there to the out of plane motion.

The third stage corresponds to the last 10% of life and consists of an accelerated damage process due to the localization of fiber breaks causing dynamic fiber fractures as shown in Fig. 67. The damage mechanisms in this region are dominated by the failure mechanisms of the fibers and their statistical behavior. The laminate stiffness degrades to such an extent in this region that the

laminate cannot support the applied loads.

Reifsnider [93-94] has proposed the critical element model to characterize the damage process and predict the strength of composite laminates. Critical elements are defined by the final failure mode of the laminate. Critical elements are those elements whose failure defines the failure of the laminate. Sub-critical elements are defined by the damage modes that occur during fatigue. Failure of these sub-critical elements changes the mechanics of local stress and its redistribution but does not cause the final failure of the laminate. The strength of the laminate is determined by the state of stress and the state of the material. The state of the material is controlled by degradation of the critical elements or the properties of the material of the critical elements.

The critical element in a tensile failure of a fiber controlled cross-ply ceramic composite subjected to fatigue is the 0^0 plies or the fibers in the 0^0 plies. Failure of these fibers by local unstable growth of a region of fiber fracture is the final event in the damage process. The sub-critical elements are:

1. 90^0 plies matrix cracking and fiber/matrix debonding
2. 0^0 plies matrix cracking, fiber/matrix debonding and limited fiber fracture in the matrix crack plane
3. Local delaminations and limited local fiber fracture

The initiation of damage modes and their propagation can be monitored continuously by real time AU parameters and can serve as input to the critical element model. The local state of stress is altered by the failure of the corresponding critical elements and accordingly the final failure of the critical element (breaking fibers in the 0^0 plies) can be predicted by this model. The stiffness of the laminate can also be extrapolated by the SWF (M0) vs cycles curve

for a given laminate and fatigue stress amplitude. Matrix cracks for the range of stress amplitude used in these tests occur in the first few cycles. The stress amplitude needs to be lowered to obtain a wider range over which matrix cracks occur so as to have a better extrapolation for stiffness from SWF values over larger data sets. The extrapolated stiffness reduction curve could also serve as input to the critical element model with the help of AU data.

6.6 Summary

The feasibility of the real-time AU technique for monitoring damage under fatigue loading was accomplished with success. The SWF (M0) measures the damage state at each cycle continuously without interrupting the fatigue test. The real-time AU set-up was validated by performing controlled experiments to verify the assumptions that AU changes resulted predominantly from damage progression. The SWF values remained constant as no damage took place during low stress amplitude (R = 0.1, f = 10 Hz) fatigue tests performed on mild steel and SiC/CAS ceramic composite material saturated with matrix cracks.

An S-N curve for cross-ply $[0/90]_{4s}$ ceramic composite was generated. The failure characteristics of cross-ply SiC/CAS specimens loaded in fatigue were similar to the static tests except for delaminations which occurred at low and medium stress amplitude fatigue tests. The damage progression was documented by monitoring static stiffness, dynamic stiffness and edge replication to complement the AU results. It has been observed that reduction in SWF values during the first stage of the damage process is higher in the interrupted fatigue tests compared to the uninterrupted tests. It is believed that the dynamics of the damage mechanisms is altered by the interruption of these fatigue tests. The real-

time AU technique developed here is a continuous damage monitoring system without interruptions and hence has a distinct advantage over the conventional NDE techniques for monitoring damage. The critical element model discussed in this chapter can be applied to predict the strength of the laminate subjected to fatigue with the help of AU parameters. The understanding of damage and its effect on residual strength and life is essential to the development of the damage tolerance methodologies for certification of composite structures and for developing and quantifying new materials [111]. Damage monitoring by real time AU as shown here can be used as a tool to provide an insight into the damage mechanisms of these new materials and thereby help in the study of their failure mechanisms.

7. Conclusions and Future Recommendations

A summary of the research conducted and the conclusions drawn are presented in this chapter in a succinct form along with future recommendations. This chapter is divided into sub-sections pertaining to the results and conclusions of:

(a) Development of real time AU, (b) Quasi-static tests of ceramic composites, (c) AUSSR modeling and (d) fatigue tests on cross-ply SiC/CAS ceramic composites corresponding to chapters 4, 5 and 6. Future work is outlined at the end of this chapter based on the observations and conclusions of the present research.

7.1 Development of real-time AU technique

- The feasibility of the real-time AU technique to assess and monitor the damage state in SiC/CAS ceramic composites under dynamic loads, (quasi-static and fatigue loading) was shown. It was found that the real-time AU technique can monitor damage progression in ceramic composites subjected to quasi-static and fatigue loading without interrupting the test. The dynamics of damage mechanisms are altered by interrupting the test for damage documentation by conventional NDE techniques as shown in a previous chapter. Hence, the development of the real-time AU technique can be considered a significant contribution to the NDE field in terms of quantifying damage continuously without stopping the test.

7.2 Quasi-static tests

- Real-time AU was used for monitoring damage progression in unidirectional, cross-ply SiC/CAS and quasi-isotropic SiC/MAS ceramic composites subjected to quasi-static loads. The real-time AU technique detected the onset and saturation stress levels for matrix cracking. The AU results were corroborated by in-situ optical microscope video recordings.

- The AU parameter is a good measure of initial integrity of the material studied here. The initial SWF (M0) shows a linear correlation with the ultimate strength of unidirectional SiC/CAS ceramic composite. Higher the value of initial SWF (M0), higher is the ultimate strength of unidirectional SiC/CAS ceramic composite.

- Real-time AU was used to study the failure mechanisms of ceramic composites subjected to quasi-static loads.

7.2.1 Failure process in $[0_8]_s$ SiC/CAS ceramic composite under quasi-static loads

- The first damage mode observed is the development of parallel transverse matrix cracks perpendicular to the load axis over a stress range. The onset of large scale matrix cracks (around 180 MPa) and the saturation stress level (275 MPa) is obtained from the AU parameter. The Budiansky, Hutchinson and Evans model predicts a higher critical cracking stress (207

MPa) due to the inherent assumption of steady state cracking which implies matrix cracking takes place at a single critical stress unlike real materials where it occurs over a stress range.

- The matrix cracking is accompanied by a few fiber breaks due to the additional loading of fibers at the matrix crack plane.

- The non-linear portion of the stress-strain curve is believed to be a combination of the effects of progressive matrix cracking over the stress range, fiber debonding and fiber slipping, and an accompanying few fiber breaks during matrix cracking.

- The onset of large scale matrix cracking slightly varies due to differences in flaw distribution in the matrix material. The characteristic damage state (CDS) is obtained at the saturation of matrix cracking (275 MPa), is a laminate property, and is independent of prior loading. The majority of the load is shared by the fibers after saturation of matrix cracks.

- The average ultimate tensile strength of SiC/CAS $[0_8]_s$ ceramic composite obtained from static tests is 400 MPa. The analytical model of Curtin's over-predicts the ultimate strength (525 MPa). The failed specimens show extensive fiber pull-out.

- The ultimate strength of a heat treated unidirectional specimen is reduced by 50% due to oxidative embrittlement of the interphase. The fiber/matrix bonding becomes stronger with oxidation, resulting in a brittle failure with negligible fiber pull-out.

7.2.2 Failure process in $[0/90]_{4s}$ SiC/CAS ceramic composite under quasi-static loads

The failure process in a cross-ply laminate is very similar to that in a unidirectional laminate apart from the initial degradation of the 90^0 plies.The sequence of damage is as follows:

- Initial degradation of 90^0 plies caused by matrix cracking in these plies.

- The onset (95 MPa) and saturation of matrix cracking (150 MPa) in the 0^0 plies with a few accompanying fiber breaks. The nominal stress levels at onset and saturation are approximately half the corresponding stress levels for unidirectional specimens as there are only half the number of 0^0 plies. The majority of the load is being carried by the fibers in the 0^0 plies after the saturation of matrix cracks.

- The average ultimate tensile strength of $[0/90]_{4s}$ SiC/CAS ceramic composites obtained from the static tests was 163 MPa. The ultimate failure was caused by localized extensive fiber breaks. Extensive fiber pull-out was observed at failure.

- Failure in the heat treated specimen was brittle in nature and was caused by the initiation and subsequent growth of matrix cracks in the 90^0 plies. The failure surface showed negligible fiber pull-out due to oxidative embrittlement of the interphase. The ultimate strength was reduced by 40% - 50% due to the heat treatment.

Real-time AU monitored damage in quasi-isotropic SiC/MAS specimens subjected to quasi-static loads. The number of specimens tested was not sufficient to make conclusive remarks about the failure process in these specimens.

7.3 AUSSR model

The AUSSR model predicts the strain response to increasing stress levels by incorporating the damage modes and their effects upon the global strain response of a laminate with the help of real-time AU data and classical laminated plate theory.

- The ply properties are varied according to the real-time AU data using Weibull parameters to vary E_m and G_m of the matrix to take into account the occurrence of matrix cracks over a stress range.

- The Weibull shape parameter, α, denotes the spread of the range at which matrix cracking occurs and could be used as a quality control tool.

- The Weibull location parameter, β = 235 MPa, for unidirectional SiC/CAS ceramic composite is nearly the critical cracking stress level (σ_{cr} = 207 MPa) calculated with Budiansky, Hutchinson and Evans model.

- The AUSSR-WZ-WB model incorporates fiber breaks during matrix cracking and the additional strains caused by the fiber breaks.

- The modified AUSSR model incorporates the fiber breaks during matrix cracking by altering the effective fiber volume fraction and is an improvement on the previous models.

- The AUSSR model for cross-ply SiC/CAS ceramic composite shows two non-linear zones, one each for matrix cracking in the 90^0 plies and 0^0 plies as observed in the experimental curve.

The prediction of these models approximates the corresponding typical experimental curve. The basic damage mechanisms during quasi-static tests are interpreted with the help of real-time AU data and supported by AUSSR models.

- The Weibull parameters, α and β, can be used to predict the onset of large scale matrix cracking in ceramic composites. The onset of matrix cracking should be used as the design stress for thermo-structural applications instead of the critical cracking stress obtained from the Budiansky Hutchinson and Evans model.

7.4 Fatigue tests

- The verification of the real-time AU set-up to be insensitive to changes other than damage during fatigue was accomplished with success.

- The real-time AU technique monitors damage progression during fatigue. Reduction in stiffness correlates with the change in the AU parameter at different stages of fatigue life, and these results were complemented and verified by edge replica photographs.

- Room temperature S-N curve was generated for un-notched SiC/CAS $[0/90]_{4s}$ ceramic composite.

- Real-time AU was used to study the failure mechanisms of ceramic composites subjected to fatigue loads.

- The failure characteristics of a cross-ply specimen subjected to fatigue loads are similar to the static tests, except for local delamination. The specimens were subjected to fatigue with stress amplitudes varying from 60% - 90% of UTS. The stress amplitude of 60% UTS is higher than the stress level for onset of matrix cracking and hence matrix cracking, occurs in the first few cycles for all specimens tested here.

The damage process in un-notched SiC/CAS $[0/90]_{4s}$ ceramic composite can be considered in three stages:

- Stage 1: onset and saturation of matrix cracking in 90^0 plies and 0^0 plies in the first 8% - 10% of life. Edge replicas of the damaged surface document the increasing crack density over this period. The characteristic damage state (CDS) is reached at the end of the first stage.

- Stage 2: corresponds to next 70% - 80% of the life. Delamination has been observed during fatigue at low stress amplitude (60% - 70%) and medium stress amplitude (70% - 80%).

- Stage 3: consists of accelerated damage process due to localization of fiber breaks causing final dynamic fracture. The failure mechanism at this stage is dominated by the failure mechanism of the fibers and its statistical behavior. Extensive fiber pull-out is seen at low, medium and high stress amplitude fatigue tests.

The ability of real-time AU NDE to study the failure mechanisms of ceramic composites has been demonstrated. Monitoring the onset of each damage mode and its progression under quasi-static ramp loading in tension and fatigue loading adds to our overall understanding of the failure mechanisms of ceramic composites.

7.5 Recommendations for future work

- Apply the critical element model to predict the life of a laminate subjected to fatigue with the help of AU damage progression curves. The fibers in the 0^0 plies are the critical elements controlling the strength of the laminate. The sub-critical elements are defined as the matrix of 90^0 plies and 0^0 plies.

- Extrapolate stiffness degradation curves from AU damage progression curves for fatigue loading. The relationship between the slopes of stiffness degradation curve and the AU damage progression curve at all three stages of damage progression can be obtained for a given stress amplitude.

- Alter the Modified AUSSR model to incorporate additional strains caused by the fiber breaks. These strains can be added to the matrix cracking model as and when the fiber breaks occur instead of assuming it to occur at the saturation of matrix cracks, with the help of AU data.

- Modify the AU analysis code to segregate the AE signals from the AU signals based on the prior knowledge of the characteristics of AE signals from each damage modes. Frequency domain analysis of AU signals could

be done in real-time during the test with the help of better computing capability.

- Study the effect of stress on AU signals by running controlled experiments and incorporate it into the AU analysis.

- Develop an understanding of the mechanics of acousto-ultrasonic technique by studying the wave propagation modes generated by AU signals.

- Study and design real-time AU tests at high temperatures with the help of laser based generation and detection of stress waves. Ceramic composites are utilized for high temperature applications and hence mechanical characterization at elevated temperature is important. The present commercially available AU transducers have a maximum operating temperature of 600^0 C. Real-time AU testing with the help of laser instrumentation might be used as a NDE tool for continuous monitoring of damage at high temperature without stopping the test.

References

1. Munz D., Rosenfelder O., Goebbels K. and Reiter H.," Assessment of flaws in ceramic materials on the basis of non-destructive evaluation", Fracture Mechanics of Ceramics, vol. 7, Publ by Plenum Press, New York, NY, USA pp. 265-283.

2. Klima Stanley J. and Vary Alex," Nde of structural ceramics", NASA Tech Memo 87186, 1986.

3. Nongaillard B., Logette P., Rouvaen J. M., Saisse H. and Fevrier H.," Acoustic microscopy: a tool for non-destructive evaluation of ceramics", NDT International, vol. 19, no. 2, Apr 1986, pp. 77-82.

4. Fahr A., Johar S., Murthy M. K. and Sturrock W. R., " Surface acoustic wave studies of surface cracks in ceramics", Review of Progress in Quantitative Nondestructive Evaluation, vol. 3A, Publ by Plenum Press, New York, NY, USA & London, England, pp. 239-249.

5. Cielo P., Maldague X., Johar S. and Lauzon B.," Some laser-based techniques for the characterization of sintered ceramics", Materials Evaluation, vol. 44, no. 6, May 1986, pp. 770-774.

6. Vary Alex, Generazio Edward R., Roth Don J. and Baaklini George,"Ultrasonic nde of structural ceramics for power and propulsion systems", NASA Tech Memo 100147, 1987.

7. Gundtoft H. E., Borum K. K. and Jacobsen F.,"Precision scanning with ultrasound with examples from measurements of single porosities in ceramics", NDT International vol. 21, no. 6, Dec 1988.

8. No Kwangsoo and McClelland John F.,"Thermal-wave imaging of ceramic/metal boundaries and of voids in low and high thermal conductivity ceramics", Review of Progress in Quantitative Nondestructive Evaluation, vol. 7A, 1988 pp. 263-272.

9. Generazio, E. R., Roth, D. J. and Baaklini, G. Y., "Acoustic imaging of subtle porosity variations in ceramics", Materials Evaluation, vol. 46, no. 10, Sep 1988, pp. 1338-1343.

10. Roberts, R. A.,"Dry-contact coupling technique for ultrasonic nondestructive evaluation of green-state ceramics", Materials Evaluation vol. 46, no. 6, May 1988 pp. 758-766.

11. Opara, U.,"High frequency ultrasonic equipment for detection of submillimeter flaws", Review of Progress in Quantitative Nondestructive Evaluation, vol. 5A, Publ by Plenum Press, New York, NY, USA pp. 811-816.

12. Patel Narendra D., van den Andel Jan and Nicholson Patrick S.,"High frequency transducer development for ultrasonic tests on ceramic components", Review of Progress in Quantitative Nondestructive Evaluation, vol. 5A, Publ by Plenum Press, New York, NY, USA pp. 605-613.

13. Rose Douglas N., Bryk Darryl C., Jackson William, Chaika Milt, Schram Glen, Quay Greg, Thomas Robert L., Favro Lawrence D. and Kuo Pao-Kuang,"Characterization of advanced ceramics by thermal wave imaging", Ceramic Engineering and Science Proceedings, vol. 8, no. 7-8, Jul-Aug, 1987, pp. 513-524.

14. Singh J. P., Roberts R. A., Vaitekunas J. J., Ellingson W. A.," Failure prediction of hot-pressed si//3n//4 ceramics by nde", American Society of Mechanical Engineers (Paper) Publ by ASME, New York, NY, USA 87-GT-7.

15. Slavin Michael J. and Gruber Jeffrey J.," Ultrasonic characterization of ceramics", American Society of Mechanical Engineers (Paper) Publ by ASME, New York, NY, USA 87-GT-1.

17. Klima Stanley J., Baaklini George Y. and Abel Phillip B.," Nondestructive evaluation of structural ceramics", NASA Tech Memo 88978, 1986.

18. Ellingson W. A. and Koenigsberg W. D., "Evaluation of engineering ceramics by gamma-ray computed tomography", Ceramic Engineering and Science Proceedings, vol. 7, no. 7-8, Jul-Aug 1986, pp. 772-783.

19. Klima S. J., " Nde of advanced ceramics", Materials Evaluation, vol. 44, no. 5, April 1986, pp. 571-576.

20. Bimbaum G. and White G. S.," Laser techniques in nde", Research Techniques in Nondestructive Testing, vol. 7, Publ by Academic Press, London, England and New York, NY, USA, 1984, pp. 259-365.

21. Berger Harold and Kupperman Davis S.," Microradiography to characterize structural ceramics", Materials Evaluation, vol. 43, no. 2, Feb 1985, pp. 201-205.

22. Tien J. J. W., Khuri-Yakub B. T., Kino G. S., Marshall D. B. and Evans A. G.," Surface acoustic wave measurements of surface cracks in ceramics", Journal of Nondestructive Evaluation, vol. 2, no. 3-4, Dec 1981, pp. 219-229.

23. Klıma S. J., Watson G. K., Herbell T. P. and Moore T. J.," Ultrasonic velocity for estimating density of structural ceramics", NASA Tech Memo 82765, 1982.

24. Round R., Bridge B. and Green A.," Appraisal of the use of low frequency ultrasound in the non-destructive evaluation of filament wound ceramics", Journal of Materials Science Letters, vol. 7, no. 7, July 1988, pp. 748-752.

25. Roth Don J. and Baaklini George Y.," Reliability of scanning laser acoustic microscopy for detecting internal voids in structural ceramics", Ceramic Engineering and Science Proceedings, vol. 7, no. 7-8, Jul-Aug 1986, pp. 771.

26. Roth D. J., Klima S. J., Kiser J. D. and Baaklini G. Y.," Reliability of void detection in structural ceramics by use of scanning laser acoustic microscopy", Materials Evaluation, vol. 44, no. 6, May 1986, pp. 762-769.

27. Baaklini George Y.," NDE reliability and process control for structural ceramics", American Society of Mechanical Engineers (Paper) Publ by ASME, New York, NY, USA, 87-GT-8.

28. Marshall David B. and Ritter John E.," Reliabılıty of advanced structural ceramics and ceramic matrıx composites - a review", American Ceramic Society Bulletin vol. 66, no. 2, Feb 1987, pp. 309-317.

29. Vary A., "Acousto-ultrasonic characterization of fiber reinforced composites", Materials Evaluation Vol. 40, pp. 650-662, 1982.

30. Vary A., and Bowles K.J.,"An ultrasonic-acoustic technique for non-destructive evaluation of fiber composıte quality,"Polymer Engineering and Science, Vol. 19, pp. 373-376, 1979.

31. Vary A., and Lark R.F.,"Correlation of fiber composite tensile strength with the ultrasonic stress wave factor," Journal of Testing and Evaluation, Vol. 7, pp. 185-191, 1979.

32. Govada A.K., Duke J.C. Jr. and Henneke E.G.II, "A study of stress wave factor technique for the characterization of composite materials," NASA Contractor Report-174870, 1985.

33. Duke J.C. Jr., Henneke E.G.II and Stinchcomb W.W., "Ultrasonic stress characterizatıon of composıte materials," NASA Contractor Report 3976, May 1986.

34. Sarrafzadeh-khoee A., Kiernan M.T., Duke J.C. Jr. and Henneke E.G.II, "A study of the stress wave factor technique for the non-destructive evaluatıon of composite materials," NASA Contractor Report 4002, Jul. 1986.

35. Duke J.C. Jr., Henneke E.G. II, Kiernan M.T. and Grosskopf P.P., "A study of stress wave factor technique for evaluation of composite materials," NASA Contractor Report 4195, Jan. 1989.

36. Kiernan M.T., "A physical model for the acousto-ultrasonic method," Doctoral Dissertation, College of Engineering, Virginia Polytechnic Institute and State University, Blacksburg, VA, U.S.A., Aug. 1989.

37. Kiernan M. T. and Duke J.C. Jr., " Acousto ultrasonics as a monitor of material anisotropy", Materials Evaluation, vol. 46, no. 8, Aug. 1988, pp. 1105-1113.

38. Kiernan M. T. and Duke J.C. Jr., " PC analysis of an acousto ultrasonic signal", Materials Evaluation, vol. 46, no. 10, Oct. 1988, pp. 1344-1352.

39. Kiernan M. T. and Duke J.C. Jr., " A physical model for the acousto ultrasonic method", NASA CR 185294, 1990.

40. Grosskopf P.P. and Duke J.C. Jr., " Mechanical Behavior of a ceramic matrix composite", NASA CR 187072, Feb. 1991.

41. Sunderesan M. J., Henneke E. G. II and Brosey W.D., " Acousto-ultrasonic investigation of filament wound spherical pressure vessels", Materials Evaluation, May 1991, pp. 601-606.

42. Stiffler R.C., "Wave propagation in composite plates," Doctoral Dissertation, College of Engineering, Virginia Polytechnic Institute and State University, Blacksburg,VA U.S.A., Nov. 1986.

43. Henneke E.G.II, Duke J.C. Jr. and Tiwari Anil, "NDT methods to assess the integrity and quality of an adhesively bonded sheet metal," Interim Project Report, Ford Motor Company, 1989.

44. Tiwari Anil, "A Feasibility study of the acousto-ultrasonic technique to assure the quality of adhesively bonded sheet metal," Master's Thesis, College of Engineering, Virginia Polytechnic Institute and State University, Blacksburg, VA, U.S.A., Feb. 1990.

45. Tiwari Anil, Henneke E.G.II and Duke J.C. Jr., "Acousto-ultrasonic (AU) Technique for Assuring Adhesive Bond Quality," Journal of Adhesion, Vol. 34, 1991, pp. 1-15.

46. Tiwari A., Henneke E. G.II, Vary A. and Chulya A., " In-situ Acousto-ultrasonic Technique to Monitor Damage in Ceramic Composites," Fifth Annual HITEMP conference proceedings, Cleveland, Ohio, Oct. 27-28, 1992.

47. Tiwari Anil and Henneke E. G. II, " In-situ Acousto-ultrasonic Technique to Monitor Damage in SiC/CAS Ceramic Composites," ASTM conference, Nov. 16-17, 1992, Miami, Florida, submitted for STP publication, ASTM.

48. Tiwari A. and Henneke E. G.II, " Development of real time monitoring of damage by Acousto-ultrasonic technique to study the failure mechanisms in SiC/CAS Ceramic Composites," Proceedings of Nondestructive Characterization of Materials VI, ed. Robert E. Green Jr., Presented at Oahu, Hawaii, June 7-11, 1993.

49. Tiwari A. and Henneke E. G. II, " Real time Acousto-ultrasonic NDE technique for monitoring damage in SiC/CAS Ceramic Composites," Proceedings of second world conference on acousto-ultrasonics, June 24-25, 1993, Atlanta, Georgia.

50. Acousto-Ultrasonics--Theory and Applications, J.C.Duke Jr., Ed. (Plenum Press, New York, 1988).

51. Srivastava V.K. and Ravi Prakash, " Prediction of material property parameter of FRP composites using ultrasonic and acousto ultrasonic techniques", Composite structures, Vol. 8, 1987, pp. 311-321.

52. De Asok, Phani K. K. and Kumar S.," Acousto-ultrasonic study on glass-ceramics in the system MgO-Al//2O//3-SiO//2", Journal of Materials Science Letters, vol. 6, no. 1, Jan 1987, pp. 17-19.

53. Kautz H. E. and Bhatt R. T.," Ultrasonic velocity technique for monitoring property changes in fiber reinforced ceramic matrix composites", NASA TM 103806, 1991.

54. Kautz H.E., " Ray propagation path analysis of acousto-ultrasonic signals in composites", NASA TM 100148, 1987.

55. Kautz H.E., " Acousto ultrasonic verification of the strength of filament wound composite materials", NASA TM 88827, 1986.

56. Kautz H.E. and Lerch Brad A., " A preliminary investigation of acousto ultrasonic NDE of metal matrix composite test specimens", NASA TM 104339, 1991.

57. Kautz H.E. and Lerch Brad A., " Preliminary investigation of acousto ultrasonic NDE of metal matrix composite specimens", Materials Evaluation, May 1991, pp. 607-612.

58. Kautz H.E., " Acousto-ultrasonics for high temperature composites", Proceedings of the fourth annual HITEMP review, Cleveland, OH, Oct. 29-30, 1991.

59. Kautz H.E., " Detecting lamb waves with broad band acousto ultrasonic signals in composite structures", NASA TM 105557, Mar 1992.

60. Vary Alex, " NDE of HITEMP composites - status and needs", Proceedings of the fifth annual HITEMP review- Advance high temperature engine technology program, vol III, NASA conference publication 10104, 1992, pp. 75.1-75.14.

61. Henrique L.M. dos Reis, " Acousto ultrasonic evaluation of ceramic matrix composite materials", NASA TM 187073, Feb 1991.

62. Fahr A., Lee S., Tanary S., and Haddad Y., "Estimation of strength in adhesively bonded steel specimens by acousto-ultrasonic technique," Materials Evaluation, Vol. 47, pp. 233-240, 1989.

63. Vary Alex and Lark R.F., " Correlation of fiber composite tensile strength with ultrasonic stress wave factor", NASA TM 77846, April 1978.

64. Vary Alex and Bowles K. J., " Ultrasonic evaluation of the strength of unidirectional Gr./polyimide composites", NASA TM 73646.

65. Tang Bruce, Henneke E.G. II and Stiffler R.C., " Low frequency flexural wave propagation in laminated composite plates", Acousto-ultrasonics : Theory and Applications, Ed. John C. Duke Jr., Plenum publishing corporation,1988, pp. 45-65.

66. Tang Bruce and Henneke E. G. II, " Lamb wave characterization of composite materials", Nondestructive testing communications, vol. 3, 1988, pp. 155-168.

67. Tang Bruce and Henneke E. G. II, " Lamb wave velocity measurement for evaluation of composite plates", Nondestructive testing communications, vol. 4, 1989, pp.109-120.

68. Tang Bruce and Henneke E. G. II, " Lamb wave monitoring of axial stiffness reduction of laminated composite plates", Materials Evaluation, Vol. 47, no. 8, 1989, pp. 928-934.

69. Tang Bruce and Henneke E. G. II, " Long wavelength approximation for lamb wave characterization of composite laminates", Research in Nondestructive Evaluation, vol. 1., no. 1, Aug 1989, pp. 51-64.

70. Bernard O.C. Aduda and Rawlings R.D., " Acousto ultrasonic testing of inorganic composites", Advanced Structural Inorganic Composites, Ed. P. Vincenzini, Elsevier Science Publishers, 1991, pp. 441-450.

71. Hashemi Nayeb H., Cohen M.D., Zotos J. and Poormand R., " Nondestructive evaluation of Gr/Ep composite materials subjected to combined fatigue and impacts", Proceedings of International Conference and exposition on fatigue, Corrosion cracking, Fracture mechanics, Failure analysis, ASM, Dec. 2-6, 1985.

72. Truell R. and Hikata A., " Fatigue and ultrasonic attenuation", Symposium on nondestructive testing, ASTM STP 213, 1957, pp. 63-69.

73. William,J.H.Jr., and Lampert,N.R., 'Ultrasonic Evaluation of Impact Damaged Graphite Fiber Composite', Materials evaluation, vol.38, no.12, December 1980, p. 68.

74. Chimenti D. E. and Fiedler C. J.,"Leaky plate waves for nde of composites", Ceramic Engineering and Science Proceedings, vol. 8, no. 7-8, Jul-Aug, 1987, pp. 538-546.

75. Liao Peter and Williams James H.," Acousto-ultrasonic input-output characterization of unidirectional fiber composite plate by sv waves", NASA Contractor Reports, no. 4152, June 1988.

76. R.N.Bracewell, The Fourier Transform and its Applications, second rev.ed.(McGraw-Hill, New York, 1986).

77. J.S.Bendat, and A.G.Piersol, Random Data Analysis Measurement Procedures, second rev. ed.(Wiley Interscience, New York, 1986).

78. Talreja R., "On fatigue life under stationary gaussian random loads, Engineering Fracture Mechanics, Vol. 5, pp. 993-1007, 1973.

79. Hemann J.H. and Baaklini G.Y., "The Effect of Stress on Ultrasonic Pulses in Fiber Reinforced Composites," NASA Contractor Report 3724, Aug 1983.

80. Steven S. Lee, Private communications.

81. O'Brien, T. K.,"Characterization of delamination onset and growth in a composite laminate,"Damage in Composite Materials, ASTM STP 775, K.L. Reifsnider, Ed., American Society for Testing of Materials, 1982, pp. 140-167.

82. Aveston J., Cooper G. A. and Kelly A., "The properties of fiber composites," Conference proceedings, National Physical Laboratory, Guildford, IPC Science and Technology Press Ltd., 1971, pp. 15-26.

83. Budiansky B., Hutchinson J. W. and Evans A. G., " Matrix fracture in fiber reinforced composites," J. Mech. Phy. Solids, Vol 34, no 2, 1986, pp. 167-189.

84. Barsoum M., Plotnick B. and Wang A.,"Matrix cracking stresses in uniaxially fiber reinforced ceramic composites," Advanced Structural Inorganic Composites, Editor P. Vincenzini, Elsevier Publishers B.V., 1991, pp. 355-364.

85. Kim R. Y. and Pagano N. J.,"Crack initiation in unidirectional brittle matrix composites," Journal of American Ceramic Society, Vol 74, no 5, 1991, pp. 1082-1090.

86. Kim R. Y.,"Failure of unidirectional and cross-ply Sic/cas ceramic composites," Proceedings of the American Society for Composites, Seventh Technical Conference, Oct. 13-15, 1992, University Park, Pennsylvania, pp. 471-480.

87. Kim R. Y.,"Experimental observations of progressive damage in Sic/Glass ceramic composites," Ceramic Engineering and Science Proceedings, Vol. 13, No. 7/8, 1992, pp. 281-300.

88. Wang S. W. and Parvizi-Majidi A.,"Experimental Characterization of the tensile behaviour of nicalon fiber reinforced calcium aluminosilicate composites," Journal of Material Science, Vol. 27, 1992, pp. 5483-5496.

89. Karandikar P. G. and Chou T. W.,"Microcrack growth and moduli reductions in Nicalon-CAS composites under static fatigue and cyclic fatigue," Proceedings of the American Society for Composites, Seventh Technical Conference, Oct. 13-15, 1992, University Park, Pennsylvania, pp. 695-704.

90. Curtin W. A., Private communications.

91. Kimber A.C. and Keer J.G., " On the theoretical average crack spacing in brittle matrix composites containing aligned fibers," Journal of Material Science Letters, Vol. 1, 1987, pp. 353-354.

92. Curtin W. A., "Theory of mechanical properties of ceramic matrix composites," Journal of the American Ceramic Society, Vol. 74, no. 11, Nov 1991, pp. 2837-2845.

93. Reifsnider Kenneth L.," The critical element model: A modeling philosophy", Engineering Fracture Mechanics, Vol. 25, (5-6), 1986, pp. 739-749.

94. Reifsnider Kenneth L. and Stinchcomb W.W.," A critical element model of the residual strength and life of fatigue loaded composite coupons", Composite Materials: Fatigue and Fracture, ASTM STP 907, H.T. Hahn, Ed., American Society for Testing and Materials, 1986, pp. 298-313.

95. Zhu H. and Weitsman Y., " Failure progression in unidirectionally reinforced ceramic composites", Damage Mechanics in Composites, AMD-vol. 150/AD-vol.32, ASME 1992.

96. Kachanov L. M., "Introduction to continuum damage mechanics", 1986, Martinus Nijhoff Publishers.

97. Reifsnider Kenneth L.," Damage and damage mechanics", Fatigue of Composite Materials, ed. K.L.Reifsnider, Elsevier Science Publishers, 1990, pp. 11-77.

98. Marshall D. B., Cox B. N., and Evans A. G., "The mechanics of matrix cracking in brittle matrix composites," Acta Matallurgica, Vol. 33(11), 1985, pp. 2013-2021.

99. Curtin W. A., "Exact theory of fiber fragmentation in a single filament composite", Journal of Material Science, Vol. 26, 1991, pp. 5239-5253.

100. Sutcu M., " Weibull statistics applied to fiber failure in ceramic composites and work of fracture", Acta Metallurgica, vol. 37, no. 2, Feb 1989, pp. 651-661.

101. Bunsell A. R. and Simon G.," Mechanical and structural characterization of nicalon SiC fibers up to 1300 degree C," Composites Science and Technology, vol. 27, no. 2, 1986, pp. 157-171.

102. Marshall D. B. and Evans A. G., "Failure mechanisms in ceramic fiber/ceramic matrix composites", Journal of the American Ceramic Society, Vol. 68, no. 5, May 1985, pp. 225-231.

103. Thouless, M.D. and Evans A. G., " Effects of pull-out on the mechanical properties of ceramic matrix composites, Acta Metallurgica, vol. 36, no. 3, 1988, pp. 517-522.

104. Prewo K. M.," Tension and flexural strength of silicon carbide fiber reinforced glass ceramics," Journal of Material Science, Vol. 21, 1986, pp. 3590-3600.

105. Brennan J.J., and Prewo K.M.," Silicon carbide fiber reinforced glass-ceramic matrix composites exhibiting high strength and toughness," Journal of Material Science, Vol. 17, 1982, pp. 2371-2383.

106. Prewo K.M. and Brennan J.J.," High strength silicon carbide fiber reinforced glass-ceramic matrix composites," Journal of Material Science, Vol. 15, 1980, pp. 463-468.

107. Reifsnider Kenneth L.," Mechanical characterization of ceramic and glass matrix composites ", Ceramic Engineering and Science Proceedings, vol. 6, no. 7-8, Jul-Aug 1985, pp. 504-506.

108. Rousseau Carl Q., " Monotonic and cyclic behavior of silicon carbide/calcium aluminosilicate ceramic composites", Thermal and mechanical behavior of metal matrix composites, ASTM STP 1080, J.M. Kennedy, H.H. Moeller and W.S. Johnson, Eds., American Ceramic Society for Testing and Materials, 1990, pp. 136-151.

109. Prewo K. M.," Fatigue and stress rupture of silicon carbide fiber reinforced glass ceramics," Journal of Material Science, Vol. 22, 1987, pp. 2695-2701.

110. Minford E., and Prewo K. M.," Fatigue behavior of silicon carbide fiber reinforced Lithium aluminosilicate glass ceramics," Proceedings of 21 University Conference on Ceramic Science, Penn State University, July 1985.

111. Stinchcomb, W.W. and Bakis C.E.," Fatigue behavior of composite laminates", Fatigue of Composite Materials, ed. K.L.Reifsnider, Elsevier Science Publishers, 1990, pp. 105-180.

112. Reifsnider Kenneth L., Henneke E.G. II and Stinchcomb W.W., AFML-TR-76-81, Wright-Patterson AFB, OH, 1979.

REPORT DOCUMENTATION PAGE

Form Approved
OMB No 0704-0188

Public reporting burden for this collection of information is estimated to average 1 hour per response, including the time for reviewing instructions, searching existing data sources, gathering and maintaining the data needed, and completing and reviewing the collection of information Send comments regarding this burden estimate or any other aspect of this collection of information, including suggestions for reducing this burden, to Washington Headquarters Services, Directorate for Information Operations and Reports, 1215 Jefferson Davis Highway, Suite 1204, Arlington, VA 22202-4302, and to the Office of Management and Budget, Paperwork Reduction Project (0704-0188), Washington, DC 20503.

1. AGENCY USE ONLY (*Leave blank*)	2. REPORT DATE	3. REPORT TYPE AND DATES COVERED
	August 1995	Final Contractor Report

4. TITLE AND SUBTITLE
Real Time Acousto-Ultrasonic NDE Technique for Monitoring Damage in Ceramic Composites Under Dynamic Loads

5. FUNDING NUMBERS
WU-505-63-12
C-NAS3-26827

6 AUTHOR(S)
Anil Tiwari

7. PERFORMING ORGANIZATION NAME(S) AND ADDRESS(ES)
Virginia Polytechnic Institute and State University
Blacksburg, Virginia 24061

8. PERFORMING ORGANIZATION REPORT NUMBER
E-9827

9. SPONSORING/MONITORING AGENCY NAME(S) AND ADDRESS(ES)
National Aeronautics and Space Administration
Lewis Research Center
Cleveland, Ohio 44135-3191

10. SPONSORING/MONITORING AGENCY REPORT NUMBER
NASA CR-198374

11. SUPPLEMENTARY NOTES
Project manager, George Y. Baaklini, Structures Division, NASA Lewis Research Center, organization code 5250, (216) 433-6016.

12a. DISTRIBUTION/AVAILABILITY STATEMENT
Unclassified - Unlimited
Subject Categories 24 and 37

This publication is available from the NASA Center for Aerospace Information, (301) 621-0390

12b DISTRIBUTION CODE

13. ABSTRACT ***(Maximum 200 words)***
Research effort was directed towards developing a near real-time, acousto-ultrasonic (AU), nondestructive evaluation (NDE) tool to study the failure mechanisms of ceramic composites Progression of damage is monitored in real-time by observing the changes in the received AU signal during the actual test. During the real-time AU test, the AU signals are generated and received by the AU transducers attached to the specimen while it is being subjected to increasing quasi-static loads or cyclic loads (10 Hz, R = 1 0) The received AU signals for 64 successive pulses were gated in the time domain (T = 40 96 μ sec) and then averaged every second over ten load cycles and stored in a computer file during fatigue tests These averaged gated signals are representative of the damage state of the specimen at that point of its fatigue life This is also the first major attempt in the development and application of real-time AU for continuously monitoring damage accumulation during fatigue without interrupting the test. The present work has verified the capability of the AU technique to assess the damage state in silicon carbide/calcium aluminosilicate (SiC/CAS) and silicon carbide/magnesium aluminosilicate (SiC/MAS) ceramic composites Continuous monitoring of damage initiation and progression under quasi-static ramp loading in tension to failure of unidirectional and cross-ply SiC/CAS and quasi-isotropic SiC/MAS ceramic composite specimens at room temperature was accomplished using near real-time AU parameters The AU technique was shown to be able to detect the stress levels for the onset and saturation of matrix cracks, respectively The critical cracking stress level is used as a design stress for brittle matrix composites operating at elevated temperatures The AU technique has found that the critical cracking stress level is 10-15% below the level presently obtained for design purposes from analytical models An acousto-ultrasonic stress-strain response (AUSSR) model for unidirectional and cross-ply ceramic composites was formulated The AUSSR model predicts the strain response to increasing stress levels using real-time AU data and classical laminated plate theory The Weibull parameters of the AUSSR model are used to calculate the design stress for thermo-structural applications Real-time AU together with the AUSSR model was used to study the failure mechanisms of SiC/CAS ceramic composites under static and fatigue loading An S-N curve was generated for a cross-ply SiC/CAS ceramic composite material. The AU results are corroborated and complemented by other NDE techniques, namely, in-situ optical microscope video recordings and edge replication

14. SUBJECT TERMS
NDE, Acousto-ultrasonic; Ceramic composites; Damage monitoring; SiC/CAS

15. NUMBER OF PAGES
193

16. PRICE CODE
A09

17. SECURITY CLASSIFICATION OF REPORT	18. SECURITY CLASSIFICATION OF THIS PAGE	19 SECURITY CLASSIFICATION OF ABSTRACT	20. LIMITATION OF ABSTRACT
Unclassified	Unclassified	Unclassified	

End of Document